Addis Ababa University
Department of Physics

Assessment of spatial and temporal drought variability and its mechanisms over Ethiopia using observational data analysis and regional climate model experiments

By

Tadesse Terefe Zeleke

Submitted in Partial Fulfillment of the Requirements for the Degree of Doctor of Philosophy in Physics at Addis Ababa University

June 2013

ADDIS ABABA UNIVERSITY

Date: January 2013

Author: Tadesse Terefe

Title: Assessment of spatial and temporal drought variability and its mechanisms over Ethiopia using observational data analysis and regional climate model experiments

Department: Physics

Degree: Ph.D Convocation: June 2013

Permission is herewith granted to Addis Ababa University to circulate and to have copied for non-commercial purposes, at its discretion, the above title upon the request of individuals or institutions.

Signature of Author

ADDIS ABABA UNIVERSITY
DEPARTMENT OF PHYSCS

The undersigned hereby certify that they have read and recommend to the Faculty of Graduate Studies for acceptance a thesis entitled **"Assessment of spatial and temporal drought variability and its mechanisms over Ethiopia using observational data analysis and regional climate model experiments"** by Tadesse Terefe Zeleke in Partial Fulfillment of the Requirements for the Degree of Doctor of Philosophy in Physics.

Date: January 2013

Main-Advisor

Gizaw Mingistu (Dr)
Department of Physics
Addis Ababa University

Examiner (external):

Arona DIEDHIOU (Dr)
IRD/LTHE, BP. 53, 38041,
Grenoble Cedex 9 (France)

Examiner (internal):

Elias Lewi (Dr)
Addis Ababa University

Chairperson:

Belayneh Mesfin (Dr)
Department of Physics
Addis Ababa University

I dedicate this dissertation to

My son Dawit Tadesse

for his unconditional love.

God bless you, David.

Abstract

Drought occurrences in Ethiopia and underlying physical mechanisms are investigated during the 1982 to 2009 period using the Standardized Precipitation Index (SPI) and Palmer Drought Severity Index (PDSI) derived from a station observation datasets and a regional climate model (RegCM4) simulation driven by ERA-Interim reanalysis. The RegCM4 model is evaluated for its performance over Ethiopia. The RegCM4 rainfall captured the observed spatial and temporal variability of rainfall over Ethiopia during the spring (FMA) and summer (JJAS) seasons during this period. The performance of the model is also evaluated against other observational atmospheric variables such as temperature, wind field and surface pressure. The RegCM4 shows a good performance in simulating the spatial and temporal variability of these atmospheric variables over Ethiopia. Trend empirical orthogonal function (TEOF), regression, wavelet and composite analyses based on observation and model simulation are then used to investigate the drought trend, frequency and intra-annual variability along with the associated large-scale circulation patterns. All methods of analysis applied to annual data show that the North and Northwest regions of Ethiopia had experienced frequent and more severe drought conditions during the 1980s that attained peak in 1983/1984 and showed a recovery phase afterwards. Drought becomes more frequent and intense in recent decades over southern and southwestern regions in tandem with apparent shift from northern Ethiopia. Analysis at the seasonal scale shows that drought events are more intense and frequent during the spring season than the summer season over the southern regions. Drought conditions during spring are significantly associated with the negative phase of ENSO, the weakening of the Arabian High and the subtropical westerly jet streams. On the other hand, drought conditions during summer are linked to the positive ENSO phase, a weakening of the upper level jet streams and a lower level moisture influx from the Atlantic and Indian oceans. An uneven heating of equatorial Pacific,

Atlantic and Indian Oceans is the main driver for both phases of ENSO, and corresponding anomalies in the moisture and circulation patterns during the two seasons.

Acknowledgements

I am grateful to many individuals and institutes who have helped me throughout my educational journey and it would not have been possible to do without the support and guidance that I received from them. I express my deepest gratitude and appreciation to my advisor Dr. Gizaw Mengistu for his continuous efforts to provide me feedback and instructions and helping me to increase the depth of my knowledge on climate of Ethiopia. He has constantly forced me to remain focused on achieving my goal. His observations and comments helped me to establish the overall direction of the research and to move forward with investigation in depth. Thank you for your support and kind cooperation in facilitating Sandwich Training Educational Program (STEP) at the International Center for Theoretical Physics (ICTP) in Italy, Trieste. Thank you for your confidence in my abilities to present my papers in international conferences held in USA, Italy and Austria. I extend my appreciation and thank to my co-advisor Prof. Filippo Giorgi for enrolling me in the STEP-PhD program of ICTP in Italy, for his transparent support, for careful corrections and for his warm friendship. I thank you for your great support and help that enables me to participate in EGU annual meeting and ICTP international conferences. I would like to express my sincere thanks to Dr. Gulilat Tefera for generously sharing his time and knowledge in our cooperative work. He has played a major role in making me understand the concept of drought mechanism.

This research financially and technically supported by Addis Ababa University, Debre Markos University and International Center for Theoretical Physics (ICTP) Italy. Specifically, I thank Addis Ababa University Physics Department and IGSSA, STEP-PhD program section and Earth System Physics section at ICTP Italy. I would like to acknowledge the use of Addis Ababa HPC cluster as well as facilities at ICTP, NOAA/OAR/ESRL for the Global Precipitation Climatology Project (GPCP) data via Web site at http://www.esrl.noaa.gov/psd/, ECMWF for the ERA-Interim dataset. I also thank University of East Anglia, Climatic Research Unit (CRU) for gridded rainfall and temperature data and UK Met Office, Hadley Centre Global Sea Ice and Sea Surface Temperature (HadISST) for global SST, ECMWF and NOAA for the various data sets used in this thesis. The SST data also available from the National Ocean and Atmosphere

Administration website at http://www.cdc.noaa.gov. I also express my thanks to the Ethiopian Meteorological Agency (NMA) for providing rainfall and temperature data.

I would like to thank among many individuals who have generally offered suggestions and helped for making this study more usable and fruitful are Dr. Solomon, Samuel, Aleminew, Hayimanot, Ayenew and others due to continuing appreciation and for their kind advice. I would like to thank ICTP, STEP fellow ship, Prof. Nadia, Dory, Pandora and Addis Ababa University Dr. Belayneh who helped me a lot in facilitation of administrative affairs. I also thank ESP group to their help especially to Dr. Laura and other members. Thanks for all Fermi-building officials (ICTP). I would like to mention that I have spent a very fruitful time on my study and with my colleagues.

Last but not the least; I would like to thanks to my parents (Terefe Zeleke and Emamye Abiye) and family members (Kinde, Habitamu, Abebu, Abebaw or Abel, Mulat, Samuel and others) for the personal sacrifices they made to push me forward to allow me to reach new levels of excellence. A sweet word to my wife, Aselefech Sorsa who always shares any difficulties and happiness with me and for her great love to our cute son, Dawit Tadesse, the little guy who most of all gives me emotion and support to overcome difficulties in my work.

Table of Contents

Common abbreviations used in text

Regional Climate Model	RCM
International Center for Theoretical Physics Regional Climate Model version 4	RegCM4
International Center for Theoretical Physics Regional Climate Model other versions	RegCMx
Global Precipitation Climatology Project	GPCP
Climatic Research Unit	CRU
European Center for Medium range Weather Forecasting	ECMWF
European Centre forMedium-RangeWeather Forecasts (ECMWF) older global atmospheric reanalysis product	ERA-40
European Centre forMedium-RangeWeather Forecasts (ECMWF) latest global atmospheric reanalysis product	ERA-Interim or ERIM
National Centers for Environmental Prediction	NCEP
National Center for Atmospheric Research	NCAR
National Oceanic and Atmospheric Administration	NOAA
Hadley Centre Global Sea Ice and Sea Surface Temperature	HadlSST
Hadley Centre Global Sea Ice and Sea Surface Temperature version 2	HadlSST2
United State Geological Survey	USGS
Global Land Cover Characterization	GLCC
Palmer Drought Severity Index	PDSI
Standardized Precipitation Index	SPI
Standardized Precipitation Index computed on 12-month time scale	SPI12
Standardized Precipitation Index computed on 3-month time scale	SPI3
Empirical Orthogonal Function	EOF
Trend Empirical Orthogonal Function	TEOF
Rotated Empirical Orthogonal Function	REOF
Principal Components	PC
Trend Principal Components	TPC
Rotated Principal Components	RPC
Summer season	JJAS
Spring season	FMA
Sea Surface Temperature	SST
Equatorial East Pacific	EEPc
Atlantic	Atl
Indian	Ind
The “Southern Oscillation” is warming (El Niño)/cooling (La Niña) SST of the tropical eastern Pacific Ocean and increasing/decreasing in air surface pressure in the tropical western Pacific	ENSO/SO
North Atlantic Oscillation	NAO
The Intertropical Convergence Zone	ITCZ
Indian Ocean Dipole	IOD

CHAPTER - ONE

Introduction

1.1. Motivation and Objectives of the Thesis

Ethiopia is located between latitudes 3-15^{o}N and Longitudes 33-48^{o}E covering an area of about 1.11 million square kilometers at the Horn of Africa. It is the most populous landlocked country in the world and the second-most populous country in Africa with a population of around 84 million. Agriculture play a dominant role on the economy of the country; which accounts for about 45% of the Gross Domestic Product (GDP), ~85% of exports and more than 84% of the population earning a living directly or indirectly from agricultural activities (RRC 1985; http://en.wikipedia.org/wiki/Ethiopia; CIA 2009). The agriculture sector is very dependent on rainfall, with only 2 percent of the total arable land being irrigated (FAO/WFP 2004).

Drought has affected most parts of Ethiopia with strong impacts on livelihood and economic development of the country for a long period. However, drought is considered as a worldwide phenomenon affecting broad regions and causing significant damages in both human lives and economy (Wilhite and Glantz 1985, 1987). Occurrence frequency of drought in Ethiopia followed by food insecurity has increased during recent decades (Tilahun 1999). List of recorded drought and famine crises that causes food shortage and excess mortality over Ethiopia are found in Pankhurst (1961, 1968) and reference therein. People have been suffering by the consequences of drought events, especially since the 1980s. Partly owing to this, the performance of the national economy fluctuates considerably with changes in weather conditions. For example, in 1984, one extreme drought event is observed in the country; which affected the food intake of about 8 million people and over 1 million died (RRC 1985).

Not only agriculture but also other sectors like health (Malaria) and energy (hydropower) are also sensitive to the intra-annual variability of rainfall in the country (Zhou et al. 2004). Thus, understanding the variability and the physical mechanism of rainfall and drought events is essential in Ethiopia for drought preparedness, mitigation, relief policies and programs and in

general to secure the economy of the country. In the present study, we explore the major patterns of long-term change over the last three decades and inter/intra-annual variability of drought events using observational and RegCM4 simulation datasets. Understanding the physical and dynamical mechanism associated with variability of drought events in Ethiopian regions are other main target of the study. Furthermore, we quantify the severity, duration and spatial extent of drought over the country.

1.2. Thesis Outline

The thesis will begin with the literature review of published work on drought definition, drought forms, drought indices, relevant drought/rainfall variability and mechanism studies in chapter two. The descriptions of the data and methods used in the thesis are then given in chapter three. The validation of Regional Climate Model version 4 (RegCM4) during spring and summer season is given in chapter four.

A detailed study of characteristics of drought (multi-scale temporal and spatial variability and distribution) over different regions of Ethiopia by applying different statistical methods using observational and RegCM4 driven indices is described in chapter five. Furthermore, in this chapter seasonal contribution is assessed for the overall drought severity during specific drought years. Large-scale atmospheric features that affect seasonal drought variability in the regions are described in chapter six. This is based on analysis of composites of atmospheric fields based on wet and dry condition years of drought indicators. Additionally, the correlation patterns of the first two dominant Trend Principal Component (TPC) seasonal drought indices with global Sea Surface Temperature Anomaly (SSTA) and with global circulation are used for the same purpose. Composite of atmospheric fields based on warm and cold SSTA years of selected ocean basins (East Equatorial Pacific, Atlantic and Indian) are discussed to understand the physical linkage. This chapter discusses the wider implications of the thesis including on the issue of causal link versus extreme drought events and on mechanisms of oceanic basins teleconnections with the spring and summer drought events. Finally, the main results of the thesis are

summarized in chapter seven based on the previous chapters and important mathematical expressions and definitions are included in the Appendix section.

CHAPTER -TWO

Background and Literature Review

To provide insight on drought features, first we describe the climate of the study area, then review definitions and forms of drought events as well as drought indicators. Studies of drought/rainfall variability and factors that govern the variability of these variables are described.

2.1. Climate of the study Area

Ethiopia is the country, with its topography varying from about 4,500m above sea level in the north and central regions to about 100 m below sea level over the lowland in the northeastern regions of the country (Fig. 2.1). The main topographic feature of the country consists of a high plateau and mountain chains; which include the great East African Rift Valley that runs northeast to southwest across the country, the highlands to the west and east of the rift valley and the lowlands surrounding the highlands (Chisholm 1911, Paul 2000). The western highlands cover large part of the country and run south to north while the eastern highlands run southwest to east as shown in Fig. 2.1. Because of these complex topographical and geographical features, the climate of Ethiopia exhibits strong spatial variations and different rainfall regimes (National Meteorology Service Agency 1996; Slingo et al. 2005; Mengistu Tsidu 2012). For example, the northwestern regions of Ethiopia are characterized by a single summer (June-September) rainy season (Kassahun 1987; Degefu 1987; Segele et al. 2009a, 2009b; Diro et al. 2011a; Zeleke et al. 2012; Mengistu Tsidu 2012) with characteristics similar to the Sahel and the Indian monsoon (Bhatt 1989; Camberlin 1997). The eastern regions exhibit a bimodal (two wet periods throughout the year) pattern long rainy season summer and a second short rainy season in the spring (February-May); which mainly due to the moist easterly flow from the northwestern Indian Ocean associated with high pressure over the Arabian Sea (Camberlin and Philippon 2002; Diro et al. 2011b). Similarly, the southern regions show a bimodal rainfall pattern with maxima in spring and autumn (October-December), a pattern similar to that found over equatorial eastern Africa caused by the north-south migration of the Intertropical Convergence

Zone (ITCZ). The southwestern regions exhibit a unimodal rainfall peak in summer like the northwest, but they also receive rainfall throughout the year (Kassahun 1987; Degefu 1987; Diro et al. 2011a; Zeleke et al. 2012; Mengistu Tsidu 2012).

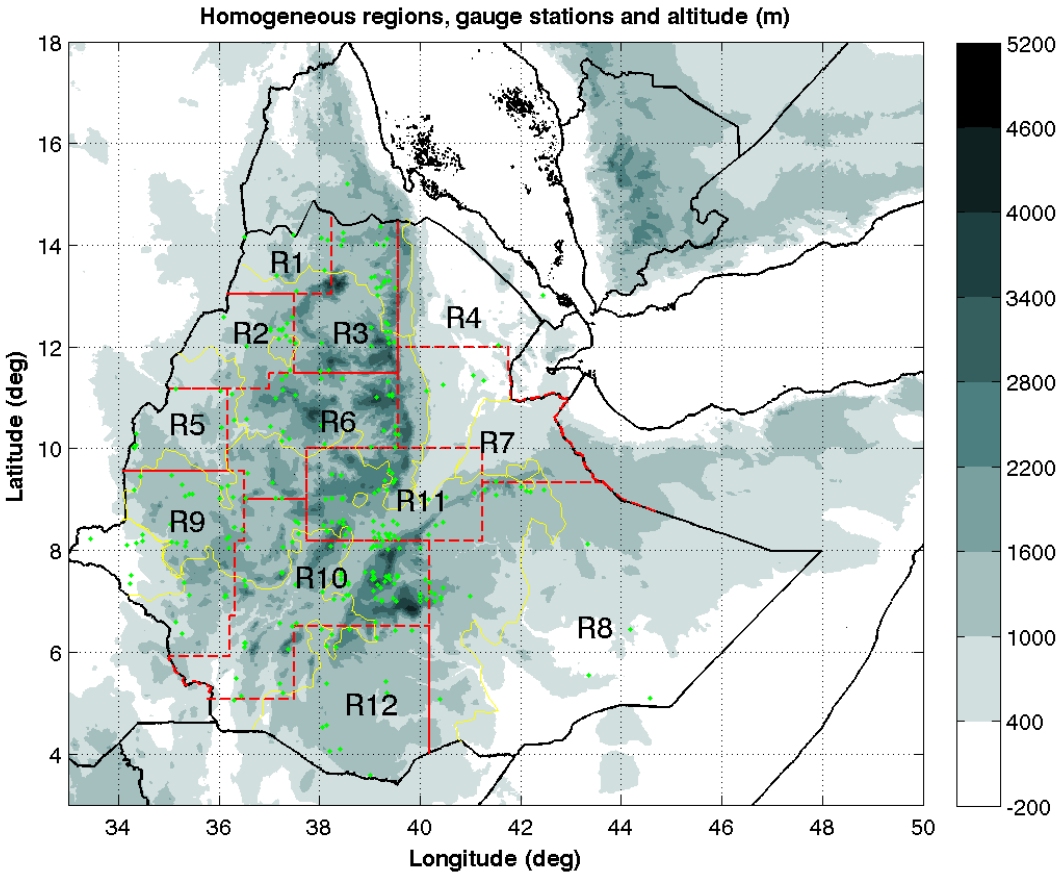

Fig. 2.1) Topography (in meters) of the study area. The broken red lines are the 12 homogeneous rainfall regions. The green dots represent the 290 rainfall stations used in this study.

2.2. Definition and forms of drought

Drought is a recurrent feature of climate. It can occur in virtually all climatic zones, with its characteristics varying significantly from one region to another. The interdependence across climatic, hydrologic, geomorphic, ecological and societal variables makes it very difficult to adopt a definition that fully describes the drought phenomena and associated impacts. The development of drought is given in form of flow chart (Fig. 2.2) and describes the respective impacts. In fact, the impacts of a drought increase slowly, often accumulate over a considerable

period and may linger for years after termination (Palmer 1965; Gibbs and Maher 1967; Mckee et al. 1993, 1995). Because of this, drought has several definitions; the central element is the deficit compared to the normal, or mean, amount of precipitation over an extended period such as a season, a year, or several years. Other climatic factors such as high temperatures, changes in large-scale circulation, low relative humidity, timing and characteristics of rains, distribution of rainy days during crop growing seasons, intensity, duration, onset and termination of rain are often associated with drought in many regions (Palmer 1965; Gibbs and Maher 1967; Mckee et al. 1993, 1995).

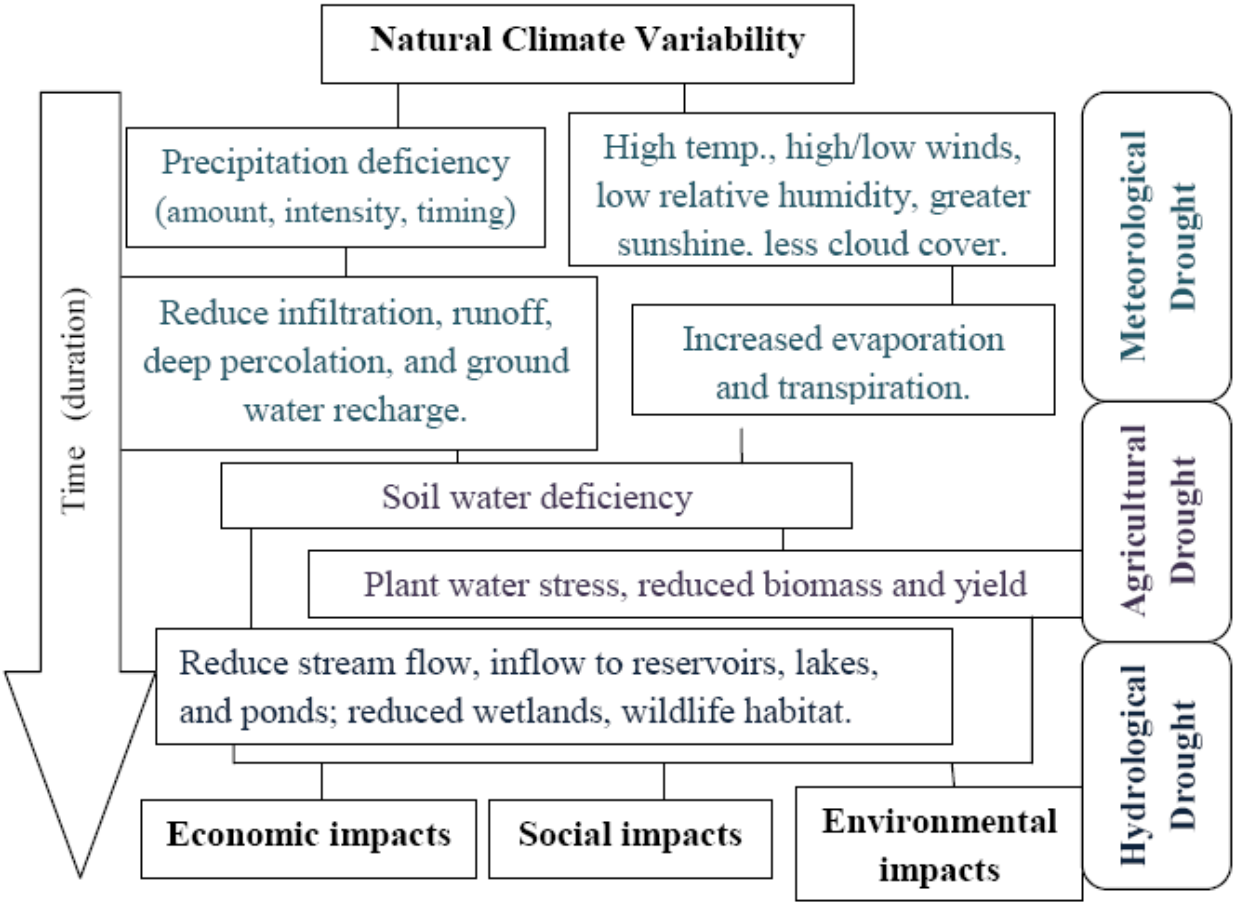

Fig. 2.2 Influence of precipitation deficiency and other factors on drought development (National Drought Mitigation Center)

Drought is classified mainly into meteorological, agricultural, hydrological and socioeconomic drought. Meteorological drought is characterized by a shortage of precipitation and represents a departure of precipitation from its climatological value calculated over a period of time (Bordi and Sutera 2007). Agricultural drought is a shortage of precipitation, soil water and increment of evapotranspiration and it is characterized by a short-term moisture deficiency in the shallow plant root zone (Palmer 1965). Hydrological drought is the result of reduction in surface water and ground water due to amount and/or spatial and temporal distribution of precipitation and it has long-term effects on regional or local surface and subsurface water supplies. Socioeconomic drought is associated with the supply and demand related to meteorological, agricultural and hydrological drought consequences (Palmer 1965; Mckee et al. 1993, 1995).

Drought indices are important elements for drought monitoring and assessment since they simplify complex interrelationships between many climate parameters and are more readily understandable for decision-making. Among many indices suggested so far are - Crop Moisture Index (CMI, Palmer 1968), Deciles (Gibbs and Maher 1967), Palmer Drought Severity Index (PDSI, Palmer 1965), Standardized Precipitation Index (SPI, Mckee et al. 1993, 1995), the Soil Moisture Drought Index (SMDI, Hollinger et al. 1993) and Crop-Specific Drought Index (CSDI, Meyer and Hubbard 1995). Their pros and cons are discussed in corresponding studies and by different authors (e. g. Alley 1984, Karl 1986, Heddinghaus and Sabol 1991; Guttman et al. 1998; Mishara and Singh 2010).

2.3. Rainfall and drought variabilities

Agriculture is the backbone of the Ethiopian economy; which is heavily dependent on natural rainfall variability. Hence, the failure of seasonal rainfall is seriously affects the country's food production and has claimed millions of human and animal lives (RRC 1985; Degefu 1987; Bekele 1997). An example of such an occurrence is the 1984 drought that resulted from the failure of the spring rains and deficiencies in the summer rainfall, aggravated by long dry-spells and their untimely onset. However, the severity and frequency of occurrence of drought vary

over different parts of the country. Rainfall variability and associated droughts have historically been major causes of food shortages and famine in the country (Wood 1977; RRC 1985).

Seleshi and Demaree (1995) identified a declining trend in summer (June-September) rains; which mainly is due to that reduction of July and August rainfall for the period 1965-1984 in the north-central Ethiopian highlands. Osman and Sauerborn (2002) found a downward trend for annual rainfall in the central highlands. Recently, Funk (2003, 2012) and Mengistu Tsidu et. al (2011) reported a significant decreasing trend of the summer rains in the southwestern highlands of the country for the period 1961-1996 and Seleshi and Zanke (2004) found significant decline of rainfall since 1982 in eastern (Jijiga, 137mm/decade), southern (Negele, 119mm/decade) and southwestern (Gore, 257mm/decade) stations. However, Seleshi and Zanke (2004) indicated in the central, northern and northwestern parts of the country for a period 1965-2002 have no significant trend in the annual and seasonal rainfall totals or rainy days. Similarly Conway (2000) reported absence of long-term trend for annual rainfall in the northern and northeastern parts of the country and Seleshi and Camberlin (2006) also supported the absence of significant trends in many indices of extreme rainfall events for the spring and summer rainfall over many regions of Ethiopia. These contrasting results of trend identification in annual rainfall in the central and northern highlands may be because;

- using different periods for the analyses (e.g. Seleshi and Demaree 1995; Conway 2000; Osman and Sauerborn 2002; Funk 2003),
- using area average time series; which may mask spatial variability (e.g. Seleshi and Demaree 1995; Osman and Sauerborn 2002) and
- using too few stations for full representation of the country; which easily miss out localized trends in the Ethiopian because of the diverse topography as discussed in section 2.2 (e.g. Seleshi and Zanke 2004).

In this thesis, we are specifically interested in drought occurrence over Ethiopia, a country particularly vulnerable to drought conditions. There is a general understanding that drought mainly depends on multi-scale temporal and spatial variability of water sources (e.g. precipitation). For instance, the duration and intensity of rainfall in Ethiopia is influenced by fluctuations of the macro-scale pressure systems and large scale atmospheric circulations over

the region (Shanko and Camberlin 1998; Segele and Lamb 2005; Yeshanew and Jury 2007; Segele et al. 2009a, 2009b; Diro et al. 2011a, 2011b; Zeleke et al. 2012). The Tropical Easterly Jet (TEJ), Inter Tropical Convergence Zone (ITCZ), Quasi Biennial Oscillation (QBO), African Easterly Jet (AEJ), winds from the Atlantic and Indian Ocean, the East African Low Level Jet (EALLJ) and the high pressure systems over Mascarene; St Helena and North Atlantic (Azores) are the most likely controls of Ethiopian rainfall during the summer season (Segele and Lamb 2005; Segele et al. 2009a, 2009b; Diro et al. 2011a, 2011b; Zeleke et al. 2012). Conversely, spring rain over southern Ethiopia is affected by the ITCZ, the Subtropical Westerly Jet Streams (SWJS), easterly anomalies and tropical cyclones from the Indian Ocean, the frequency of tropical cyclones over the southwest Indian Ocean (Kassahun 1987; Camberlin and Philippon 2002; Camberlin 1995, 1997; Segele and Lamb 2005; Diro 2008; Segele et al. 2009a, 2009b and Diro et al. 2011a, 2011b).

These atmospheric circulations could be triggered by the SST anomalies over different oceanic basins. For instance, summer rainfall over the Ethiopian highlands is positively correlated with the equatorial East Pacific sea level pressure and the southern oscillation index and negatively correlated with the SST over the tropical eastern Pacific Ocean (Diro et al. 2011a). High positive SST (El Niño) anomalies during the summer are associated with high drought probability over most of agricultural productive land and major water reservoir areas of the country (Degefu 1987; Tadesse 1994; Seleshi and Demaree 1995). This phenomenon (variability of ocean basins) has significant impact on the displacement and weakening of the rain-producing mechanisms in Ethiopia (Korecha and Barnston 2007; Segele et al. 2009a; Diro et al. 2011a). Overall, SST anomalies in the equatorial Pacific Ocean are significantly correlated with East African rainfall variations, but the signs of the correlations and their phase vary from region to region (Camberlin 1995; Nicholson 1996, 1997; Segele and Lamb 2005; Diro 2008 and Diro et al. 2011a, 2011b).

Other studies also emphasized the influence of other oceanic basins on Ethiopian seasonal/annual rainfall. For example, Diro (2008) showed the association of decadal and multi-decadal oscillations of the Atlantic Ocean with Ethiopian climate. Similarly, Jury (2010) highlighted the role of the Atlantic Multi decadal Oscillation for rainfall over northern Ethiopia. The Indian Ocean SST variability has a dominating role in setting up a dipole precipitation (wet

and dry) pattern over eastern and southern Africa and tends to be associated with the inter-annual climate variability of Ethiopian climate (Shanko and Camberlin 1998). Recently, several studies confirmed the impact of the Indian Ocean Dipole (IOD) mode on the East African seasonal variability of rains (Saji et al. 1999; Webster 1999 and Giannini et al. 1995, 2003) found a dominating forcing of Indian Ocean SST variability on precipitation in the Sahel.

While many studies investigated precipitation variability over the broad region of East Africa and the Sahel, the sub-regional variability of drought conditions over Ethiopia has not been explored in detail. Viste et al. (2012) addressed drought conditions in Ethiopia using the SPI index. They compared episodes in different periods (1972-1975, 1984, 1987, 1990-1992, 1999-2000, 2002-2003, and 2008-2011) by counting number of drought conditions for 14 homogeneous regions of Ethiopia, finding an increase in spring drought during the most recent period over the southern region. In this thesis first, we analyze two drought indexes, the SPI, which is only based on precipitation, along with the PDSI, which is based on both precipitation and temperature anomalies. Then, we explore the major patterns of long-term change, inter/intra-annual variability and periodicity of drought events using both, a high-density observational dataset and a regional climate model simulation (using the ICTP RegCM4 model of Giorgi et al. 2012). This allows us to better explore the physical and dynamical mechanisms associated with the variability of drought events over different Ethiopian regions. Furthermore, we quantify the severity, duration and spatial extent of drought over the country. Our study also provides information on the performance of the RegCM4 in reproducing drought statistics, which is important within the perspective of using this model for climate change simulations over the region.

CHAPTER -THREE

Data and Methodology

Now a daytime compared to the previous decades high quality and high-resolution dataset for both atmospheric and oceanic fields are available; including gauge observation, satellite, reanalysis, model simulation and assimilation data that incorporates various kind of available observations. Similarly, different methods are available to assess the characteristics of drought and its physical mechanism. In this chapter, we briefly describe both dataset and methods that we used in this thesis.

3.1. Data

3.1.1. Gauge data

Gauge observations are considered the most reliable estimates of rainfall reaching the ground. Precipitation is discrete and highly variable in both time and space, so spatial density and distribution of gauge population and continuity of gauge network operation are fundamental for gauge precipitation analysis.

The station rainfall dataset used to calculate drought indices is the same as Zeleke et al. (2012); which obtained from the Ethiopian National meteorological Agency (EMA) and it includes 290 stations (Fig. 2.1) unevenly distributed throughout the country for the period 1982-2009 (Zeleke et al. 2012). The quality of the data varies across stations in terms of time span and missing records. The time series homogeneity is checked for any extreme outliers following the method used by Diro et al. (2008) and references therein. If the time series shows an extreme value, then the ten closest neighboring stations are examined to check whether they exhibit a similar behavior. If so, the value is treated as a true extreme otherwise it is replaced by the value 3×IQR+Q3; where IQR is the inter-quartile range defined as the difference between the upper (Q3) and lower (Q1) quartiles.

The fraction of missed data for those early 1990‟s is as large as 40%, which might have been caused by economic and political stability in Ethiopia. However, the correlation between the full 290 stations and 100 stations whose missing data are less than 18% is 0.8. Therefore, the full 290 stations are assessed to be reliable. On the other hand extended precipitation analyses in space based on a limited number of gauge records can sometimes yield highly biased or even completely unrepresentative results if the precipitation has very low spatial homogeneity. Clearly, there is a dependency of the results on how well gauges sample the precipitation (e.g. Dai et al., 2004; Mengistu Tsidu 2012). Hence, the missing data are filled using a kriging procedure (see below), in which a spherical variogram fits the experimental variogram (Sen 2009).

In order to validate the model against 290 gauge stations data, first we cheek the spatial uniformity by computing the distances d_i of all possible pairs of nearest points and by plotting scatter plot as shown in Fig. 2.1. The distribution of the gauge stations is non-uniform; which concentrated mainly over the central highland regions and only a few stations over the lowland areas. For this purpose we applied kriging procedure, which refers to the interpolation of unknown quantities/variables, let $X(s_o)$ at unobserved locations, based on sample data $X(s_i)$ and assumptions regarding the form of global or local trend (drift) of X and its variance and spatial correlation. The shape, the range, and the direction of the spatial autocorrelation are described by the variogram; which is the main tool in kriging method (see details in Sen 2009; Mengistu Tsidu 2012).

In short, the basic assumption in kriging procedure is that a spatiotemporal process is composed of deterministic and stochastic components. The deterministic components can be global and local trends (drifts). The stochastic component is formed by a purely random and an auto-correlated part. An auto-correlated component implies that on average, closer observations are more similar than observations that are more distant. This behavior is described by the variogram where squared differences between observations against their separation distances. Variogram is used for interpolation as means to determine the magnitude of influence of neighboring observations when interpolating values at unobserved locations (Sen 2009). In theory, only Kriging method of grid generation can produce better estimates (in the sense of being unbiased and having minimum error). In practice, the effectiveness of the technique

depends on the correct specification of several parameters that describe the variogram and the model of the drift (Sen 2009; Mengistu Tsidu 2012).

The variogram describes the spatial dependency of referenced observations in a one or multidimensional space. While usually, we do not know the true variogram of the spatial process we have to estimate it from observations. This procedure is called variography. Variography starts with calculating the experimental variogram from the raw data. In the next step, the variogram estimator summarizes the experimental variogram. Variography finishes with fitting a variogram model to the variogram estimator. The experimental variogram is calculated as the difference between pairs of the observed values depending on the separation vector h. The length of the separation vector h is called lag distance or simply lags. The correct term for $\gamma(h)$ is semi-variogram (or semi-variance, or conventionally variogram), where semi refers to the fact that it is half of the variance of the difference between z_x and z_{x+h}. To calculate the experimental variogram we first have to build pairs of observations. Then the matrix of separation distances D between the observation points is,

$$D = \sqrt{((x_1 - x_2)^2 + (y_1 - y_2)^2)}$$

The spatial process is correlated over short distances while there is no spatial dependency over longer distances. Values are low at small separation distances (near the origin), they are increasing with increasing distances, than reaching a plateau (sill) which is close to the population variance. The length of the spatial dependency is called the range and is defined by the separation distance where the variogram reaches the sill. The variogram model is a parametric curve fitted to the variogram estimator, in our case the spherical model,

$$\gamma_{sph}(h) = \begin{cases} c.\left(1.5\frac{h}{a} - 0.5\left(\frac{h}{a}\right)^3\right), & for\ 0 \le h \le a \\ c, & for\ h > a \end{cases}$$

where c is the sill and a is the range. The parameters c and a may change when a variogram model is fitted to the variogram estimator. The so-called nugget effect is a special type of variogram model. In practice, when extrapolating the variogram towards separation distance zero, we often observe a positive intercept on the ordinate. This is called the nugget effect and it is explained by measurement errors and by small-scale fluctuations (nuggets), which are not captured due to too large sampling intervals. Thus, we sometimes have expectations about the

minimum nugget effect from the variance of repeated measurements in the laboratory or other previous knowledge. More details can be found in (Sen 2009; Mengistu Tsidu 2012). Here main procedures of interpolation of the observations on a regular grid by ordinary point kriging; which is the most popular kriging method is described below. Ordinary point kriging uses a weighted average of the neighboring points to estimate the value of an unobserved point:

$$\hat{Z}_{x0} = \sum_{i}^{N} \lambda_i . Z_{xi}$$

where λ_i are the weights which have to be estimated. The sum of the weights should be one to guarantee that the estimates are unbiased:

$$\sum_{i}^{N} \lambda_i = 1$$

The expected (average) error of the estimation has to be zero. That is:

$$E(\hat{Z}_{x0} - Z_{x0}) = 0$$

where Z_{x0} is the true, but unknown value. After some algebra, using the preceding equations, we can compute the mean-squared error in terms of the variogram:

$$E((\hat{Z}_{x0} - Z_{x0})^2) = 2\sum_{i=1}^{N} \lambda_i \, \gamma(X_i, X_0) - \sum_{i=1}^{N} . \sum_{j=1}^{N} \lambda_i \lambda_j \, \gamma(X_i, X_j)$$

where E is the estimation or kriging variance, which has to be minimized, $\gamma(X_i, X_0)$ is the variogram (semi-variance) between the data point and the unobserved, $\gamma(X_i, X_j)$ is the variogram between the data points X_i and X_j and λ_i and λ_j are the weights of the i^{th} and j^{th} data point. For kriging we have to minimize this equation (quadratic objective function) satisfying the condition that the sum of weights should be one (linear constraint). This optimization problem can be solved using a Lagrange multiplier ν resulting in the linear kriging system of *N*+1 equations and *N*+1 unknowns:

$$\sum_{i=1}^{N} \lambda_i \, \gamma(x_i, x_o) + \nu = \gamma(x_i, x_o)$$

After obtaining the weights λ_i , the kriging variance is given by

$$\sigma^2(x_o) = \sum_{i=1}^{N} \lambda_i \, \gamma(x_i, x_o) + \nu(x_o)$$

The kriging system can be presented in a matrix notation:

$$G\_mod.E = G\_R \qquad where,$$

$$G\_mod = \begin{pmatrix} 0 & \gamma(x_1,x_2) & \cdots & \gamma(x_1,x_N) & 1 \\ \gamma(x_2,x_1) & 0 & \cdots & \gamma(x_2,x_N) & 1 \\ \cdot & \cdot & \cdots & \cdot & \cdot \\ \vdots & \vdots & \cdots & \vdots & \cdot \\ \gamma(x_N,x_1) & \gamma(x_N,x_2) & \cdots & 0 & 1 \\ 1 & 1 & \cdots & 1 & 0 \end{pmatrix}$$

is the matrix of the coefficients, these are the modeled variogram values for the pairs of observations. Note that on the diagonal of the matrix, where separation distance is zero, the value of γ vanishes.

$E = \begin{bmatrix} \lambda_1 \\ \lambda_2 \\ \cdot \\ \cdot \\ \cdot \\ \lambda_N \\ \nu \end{bmatrix}$, is the vector of the unknown weights and the Lagrange multiplier

$$G\_R = \begin{bmatrix} \gamma(x_1,x_o) \\ \gamma(x_2,x_o \\ \cdot \\ \cdot \\ \cdot \\ \gamma(x_N,x_o \\ 1 \end{bmatrix},$$

is the right-hand-side vector. To obtain the weights and the Lagrange multiplier the matrix G_mod is inverted:

$$E = G\_mod^{-1}.G\_R, \qquad the\ kriging\ variance\ is\ given\ by \quad \sigma^2 = G\_R^{-1}.E$$

Hence, the data are gridded using a kriging procedure in which a spherical variogram fits the experimental variogram and the gridded result from the kriging procedure close to the boundaries of Ethiopia is essentially an extrapolation. For this reason, the gridded gauge data are

blended with Global Precipitation Climatology Project (GPCP) data. The merging is done in such a way that after both the GPCP and kriged data are interpolated onto a 0.9°×0.9° grid and the gridded gauge data are used only between 34°E-43°E and 4°N-14°N, while the remaining region is filled with the GPCP data. The observed data comparisons are done in the homogeneous regions (see Section 3.4) before merging them. Using similar procedure, we produce gridded temperature (from station over Ethiopia and CRU over other regions of Africa) and availability of water content (from station and model simulation).

3.1.2. Global Precipitation Climatology Project (GPCP)

Global Precipitation Climatology Project (GPCP) combines the precipitation information available from each source (satellite infrared and microwave estimates of rainfall and gauge observations) into a final merged product by taking advantage of the strengths of each data type and removing biases based on hierarchical relations in a stepwise approach (Adler et al., 2003). GPCP is one of the few precipitation products that take advantage of both satellite estimates and gauge analyses to provide global coverage of monthly mean precipitation on $2.5^{o} \times 2.5^{o}$ grids. It has been validated against gridded gauge data over Ethiopia in recent study (Mengistu Tsidu 2012) and robust enough in comparism with other datasets, hence we used GPCP to merge with gauge data as described above.

3.1.3. Climatic Research Unit (CRU)

Climatic Research Unit (CRU) is the University of East Anglia product; with 0.5×0.5 degree resolution (Mitchell et al 2005). Nine gridded climate variables (temperature, diurnal temperature range, daily minimum and maximum temperatures, precipitation, wet-day frequency, frost-day frequency, vapor pressure and cloud cover) are publicly available (http://www.cru.uea.ac.uk/). The station anomalies were interpolated into a regular latitude-longitude grid following New et al. (2000) and adjusted to correspond to the published norms (New et al., 1999). Temperature and precipitation estimates, were made for 80-100% of the land

surface. The database is checked for in-homogeneities in the station records using incomplete and partially overlapping records by detecting in-homogeneities with opposite signs in different seasons and by development reference series using neighboring stations (Mitchell et al 2005). Inter-comparism of observational temperature shows CRU better correlated with station over Ethiopia, hence we used to merge with station as described in Section 3.1.1 procedure.

3.1.4. Sea Surface Temperature (SST)

Sea surface temperature (SSTs) for the same time was obtained from the UK Met Office Hadley Centre Global Sea Ice and Sea Surface Temperature (HadISST2, Rayner et al. 2005). This analysis (the Second Hadley Centre Sea Surface Temperature dataset (HadSST2)) is based on data contained within the recently created International Comprehensive Ocean-Atmosphere Data Set (ICOADS) database and hence it is superior in geographical coverage to previous datasets and has smaller uncertainties and gives monthly mean temperatures with a resolution of $1^{o}\times1^{o}$ (Rayner et al. 2003, 2005) .

3.1.5. Reanalysis Data

ERA-Interim is the third generation European Centre for Medium-RangeWeather Forecasts (ECMWF) gridded reanalysis product (Dee et al. 2011). ERA-Interim improved various difficulties encountered in the production of ERA-40 including improvement of the representation of the hydrological cycle, the quality of the stratospheric circulation, the consistency in time of the reanalyzed fields by using improved representation of moist physical processes. In forecast models, an improved model physics, variational bias correction of satellite radiance data, an improved fast radiative transfer model, better use of satellite observations over land; which leads to more accurate representations of clouds and precipitation. A similar improvement in the exchange of fluxes between atmosphere and ocean is achieved by including the ocean mixed layer in the forecast model. Advances in the treatment of soil hydrology and snow in land-surface models lead to improved fluxes of heat and moisture in the atmospheric boundary layer (Dee et al. 2011). In addition to ERA-Interim, we used data from the National

Centers for Environmental Prediction-National Center for Atmospheric Research (NCEP–NCAR) reanalysis products (Kalnay et al. 1996; Kistler et al. 1999, 2000).

3.2. Data Analysis Method

3.2.1. Empirical Orthogonal Function (EOF)

To capture the patterns of co-variability of rainfall and other atmospheric variables at different stations and in Ethiopia, the Principal Component (PC) analysis (PCA) is applied to the time series. The method consists in computing the covariance matrix of the analyzed atmospheric variable dataset with the corresponding Eigen-values and Eigen-vectors (Navarra and Simoncini 2010). The projection of the analyzed atmospheric fields (e.g. rainfall, temperature, wind, etc) into the orthonormal Eigen-functions provides the principal components (PC) score time series. The spatial patterns (Eigen-vectors), properly normalized (divided by their Euclidean norm and multiplied by the square root of the corresponding Eigen-values), are called Empirical Orthogonal Function (EOF) or simply "loadings". The loadings in this study are the correlation values between the original data time series at each grid point and the corresponding principal component time series.

In order to extract more localized spatial patterns of variability, we apply the Varimax rotation to the loadings (Richman 1986; Jolliffe 1987; Rencher 1998; Von Storch and Zwiers 1999). Rotated Empirical Orthogonal Function (REOF) analysis is applied to atmospheric variables such as rainfall, temperature, low-level wind (averaged between 1,000 and 850 hPa), upper level wind (average of pressure levels between 100 and 300 hPa), vertical wind profile averaged over the longitude band between 35°W and 68°E and for selected oceanic basins. The region that is included in the REOF analysis of rainfall is between 34° and 49°E and 4° and 15°N for consistency with the gauge data.

To remove the influences of location and spread from a set of data, all atmospheric variables time series are standardized by subtracting the mean and dividing by the standard deviation. For each mode, a spatial pattern of loadings describes its area of influence and time scores that reveal the amplitude and wavelength of oscillation. Hence, we used standardized anomalies of time scores (PCs/RPCs) for wavelet and correlation analysis for the dominant modes of atmospheric variables (see Appendix A).

3.2.2. Wavelet

Wavelet analysis is a common tool for analyzing the power of local variation within a time series by decomposing a time series into time versus frequency space and hence it describes the variability of drought in terms of pattern and representing the contribution of each period/scale for the overall variance. We can understand easily the wavelet by comparing with Fourier transform. The Fourier transform breaks up a signal into sine waves and expresses a signal in terms of the frequency (x) and power (y) of its constituent sine waves; without reference to when the frequencies occur. Localization in time can be achieved with the Fourier transform by transforming the data within a specified window of time and shifting this window along the time series (Torrence and Compo 1998). However, the window length has to remain fixed, which is the limitation of the method. The wavelet transform addresses this problem by breaking up a signal into scaled versions of a wavelet function; where the scale of the wavelet (the window) varies with frequency. The process is able to measure both the dominant modes of variability and how those modes vary in time versus frequency. The wavelet transform, therefore, expresses a time series into three-dimensional space: - time (x), scale/frequency (y), and power (z) (Torrence and Compo 1998). Hence, the periodic characteristics of atmospheric variables used in this study are explored using wavelet analysis.

We can characterize a wavelet by how localized it is in time (Δt) and frequency ($\Delta\omega$ or the bandwidth) by compromising Heisenberg uncertainty. An example is the Morlet wavelet, defined as

$$\psi_o(\eta) = \pi^{-1/4} e^{i\omega_o \eta} e^{-\frac{1}{2}\eta^2}$$

Where ω_o is dimensionless frequency and η is dimensionless time. When using wavelets for feature extraction purposes the Morlet wavelet (with ω_o =6) is a good choice, since it provides a good balance between time and frequency localization. Assume that we have a time series, x_n, with equal time spacing δt and $n = 0,\ldots,N-1$. We assume also a wavelet function $\psi_o(\eta)$ that depends on a non-dimensional "time" parameter η. Torrence and Compo (1998) then derive the continuous wavelet transform of the discrete sequence x_n as the convolution of x_n with the scaled and translated version of $\psi_o(\eta)$:

$$W_n(s) = \sum_{n'=0}^{N-1} x_{n'} \psi * \left[\frac{(n' - n)\delta t}{s}\right],$$

where * is the complex conjugate of $\psi_o(\eta)$.

In the Fourier space the above expression becomes:

$$W_n(s) = \sum_{k=0}^{N-1} \hat{x}_k \hat{\psi} * (s\omega_k) e^{i\omega_k n \delta t}$$

where the angular frequency is defined as

$$\omega_k = \begin{cases} \dfrac{2\pi k}{N\delta t}, & k \leq \dfrac{N}{2} \\ \dfrac{-2\pi k}{N\delta t}, & k > \dfrac{N}{2} \end{cases}$$

and the discrete Fourier transform.

$$\hat{x}_k = \frac{1}{N} \sum_{n=0}^{N-1} x_n e^{-\frac{2\pi i k n}{N}}$$

Finally the wavelet power spectra is defined as $[W_n(s)]^2$

3.2.3. Composite Analysis

We applied composite analysis to summarize the large-scale atmospheric features for the two extreme cases (dry and wet event years) and to understand the physical and dynamical mechanisms of drought events by viewing as climatology based on specified conditions. Composite analysis has advantages over individual case studies because composing emphasizes simultaneously occurring features, while smoothing random fluctuations.

Seasonal (spring and summer) composite analysis on the selected variables are carried out from observational, reanalysis and model simulation datasets to understand the mechanism behind drought occurrence and climate variability in Ethiopian region. A set of extreme negative and positive (dry and wet) years are selected from seasonal dominant TPCs of drought indices.

The selection of these extreme dry and wet seasonal years is performed using student‟s t-test given by

$$t = \frac{\bar{x}-\mu}{s/\sqrt{n}}$$

where $\bar{x}$ is the sample mean, $\mu = 0$ is the hypothesized population mean, s is the sample standard deviation and n is the sample size. The confidence limits of the mean are calculated from the published value of t corresponding to n-1 degrees of freedom as,

$$\bar{x} - ts/\sqrt{n} \ , \quad \text{and} \quad \bar{x} + ts/\sqrt{n}$$

Then we select the most four dry/wet years out of confidence zone.

3.2.4. Trend Analysis

We applied parametric and non-parametric methods of trend detection such that, there is a significant change over time. Parametric or non-parametric statistical tests can be used to decide whether there is a statistically significant trend or not (Kundzewicz et al. 2000).

Trend Empirical Orthogonal Function (TEOF) is the new method suggested by Hannachi (2007) for a systematic decomposition of the data into a small number of long terms (trend) patterns and remaining short-term variations. The method is used for the extraction of robust trend patterns from a space-time gridded dataset. The method is based on an Eigen-analysis of the covariance/correlation matrix of time positions from sorted data, i.e. inverse ranks, yielding TEOFs and associated Trend Principal Component (TPCs). By sorting the data and looking for patterns that maximize correlation/covariance between inverse ranks, one is looking for linear combinations maximizing total monotonicity, hence capturing trends with their local slow variation feature. The leading non-degenerate Eigen-values are associated with trends, whereas non-trend components are associated with the remaining modes (Hannachi 2007 and Barbosa and Andersen 2009). With the aim of identifying the long-term component (trend) from the time, series of atmospheric variables including drought indices TEOF and for cross verification linear regression is used.

3.3. Drought Indices

Many quantitative measures of drought have been developed based on the particular application and the degree of understanding of the phenomena. Drought indices can summarize different data of rainfall, temperature, soil moisture, stream flow and others into a comprehensible big picture (Palmer 1965; Mckee et al. 1993). They can be used to identify, characterize and analyze drought events, including intensity, duration, severity and spatial extent. There are several indices which measure how much precipitation and temperature for a given period has deviated from historically established norms (e.g. PDSI and SPI). The various drought indices are usually discipline specific and have their own pros and cons. In this study, we used the PDSI and SPI.

3.3.1. Palmer Drought Severity Index (PDSI)

The Palmer Drought Severity Index (PDSI) was developed by Palmer (1965) based on the supply and demand concept for the water balance equation of a two-layer soil model. It depends on several local coefficients estimated with respect to local hydrological norms related to temperature and precipitation averaged over a calibration period, in our case 28 years. The basis of the index is the difference between the amount of precipitation required to retain a normal water balance level and the actual precipitation.

Many authors have used suitable improved versions of the PDSI (Alley 1984; Karl 1986; Heddinghaus and sahol 1991; Soulé 1993). The mathematical derivations and physical interpretation of the PDSI are found in Palmer (1965), Alley (1984), Karl (1986) and Heddinghaus and Sabol (1991) that reviewed here as follows. For each month of every year, four values related to the soil moisture are computed along with their complementary potential values. These eight values are evapotranspiration (ET), recharge (*R*), runoff (RO), loss (*L*), potential evapotranspiration (PE), potential recharge (PR), potential runoff (PRO), and potential loss (PL). The potential evapotranspiration is estimated using Thornthwaite‟s method (Palmer

1965 and reference there in). The PDSI uses the following equations to compute the moisture transfer between soil layers:

$$L_s = \min\{S_s, (PE - P)\} \qquad P \leq PE$$

$$L_u = \frac{[(PE - P) - L_s]S_u}{AWC} \qquad L_u \leq S_u, P \leq PE$$

where *P* is the precipitation, *L*s and *L*u (*S*s and *S*u) are the moisture loss (available soil moisture stored) in the upper or surface and underlying layer(s) respectively at the start of the month. AWC is the combined available field capacity of all soil layers. Palmer (1965) assumed that no runoff occurs until both layers reach field capacity. Palmer (1965) also computed the potential recharge (PR) that brings the soil to field capacity, the potential loss (PL) of soil moisture to ET during dry periods and the potential runoff (PRO):

$$PR = AWC - (S_s + S_u)$$

$$PL = PL_s + PL_u, where\ PL_s = \min(PE, S_s)\ and\ PL_u = (PE - PL_s)\frac{S_u}{AWC} \qquad PL_u \leq S_u$$

$$PRO = AWC - PR = S_s + S_u$$

From PE, PR, PL and PRO, there are four coefficients related to the climate of the area:

$$\alpha_j = \overline{ET_j} \Big/ \overline{PE_j}\ , \qquad \beta_j = \bar{R}_j \Big/ \overline{PR_j}\ , \qquad \delta_j = \bar{L}_j \Big/ \overline{PL_j}\ , \qquad \gamma_j = \overline{RO_j} \Big/ \overline{PRO_j}$$

where ET_j , L_j , R_j, and RO_j are monthly mean evapotranspiration, moisture loss, water recharge, and runoff respectively and j = 1, 2, . . ., 12. The over bars signify that the variables are average values of month j. From these variables, Palmer (1965) computed the „climatologically appropriate for existing conditions" (CAFEC) from a given year and month precipitation P_j and the departure d_j of the monthly precipitation P_j :

$$d_j = P_j - CAFEC = P_j - (\alpha_j PE + \beta_j PR + \gamma_j PRO - \delta_j PL)$$

To compare d_j among regions, Palmer (1965) introduced a moisture anomaly index Z_j that signifies the departure of the monthly weather from the „climatically normal" conditions for j:

$$Z_j = K_j d_j, \qquad where \quad K_j = {17.67\widehat{K}_j}\Big/{\sum_{i=1}^{12} \overline{D}_i \times \widehat{K}_i}, \qquad j = 1,2,\dots,12$$

$$\widehat{K}_j = 1.5 \log_{10} \frac{T_j + 2.8}{\overline{D}_j} + 0.50, \qquad where\ T_j = {(\overline{PE}_j + \bar{R}_j + \overline{RO}_j)}\Big/{(\bar{P}_j + \bar{L}_j)}$$

$\overline{D}_i$ is the monthly average of d_j and T_j is the ratio of „moisture demand" to „moisture supply": By plotting Z versus duration for the worst drought episodes in his study area, Palmer (1965) obtained a linear relationship from which he derived the drought severity equation:

$$X_j = 0.897X_{j-1} + 0.333Z_j$$

The PDSI is the most widely used drought index in the United States for monitoring droughts. It is used to illustrate the areal extent and severity of various drought episodes (Palmer 1967) and to investigate the spatial and temporal drought characteristics (Soule 1993) as well as to explore the periodic behavior of droughts (Rao and Padmanabhan 1984), monitoring hydrologic trends, forecasting crop yields and assessing potential fire severity (Heddinghaus and Sahol 1991), and forecasting drought patterns (Kim and Valdes 2003). Because of its wide applicability, we used this index for our investigation of multi-scale characteristics of drought in Ethiopia.

3.3.2. Standardized Precipitation Index (SPI)

The Standardized Precipitation Index (SPI) was developed by Mckee et al. (1993) to improve drought detection and monitoring capabilities. The SPI has several characteristics that are an improvement over previous indices, including its simplicity and temporal flexibility that allow its application for water resources on all timescales and quantify precipitation deficit on multiple time scales for any location based on a long-term precipitation record for a desired period. This long-term record is fitted to a probability distribution (normally a Gamma distribution, Guttman 1998), then transformed through an equal-probability transformation into a normal distribution, so that the mean SPI for the location and desired period is zero (McKee et

al. 1993). Positive SPI values represent higher than median precipitation and negative values indicate less than median precipitation (Bordi and Sutera 2001).

The SPI is used to monitor short-term water supplies (e.g. meteorological, soil moisture) and long-term water resources (e.g. groundwater supplies, stream-flow and lake and reservoir levels). The SPI is spatially consistent (invariant) and its probabilistic interpretation makes it useful to be used in risk and decision making analyses. It requires less input data (only precipitation) and calculation effort than other indices (Guttman 1998), which makes it useful to describe drought conditions in meteorological, agricultural and hydrological applications (Hayes et al. 1999). Ntale and Tan (2003) found that the SPI is better suited than other indices for several applications and most appropriate for monitoring East Africa drought. They also showed that the linear correlation between the PDSI and SPI is maximum at the 12-month time scale. Thus, due to its advantages the SPI appears to be the most powerful drought index and chosen for this study. Many authors including (Guttman 1998; Hayes et al. 1999; Bordi and Sutera 2001) used the SPI to monitor drought in many regions. McKee et al., (1993) have given mathematical derivation and physical interpretation of SPI and reviewed here in detail.

First a monthly precipitation time series is smoothed with a moving window of width equal to the number of month"s desired (scale needed), let β is scale,

$$p_t' = \frac{1}{\beta} \sum_{i=0}^{i=\beta-1} p_{t-i} \quad \text{where } p = \text{precipitation}, \beta = \text{scale(months)}$$

The filtered data are broken into β monthly time series, which McKee et al. (1993) individually fitted with a gamma distribution g(x),

$$g(p) = \frac{1}{\beta^{\alpha}\Gamma(\alpha)} p^{\alpha-1} e^{-p/\beta} \quad \text{for } p > 0$$

α>0, α is a shape parameter, β>0, and $\Gamma(\alpha) = \int_0^{\infty} y^{\alpha-1} e^{-y} dy, \Gamma(\alpha)$ is the gamma function. Computation of the SPI involves fitting a gamma probability density function to a given frequency distribution of precipitation totals for a station. The alpha and beta parameters of the gamma probability density function are estimated for each station, for each time scale of interest

(β = 3, 6, 9, 12, 48 months) and for each month of the year. From Thom (1966); the maximum likelihood solutions are used to optimally estimate α and β:

$\hat{\alpha} = \frac{1}{4A}(1 + \sqrt{1 + \frac{4A}{3}})$ $\hat{\beta} = \frac{\bar{p}}{\hat{\alpha}}$ $A = \ln(\bar{p}) - \frac{\sum \ln(p)}{n}$, where n=number of precipitation observations.

The resulting parameters are then used to find the cumulative probability of an observed precipitation event for the given month and time scale for the station in question. The cumulative probability is given by:

$G(p) = \int_0^x g(p)dp = \frac{1}{\hat{\beta}^{\hat{\alpha}}\Gamma(\hat{\alpha})}\int_0^p p^{\hat{\alpha}-1}e^{-p/\hat{\beta}}dp$, let $t = \frac{p}{\hat{\beta}}$, this equation becomes the incomplete gamma function: $G(p) = \frac{1}{\Gamma(\hat{\alpha})}\int_0^t t^{\hat{\alpha}-1}e^{-t}dt$. Since the gamma function is undefined for x=0 and a precipitation distribution may contain zeros, the cumulative probability becomes: $H(p) = q + (1-q)G(p)$ where q is the probability of a zero. If m is the number of zeros in a precipitation time series, Thom (1966) states that q can be estimated by m/n. Then the cumulative probability (H(x)) is transformed to the standard normal random variable Z with mean zero and variance of one, which is the value of the SPI.

$$Z = SPI = -\left(t - \frac{c_0 + c_1 t + c_2 t^2}{1 + d_1 t + d_2 t^2 + d_3 t^3}\right) \quad \text{for } 0 < H(p) \leq 0.5$$

$$Z = SPI = +\left(t - \frac{c_0 + c_1 t + c_2 t^2}{1 + d_1 t + d_2 t^2 + d_3 t^3}\right) \quad \text{for } 0.5 < H(p) \leq 1.0$$

where:

$t = \sqrt{\ln(\frac{1}{(H(x))^2})}$ for $0 < H(p) \leq 0.5$ and $t = \sqrt{\ln(\frac{1}{(1.0-H(x))^2})}$ for $0.5 < H(p) \leq 1.0$,

$c_0 = 2.515517,$ $c_1 = 0.802853,$ $c_2 = 0.010328,$

$d_1 = 1.432788,$ $d_2 = 0.189269,$ $d_3 = 0.001308$

Here, we employed both the SPI and PDSI indices because of their advantages described above and in order to check the consistence of the results between the two indices. Both indices use a classification of drought into seven categories ranging from an extremely dry to an extremely wet category (see Table 2.1). .

Table 2.1) Classifications of the dryness/wetness degree in accordance with the PDSI and SPI definitions.

Category	PDSI	SPI
Extremely dry	≤-4.00	≤ -2.00
Severely dry	-3.99 ~ -3.00	-1.99 ~ -1.50
Moderately dry	-2.99 ~ -2.00	-1.49 ~ -1.00
Near normal	-1.99 ~ 1.99	-0.99 ~ 0.99
Moderately wet	2.00 ~ 2.99	1.00 ~ 1.49
Severely wet	3.00 ~ 3.99	1.50 ~ 1.99
Extremely wet	≥4.00	≥ 2.00

3.4. Identification of homogeneous rainfall climate zones

The new merged gridded station dataset is used to identify homogeneous rainfall climate zones. Averaging gauges over large areas is important for increasing the signal to noise ratio, however care must be taken in places where, there is high spatial variation. Rainfall over East Africa in general and Ethiopia in particular exhibits high spatial variation as discussed in the previous chapter. Therefore, it is necessary to divide the country into homogeneous rainfall zones (Diro 2008; Mengistu Tsidu 2012).

We used rotated principal component analysis for grouping of station into homogeneous zones (see section 3.2). This method allows us to find areas within the region that have rather independent climatic variability, i.e. in which the rotated principal components are temporally orthogonal (Rencher 1998). Following the rule by North et al. (1982), 16 significant loading patterns were selected for the rotation to represent the zones. Further examination in to the mean correlation of time series among grid points within a zone and grid points across neighboring

zones was performed to merge two neighboring zones to form a larger zone whenever there is a strong correlation between grid points across the neighboring zones. Additional information like topography, seasonal cycle and spatial proximity to the neighboring zone is also considered when correlation is not a decisive factor. Subsequently the final homogenous rainfall regions are reduced to 12 zones as shown in Fig. 2.1.

Area-averaged standardized seasonal rainfall time series are generated from the identified regions by subtracting the corresponding climatological averages and then dividing by the corresponding standard deviation. The atmospheric variables including rainfall and temperature anomalies of different observational datasets and model simulations are correlated with each other for the evaluation of the performance of RegCM4. Both observational dataset and model simulation monthly mean rainfall and temperature of each homogenous region during the 1982–2009 periods are used for analysis of seasonal cycles. Moreover, the observed and simulated rainfall and temperature anomalies of each homogenous regions are correlated with the large scale features including wind fields generated in the same manner to understand the association of the variables.

3.5. Identification of seasons based on large scale circulation patterns

The monthly mean and inter-seasonal variability of climatological patterns of lower and upper level ERIM and model horizontal wind (Fig. 3.1 and Fig. 3.2); during February-May exhibit marked dissimilarities between February-April and May (correlation between February/March/April and May < 0.52 and correlation between February, March and April > 0.75). This inter-monthly variability shows that more or less different mechanism of drought variability operates on these periods (similar results are reported by Camberlin and Philippon, 2002). In contrary, the variability of large scales circulation climatology during June-September is less; which has significant month-to-month correlations (correlation between June/July/August/ and September is > 0.76). Hence, we consider from February-April as spring season and May as a transition season and from June-September as summer season in the whole document to evaluate the model, to understand seasonal contribution of drought and to explore seasonal mechanisms of drought occurrence and variability.

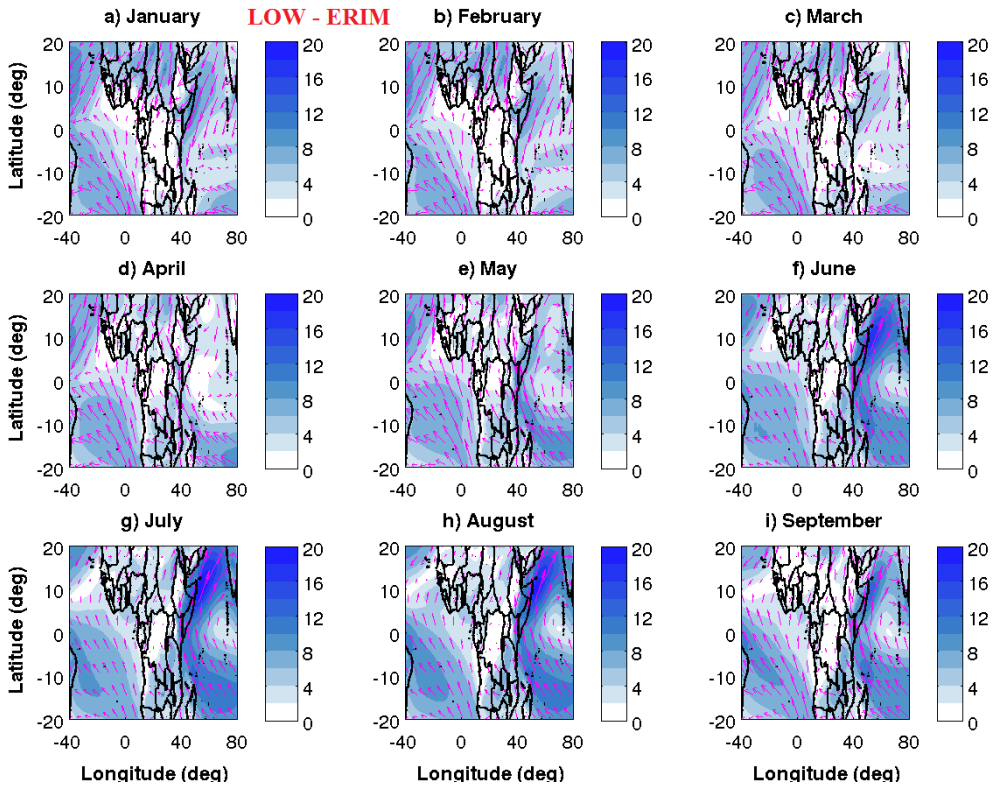

Fig. 3.1) Seasonal (monthly) climatology low-level horizontal wind (averaged between 850-1000hPa).

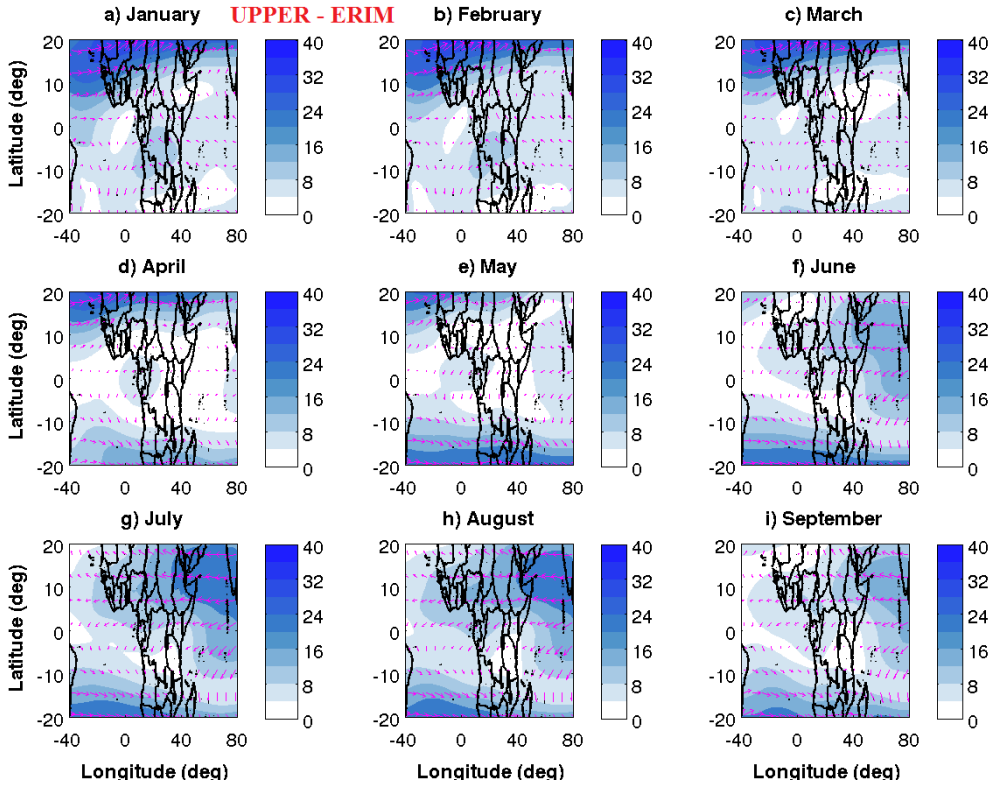

Fig. 3.2) Seasonal (monthly) climatology upper-level horizontal wind (averaged between 100-300hPa).

CHAPTER - FOUR

Evaluation of a Regional Climate Model for the Study Area

Regional climate models (RCMs) have become increasingly important tools used to downscale global (large-scale) climate information for regional applications. Number of studies have demonstrated the capability of regional climate model (RegCMx) in downscaling global climate information for regional applications and representing details of regional climate variability (e.g. Giorgi and Mearns 1999; Giorgi and Shields 1999; Small et al. 1999; Sun et al. 1999a, b; Wang et al. 2003; Pal et al. 2007; Anyah and Semazzi 2007). Such models are driven by initial and lateral boundary conditions taken from reanalysis, observations and from Global Circulation Model (GCM) output (e.g. Dickinson et al. 1989; Giorgi and Bates 1989; Giorgi et al. 1993a, b; Sun et al. 1999a, b; Small et al. 1999; Denis et al. 2002). RCMs become suitable tools for regional process studies; which increase our understanding about influence of local climatic forcing superimposed on large-scale climate variability. By coupling appropriate land surface, hydrologic or lake models with RCMs enable accurate simulations of detailed precipitation, temperature, surface hydrological features and other meteorological variables (Leung and Ghan 1999).

The sensitivity of RegCMx to dynamical configuration such as domain size, resolution and to the physical parameterizations have been demonstrated in a number of studies (e.g. Giorgi et al. 1993a, b; Sun et al. 1999a; Denis et al. 2002; Giorgi and Mearns 1999). Hence before applying a regional climate model for regional climate variability studies, the accuracy of the model in reproducing the observed regional climate, should be assessed to establish its strengths and weaknesses for the specific region (Small et al. 1999).

Regional climate models (RCMs) has been utilized extensively for mid-latitude regions in wide-ranging surface climate and hydrologic process investigations. Sensitivity studies and simulations of present, past and future climates on the mesoscale and regional scale have been done (e.g. Giorgi 1990; Giorgi et al. 1993a, b; Giorgi and Shields 1999; Small et al. 1999; Giorgi and Bi 2000; Pal et al. 2007). Relatively few studies exist for eastern Africa climate (e.g.Sun et al. 1999a, b; Anyah and Semazzi 2007; Davis et al. 2009; Segele et al. 2008; Zeleke et al. 2012;

Gebremariam 2012). Most of the above studies of eastern Africa (except Segele et al. 2008 and Zeleke et al. 2012) focused on the spring and autumn seasons, as these are the main and short rainy seasons for the equatorial Africa. Segele et al. (2008) evaluated the performance of the RegCM3 in reproducing the Ethiopian summer rainfall variability. They found that RegCM3 not only reproduced the spatial variability of dry and wet years but also correlated well with gauge data.

Based on these considerations, in this chapter the performance of a regional climate model (an updated version of the RegCM4, Giorgi et al. (2012) is presented. Here, we briefly discuss/compare the essential atmospheric variables of observational and/with model simulation; that will be necessary in the rest of the thesis to understand the various characteristics of drought events in Ethiopia. Such as in representing the climatology, inter/intra annual variability of atmospheric variables including rainfall, temperature, wind field and surface pressure with respect to relatively large set of rain gauge and satellite based observations and reanalysis datasets.

4.1. Model description

The regional climate model used in this study is the ICTP RegCM4 described by Giorgi et al. (2012). It is a hydrostatic model based on the dynamical core of the Penn State/NCAR Mesoscale Model version 4 (Grell et al. 1994) with the developments described by Giorgi et al. (1993a, b). RegCM4 includes a range of physics options and for the present work, it uses the radiation scheme of Kiehl et al. (1996), the nonlocal planetary boundary layer scheme originally developed by Holtslag et al. (1990) and later modified as described by Giorgi et al. (1993a, 2012). The Biosphere-Atmosphere Transfer Scheme (Dickinson et al. 1993) is used for land surface process calculations. Precipitation is represented by two different terms: resolvable (large-scale nonconvective) and convective (subgrid cumulus). The resolvable scale precipitation is represented by the SUB-grid EXplicit moisture scheme of Pal et al. (2000). For convective precipitation, three options are available: (1) the modified Anthes–Kuo scheme (Anthes 1977; Giorgi et al. 1993b); (2) the Grell scheme (Grell et al. 1994); and (3) the Emanuel scheme (Emanuel and Rothman 1999). In addition, different schemes can be chosen for land and ocean regions (Giorgi et al. 2012). After a number of preliminary tests, we selected the Grell scheme

with the Fritsch-Chappel closure (Fritsch and Chappell 1980; Giorgi et al. 1993b) over land and the Emanuel scheme over the ocean grid points. More information on the different physics schemes and applications of the RegCM model system can be found in Giorgi et al. (2012).

4.2. Experimental Setup

The simulation/analysis period is 1982-2009 and we applied similar experimental setup with previous study; which its initial and lateral boundary conditions are obtained from the new ERA-Interim (ERIM) 1.5° X 1.5° third generation ECMWF gridded reanalysis product (Dee et al. 2011). The Sea Surface Temperature (SST) used to force RegCM4 is obtained from the National Oceanic and Atmospheric Administration (NOAA) weekly Optimum Interpolation (wk-OI, Reynolds et al. 2002) on a one-degree grid. The 10-minute resolution Global Land Cover Characterization (GLCC) data set for vegetation cover, land use and elevation is used as obtained from the United States Geological Survey (USGS). The model domain covers most of the African continent and adjacent ocean waters at a grid point spacing of 50km (Zeleke et al. 2013). This study showed that this domain size is sufficient to obtain a realistic simulation of the climate of Ethiopia.

4.3. Evaluation of RegCM4 during Spring Season

4.3.1. Characteristics of large scale circulation

Spring season climatological patterns of both ERIM and model simulation upper-level horizontal wind (Fig. 4.1a, b; which are averaged between 100 and 300hPa) shows strong spatial consistency. The pattern corresponds to an anomalous southerly extension of subtropical westerly jet streams (STWJ) over northern Africa is reproduced very well by RegCM4.

This pattern in both ERIM and model shows relatively narrow and shallow streams with maximum wind speed. Camberlin and Philippon (2002) and Diro (2008) have shown the down ward bent of subtropical westerly jet stream is related to a large scale convection in the lower troposphere; which is conducive condition for spring rain getting regions of Ethiopia.

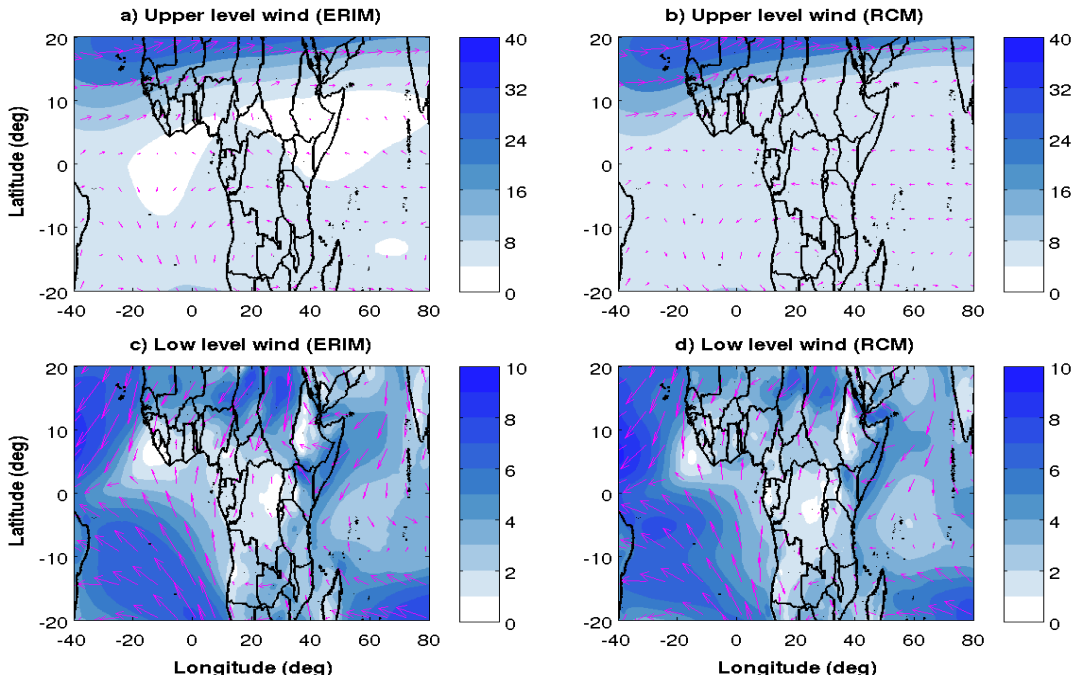

Fig. 4.1) Spring (FMA) season mean horizontal wind: a) upper-level (averaged between 100-300hPa) wind (ERIM), b) upper-level (averaged between 100-300hPa) wind (RCM), c) low-level (averaged between 850-1000hPa) wind (ERIM), d) low-level (averaged between 850-1000hPa) wind (RCM).

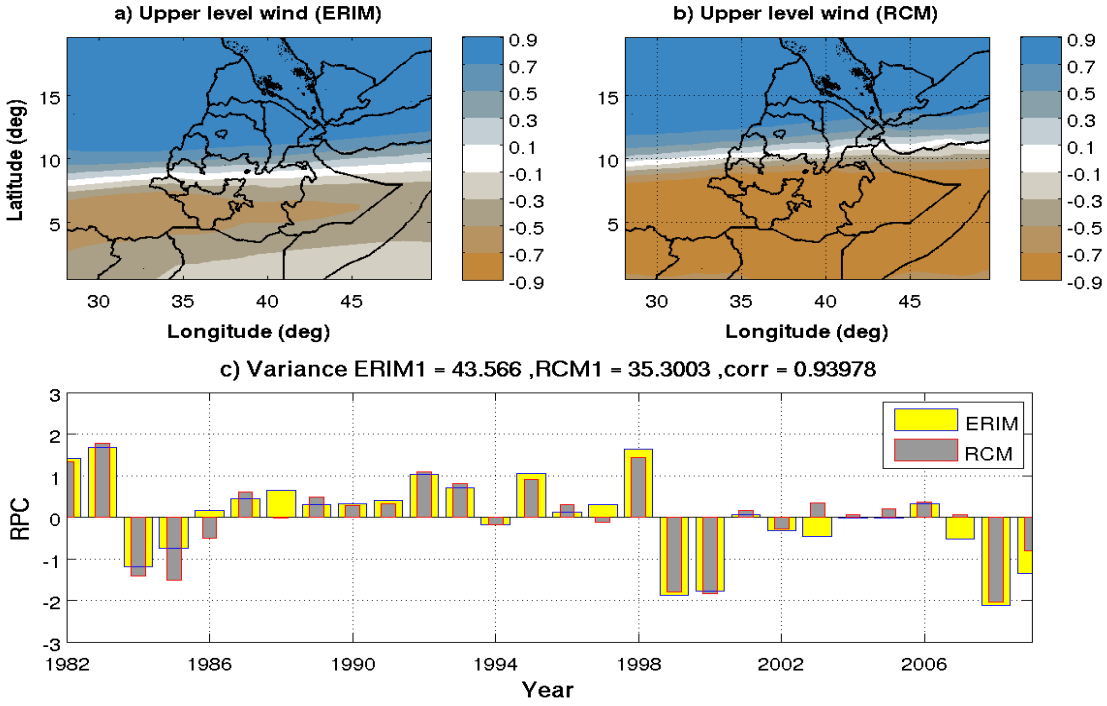

Fig. 4.2) Spring (FMA) season; correlation patterns of upper-level (averaged between 100-300hPa) horizontal wind dominant RPC1 with raw upper-level horizontal wind a) ERIM b) RCM c) Dominant time scores.

The Sub-Tropical Westerly Jet (STWJ) is formed as a result of conservation of angular momentum as the air moves from the lower latitudes to the higher latitudes (Diro 2008 and reference there in). Detail description related to the link between Ethiopian climate and STWJ is given in Section 6.1. The correlation between the time series of the wind field and the first rotated principal component (RPC-1) of the upper level wind (Fig. 4.2a, b) reveals that the spatial pattern of the dominant mode of variability at upper levels is a dipole structure; which shows positive above ~10^{o}N and negative below ~10^{o}N in both model and ERIM. The boundary of the dipole pattern in the model is shifted slightly northward and has stronger magnitude over southern regions. The fraction of variance explained by the first RPC of the model (~35 %) and ERIM (~44 %) are more than 1/3 of total variance. The intra-annual variability of RPC-1 in ERIM and RegCM4 (Fig. 4.2c) shows a good agreement (correlation value of ~0.94) and the extreme years (1982/83, 1984/85, 1992, 1995, 1998, 1999/2000, 2008/09) are well captured. Fig. 4.3a, b shows strongly similar patterns of dominant variability for the latitudinal cross section of horizontal wind in ERIM and RegCM4 and explains ~39% and ~40% of the total variance respectively. The time series of the leading RPCs of the reanalysis and the model simulation are correlated significantly (with value of ~0.97) suggesting a good agreement between ERIM and RegCM4 simulation (Fig. 4.3c).

The low-level horizontal wind climatology for the spring season in ERIM and RegCM4 simulation (Fig. 4.1c, d) shows a good agreement in both the magnitude and direction. The similarity of variability of low-level horizontal wind patterns in Fig. 4.4a, b describes the performance of the model in representing the region of dominant variability in the wind field; which explains ~30% and ~32% of total variance respectively, although small difference are observed over south west regions of Ethiopia. Significant and high correlation (correlation of ~0.86) of the dominant time components (RPC-1s, Fig. 4.4c) confirms the ability of the model to simulate the large-scale circulation.. The importance/link of variability of this wind in its magnitude and direction to the Ethiopian climate is discussed in detail in Section 6.1.

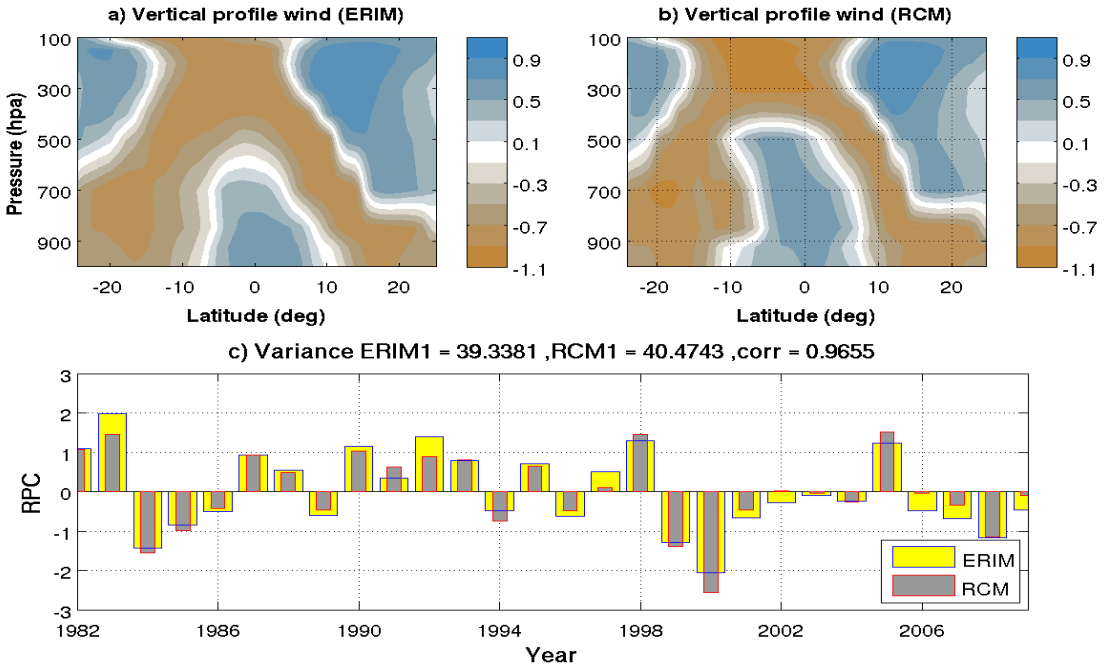

Fig. 4.3) Spring (FMA) season; correlation patterns of mean (averaged in longitude wise from ~ 45W-85E) vertical profile horizontal wind dominant RPC1 with its raw dataset a) ERIM b) RCM c) Dominant time scores of both data sets.

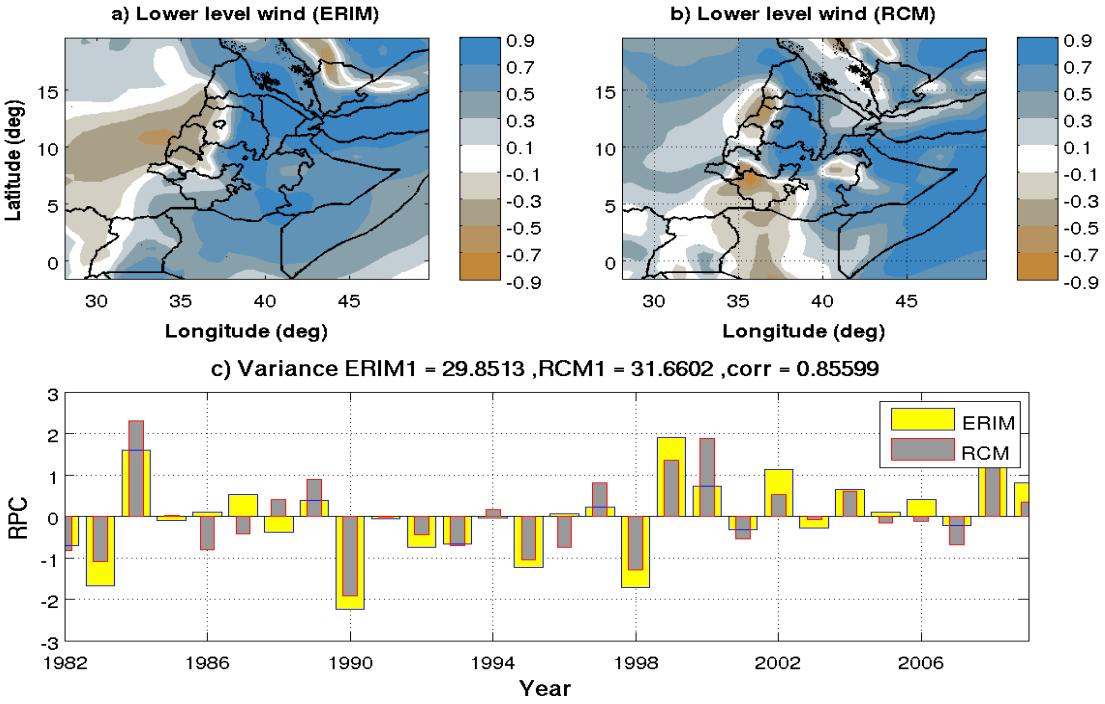

Fig. 4.4) Spring (FMA) season; correlation patterns of low-level (averaged between 850-1000hPa) horizontal wind dominant RPC1 with raw low-level horizontal wind a) ERIM b) RCM c) Dominant time scores.

4.3.2. Rainfall climatology and intra-annual variability

In this section, we examine the spatial patterns of spring mean precipitation and its intra-annual variability. The observed precipitation (Gauge station) (Fig. 4.5a) over the country during this season is mostly confined to Southwest regions of Ethiopia, while regions north and northwest tip regions are predominantly dry. The pattern is reasonable because of the movement of ITCZ towards equator during this season. The southwestern regions receive on average 5 mm/day of rainfall; however, small precipitation rates (1-2 mm/day) are located in northern and northwestern regions (see Fig. 4.5). It exhibits also a southwest-southeast gradient where rainfall decreases from ~5 to less than ~1 mm/day. RegCM4 forced by ERIM reanalysis (Fig. 4.5d) capture the location of higher precipitation rates in the southwest regions but it does not capture the small precipitation rates along the north and northeast regions.

As one moves from southwestern towards northern and northwestern the climatological pattern of spring rainfall decreases and become dry over north and extreme northwest regions. The model reasonably reproduces this climatological pattern of rainfall; however, the model is drier than observed in the northeastern and wetter over the southwestern regions (Fig. 4.5e, f). CRU and RegCM4 locate precipitation in a zonal band around southwest regions, in which rainfall decreases north and northeastwards. Due to lack of gauge stations over north and northeast border regions, CRU does not show any rainfall over these regions. Whereas GPCP represent the patterns of rainfall in similar way of merged gauge dataset. We also note that the CRU datasets show relatively low precipitation amounts over the eastern and along great east African refit valley regions (Fig. 4.5e, f).

Most previous studies of RegCM3 using a smaller domain centered over eastern Africa found difficulties to correctly reproduce the precipitation patterns. For example, Segele et al. (2008) performed 18 years of simulation with RegCM3 over eastern Africa and overestimated by greater than 26% precipitation over Ethiopia, by using the Grell (Emanuel) convective scheme. Anyah and Semazzi (2007) indicated some deficiencies in capturing short east Africa rainy season of the observed rainfall over the Kenya Highlands and Lake Victoria Basin using RegCM3. Sun et al. (1999a) showed some deficiencies over the Congo-Angola Basin and Kenya Highlands and the monsoon flow during the same period was stronger than observed.

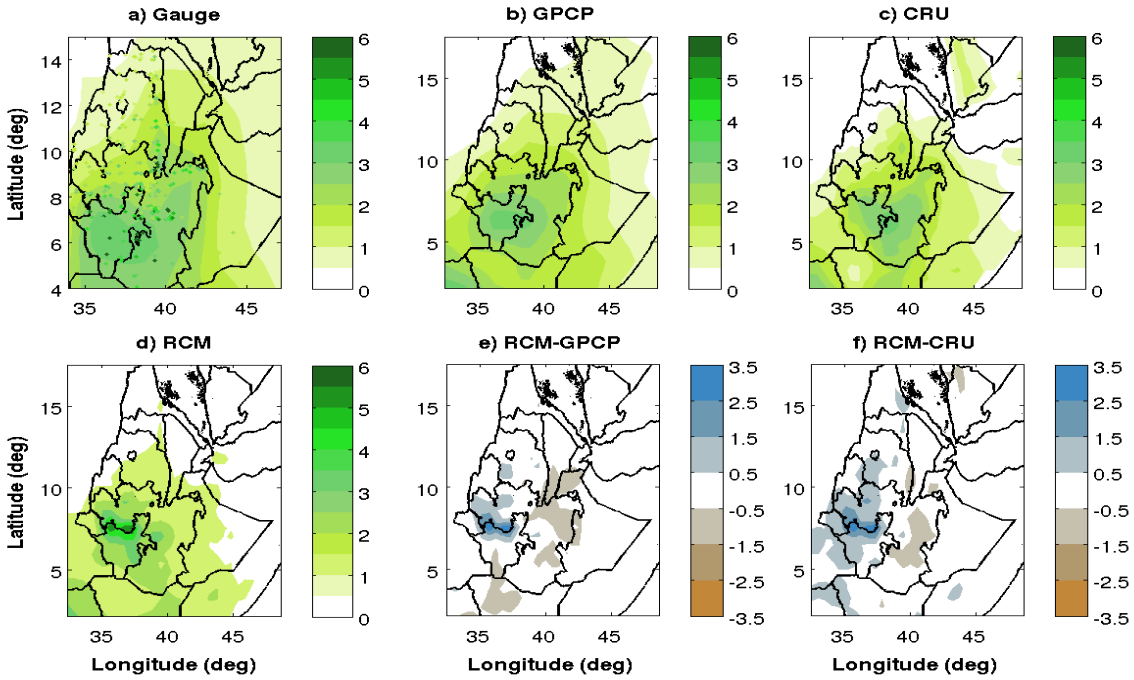

Fig. 4.5) Spring (FMA) mean rainfall: a) Gridded and station rain (gauge), B) GPCP rain c) CRU rain d) RCM rain, e) bias of RCM minus GPCP b) bias of RCM minus CRU.

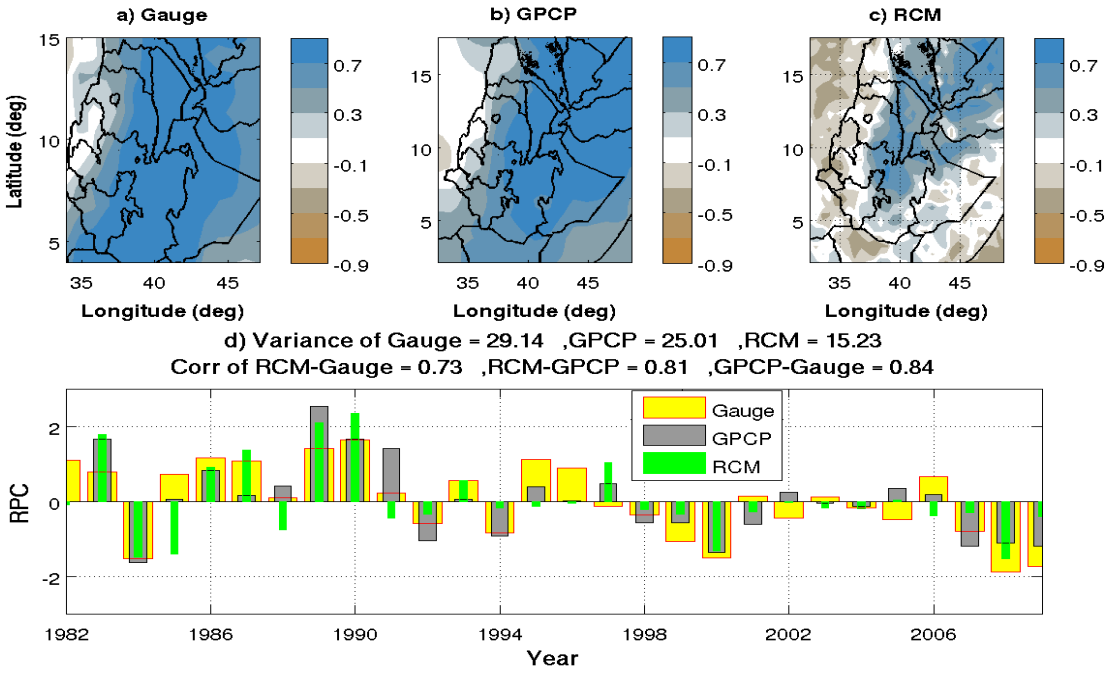

Fig. 4.6) Spring (FMA) season, correlation patterns of rainfall first dominant RPC1 with raw rainfall, a) Gauge b) GPCP c) RCM. (d) is the time series of the RPC1 for the observations and the RCM.

Our simulation showed relatively good performance when we apply dry Grell over land and Emanuel over Ocean and we used ERIM at the lateral boundaries of the simulation.

Fig. 4.6a, b, c shows the spring season intra-annual dominant variability patterns; which explain ~ 29%, ~ 25%, ~ 15% of the total variance of gauge, GPCP and RegCM4 respectively. The patterns are confined over the eastern regions. The pattern shown by the model is a little narrower and smaller percent of the variance that explained by the corresponding PC. The corresponding rotated principal component of RegCM4 (Fig. 4.6d) is correlated significantly with merged-gauge and GPCP dataset (i.e. correlation RCM-RPC and gauge-RPC ~ 0.73, RCM-RPC and GPCP-RPC ~ 0.81, GPCP-RPC and gauge-RPC ~ 0.78). Observed extreme events of spring season for example 1983, 1989 and 1990 which are positive extreme anomaly years and 1984, 2000, 2008/09 negative extreme years from first dominant RPCs are captured correctly.

The second dominant variability patterns are similar in gauge, GPCP and RegCM4 datasets (Fig. 4.7a, b, c) which shows the western regions of the country and explained ~22%, ~24% and ~14% of the variances respectively. This consolidates the performance of the model to reproduce variability of spring rainfall across the regions. The simulated RPC-2 (intra-annual variability) of spring rainfall is significantly correlated (Fig. 4.6d, correlation of RegCM4 and gauge ~ 0.65, RCM and GPCP ~ 0.84) and coincides with extreme years of RPC-2 of observation.

Observed areal averaged standardized anomalies of each homogeneous spring mean rainfall time series are significantly (a significance level of 95%) correlated with the corresponding simulation dataset and summarized in Table 4.1. The result indicates the model standardized precipitation anomaly is highly correlated with the corresponding gauge and GPCP dataset. On contrary weak correlation over most of homogeneous regions with CRU dataset, which may be because of high spatial difference over Ethiopia, using small number of stations may bring such result between simulation and CRU dataset unlike GPCP and gauge. Mengistu Tsidu (2012) reported similar results.

Overall the RegCM4 simulate fairly the observed multi-scale spatial and inter/intra annual temporal variability in Ethiopia (correlation with gauge > 0.7) during spring season. We also noticed GPCP represent the observed multi-scale variability better (correlation with gauge > 0.83) than CRU for both homogeneous areal mean standardized time series and dominant RPCs.

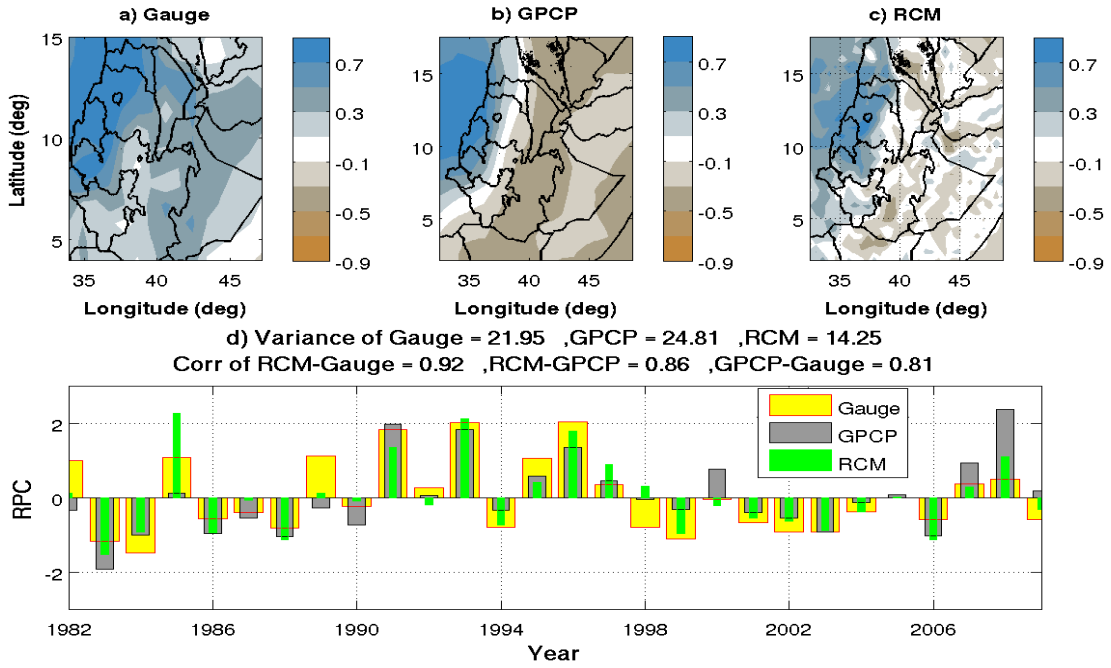

Fig. 4.7) Spring (FMA) season, correlation patterns of rainfall second dominant RPC2 with raw rainfall, a) Gauge b) GPCP c) RCM. (d) is the time series of the RPC2 for the observations and the RCM.

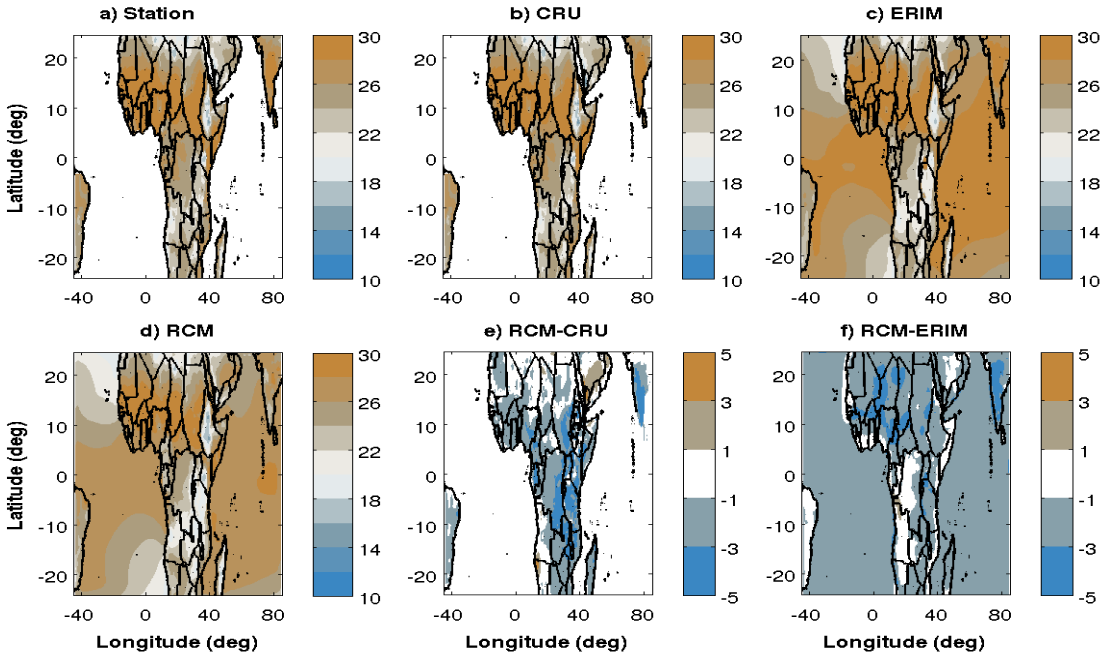

Fig. 4.8) Spring (FMA) season, mean (averaged 1982–2009) two-meter air temperature (in ^{o}C) ; a) Station b) CRU c)ERIM d) RCM e) bias of RCM minus CRU f) bias of RCM minus ERIM.

4.3.3. Temperature climatology and intra-annual variability

During spring (FMA) the station and observed CRU (mean 2-meter) temperature distribution (Fig. 4.8a, b) shows approximately a zonal pattern locating the lowest values (~14°C) in the north tip of Africa and complex terrain regions of Ethiopia, Tanzania, Angola and South Africa highlands. The highest values (30°C) are observed along the Sahel regions, in south Sudan and the south of Somalia. Mean spring temperature of ERIM shows similar patterns of observed dataset except a little warmer over north tip Africa and Ethiopian highlands (Fig. 4.8c). Spring climatology RegCM4 (Fig. 4.8d) temperature reproduces well this spatial pattern, but it extends area of minimum temperature slightly to the south from northern Africa. CRU gives more or less the same spatial distribution with RegCM4 simulation including a band of warm temperatures in the Sahel extending from West to East Africa. The temperature biases are low during spring season, although RegCM4 simulation tends to have cold bias around the complex terrains of southeast Africa and south of Sahel regions and warm bias over south of Saudi Arabia (Fig. 4.8e, f). Only few small regions exceed $\pm 2^{o}$C of bias (e.g. the southeast Africa regions).

The first dominant variability of temperature shown in Fig. 4.9 describes less representation of dominant pattern by the model. Even though, the dominant time component of model correlated better with corresponding CRU than ERIM with a correlation 0.87 and 0.71 respectively. Similarly, the second dominant RPC-2 of model temperature correlated well with CRU and ERIM (0.83 and 0.70) and the corresponding patterns (Fig. 4.10) captured the main temperature variability regions of Ethiopia.

Additionally the time series of observational temperature in each homogeneous regions are compared with respect to corresponding model simulation temperature. Temperature variability is also captured fairly and the summary is given in Table 4.2. The correlation of RCM with corresponding CRU areal averaged standardized temperature shows better than correlation between RegCM4 and ERIM over most sub-regions of Ethiopia (e.g. region 1, 4, 6, 7, 8, 9 and 10 in Fig. 2.1). We also notice station temperature time series are highly correlated with corresponding CRU temperature (correlation > 0.76). From this, we understand RegCM4 represents the observed variability by correcting the boundary forcing (ERIM).

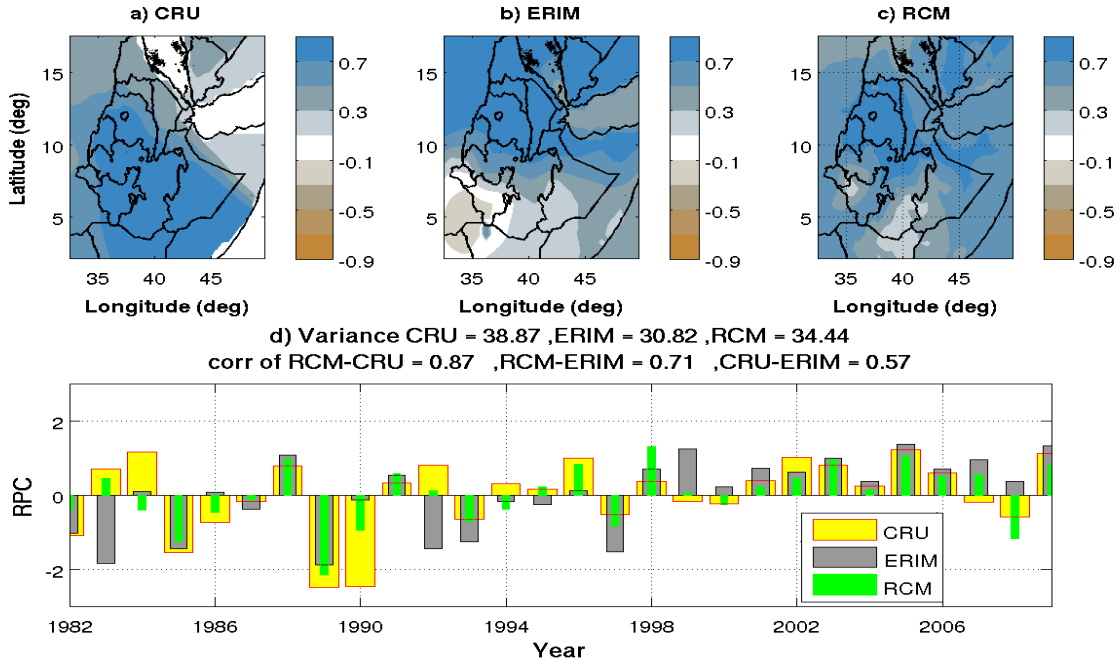

Fig. 4.9) Spring (FMA) season; correlation patterns of temperature first dominant RPC1 with raw temperature dataset, a) CRU b) ERIM c) RCM. (d) The time series of the RPC1 for the observation, reanalysis and the RCM.

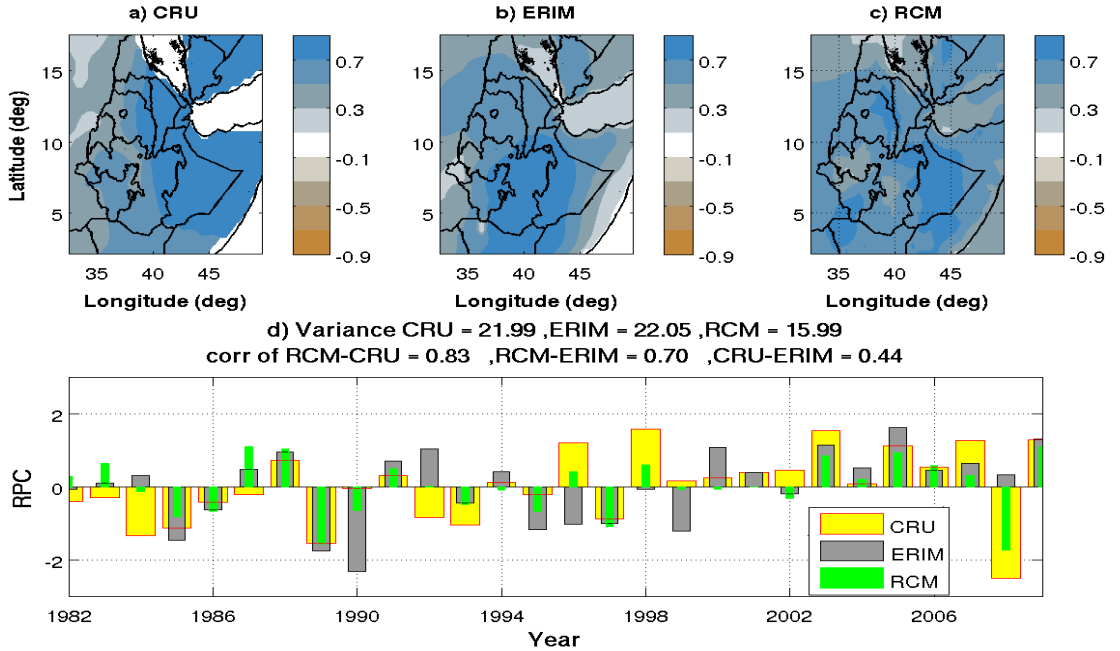

Fig. 4.10) Spring season; correlation of the second dominant temperature RPC2 with temperature of; a) CRU b) ERIM c) RCM. (d) The time series of the RPC2 for the observation, reanalysis and the RCM.

CRU temperature is better than ERIM to represent the observed variability with respect to station temperature as indicated in Table 4.2.

4.3.4. Summary

In this section, we evaluated the performance of RegCM4 in reproducing spring (FMA) climatology and intra-annual variability of large-scale circulation, precipitation and temperature variables over a large domain covering the entire African continent, with the model being driven by the recently produced ERIM reanalysis. We analyze climatological patterns of large-scale circulation (low-level horizontal wind averaged between 850-1000hPa, upper-level horizontal wind averaged between 100-300hPa and latitudinal cross-section (averaged between longitude 40W and 80E) of vertical profile horizontal wind, temperature over the whole domain and precipitation over Ethiopian region. The temporal variability of all variables is considered over Ethiopia and sub-regions of Ethiopia. The RegCM4 is able to capture very well the main circulations patterns that influence the Ethiopian climate during spring season such as STWJ and low-level horizontal wind coming from Atlantic and Indian Ocean, as well as Mediterranean Sea. The first dominant RPCs of these circulations are significantly correlated with the corresponding RPCs of model simulated wind fields (correlation > 0.8).

RegCM4 reproduces the climatology of rainfall very well over the southwest and eastern regions while it deteriorates towards north and northwestern tip regions. Maxima are well represented over complex terrains, although the model tends to overestimate precipitation over high mountain areas; although over these regions observed estimates may also be affected by a high uncertainty due to the paucity of high elevation stations. The model underestimates rainfall by small amount over the eastern regions of Ethiopia. Nevertheless, our simulation using RegCM4 is improved compared to that of previous RegCM3 studies over Ethiopia (e.g Segele et al. 2008) which was carried out using smaller domains and older reanalysis for the provision of lateral boundary conditions. Similarly, correlation of dominant RPCs and areal averaged standardized anomalies of each homogenous region indicated the performance of the model to represent the intra-annual variability of rainfall with respect to gauge dataset. We also noticed GPCP represented the observed spatial and temporal variability better than CRU precipitation.

The mean spring observed temperature over the simulation domain is captured relatively well by the model, although slight underestimates over topographic southeast and eastern African regions. The RegCM4 simulation captures relatively well the intra-annual variability of the temperature. The correlation values of dominant RPCs with respect to corresponding observations and areal averaged standardized temperature anomalies of each homogeneous regions with respect to corresponding observations confirms the improved performance of the model. CRU temperature is better correlated than ERIM in both RPCs and homogeneous regions time series with station temperature. We notice in case of temperature, evidently local model processes are more important than the lateral boundary forcing in determining the temperature variability.

Overall, the simulation analyzed here indicates good performance of the RegCM4 over Ethiopian region by representing multi-scale spatial and temporal variability of large-scale circulation, rainfall and temperature during spring season. This good performance (compared to previous model experiments) may be because of the new version of the model, the use of ERIM to produce lateral boundary conditions, domain size, convection scheme and some parameter values; which contributed to this improvement, even if the contribution of these variables are not identified.

4.4. Evaluation of RegCM4 during Summer Season

4.4.1. Characteristics of large scale circulation

In this section, we first examine the dynamical features of large-scale circulations in the model and reanalysis datasets during summer (JJAS). Comparison of ERIM and RegCM4 horizontal upper level winds (averaged between 100 and 300 hPa) indicates a strong similarity (Fig. 4.11a, b) in representing the location and strength of the TEJ core, even though the jet stream is slightly stronger in the model over regions south of Chad, Central African republic, central and eastern Ethiopia. The TEJ extends from Southeast Asia across the Indian Ocean towards northeast Africa, with the jet core positioned above 10° N over the Arabian Peninsula and eastern Africa, and tilted southward over central and western Africa.

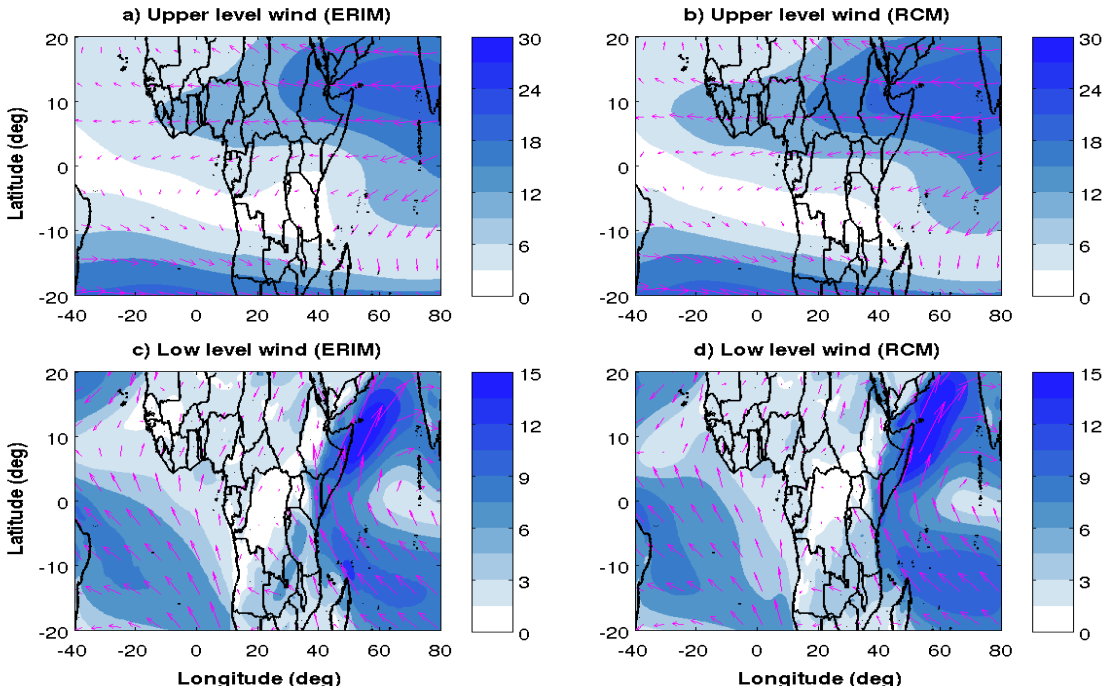

Fig. 4.11) Summer (JJAS) season mean horizontal wind: a) upper-level (averaged between 100-300hPa) wind (ERIM), b) upper-level (averaged between 100-300hPa) wind (RCM), c) low-level (averaged between 850-1000hPa) wind (ERIM), d) low-level (averaged between 850-1000hPa) wind (RCM).

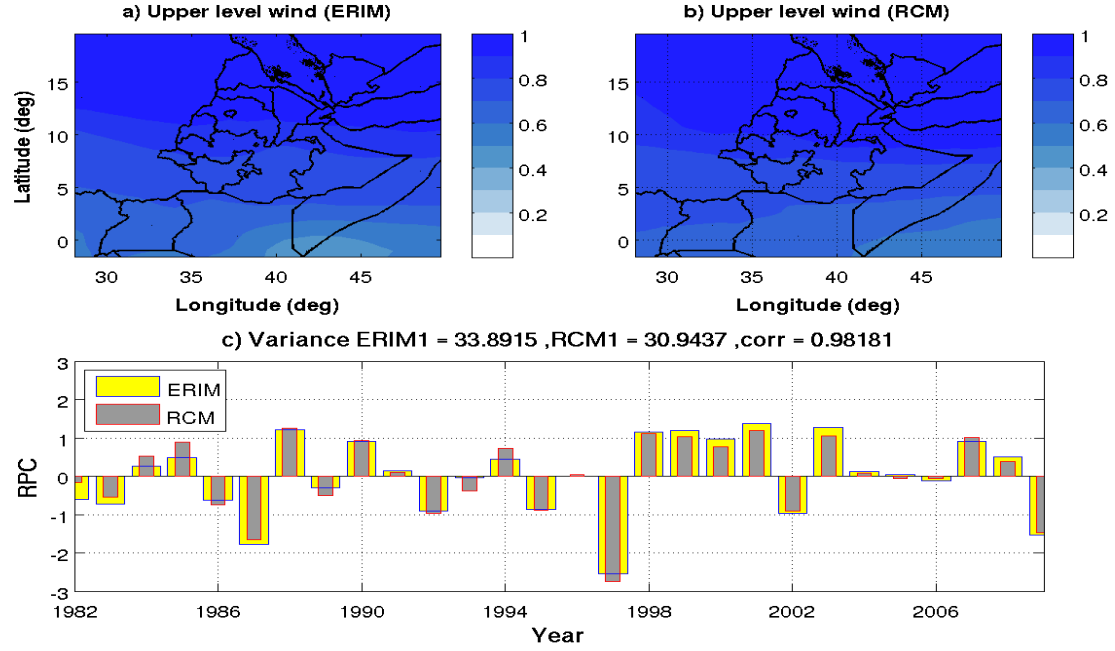

Fig. 4.12) Summer (JJAS) season; correlation patterns of upper-level (averaged between 100-300hPa) horizontal wind dominant RPC1 with raw upper-level horizontal wind a) ERIM b) RCM c) Dominant time scores.

The correlation between the time series of the wind field and the first rotated principal component (RPC-1) of the upper level wind (Fig. 4.12a, b) reveals that, the spatial pattern of the dominant mode of variability at upper levels is similar to the pattern of TEJ in both reanalysis and model simulation. Although in the model, the pattern is slightly shifted towards south over western and eastern regions of Ethiopia. The fraction of variance explained by the first REOF in the model (~31%); which is comparative with that of ERIM (~34%). The intra-annual variability of dominant region; RPC-1 in ERIM and RegCM4 (Fig. 4.12c) shows a good agreement (correlation value of ~0.98), and in particular, the extreme negative years (1987, 1992, 1995, 1997, 2002 and 2009) and positive years (1988, 1998/99, 2001 and 2003) are well captured. Figure 4.13 shows the pattern of dominant mode of variability for the latitudinal cross section of horizontal wind in ERIM and RegCM4 along with the time series of the leading RPCs. The first RPCs of the reanalysis and the model not only explain about a one third of the total variance (~37 and 35% of the total variance, respectively) but also correlate with each other significantly (correlation of RPCs ~0.97); suggesting a good agreement between ERIM and RegCM4 simulation. The pattern of dominant mode of variability indicated a strong positive correlation around 100-300hPa at 10^{o}S-20^{o}N which corresponds to the TEJ.

The low-level winds correlated oppositely over Ethiopian region, which is between ~0-5^{o}N and 10-15N. This low-level wind corresponds to the westerly monsoon flow. On the other hand, the strong negative correlation values at the upper levels (below 10°S) correspond to the subtropical westerly jet. In the mid-troposphere there is a north/south dipole pattern centered at about ~10° N that could be associated with the north/south shift of the AEJ. The low-level wind climatology for the summer season in ERIM and RegCM4 is shown in Fig. 4.11c, d. Like spring during summer season there is good agreement in both the magnitude and direction of the East African low-level jet. The patterns of the dominant mode of variability in the lower level wind of the ERIM reanalysis and RegCM4 are essentially identical (Fig. 4.14a, b) and show a positive loading over much of the East African domain and negative values over the boundary between southwest Ethiopia, southeast Sudan, and Kenya. The positive values over most of Sudan and Ethiopia correspond to the westerly flow from the Atlantic, and the values over the eastern Ethiopia, Somalia, and the coastal areas of east Africa are related to the Somali jet.

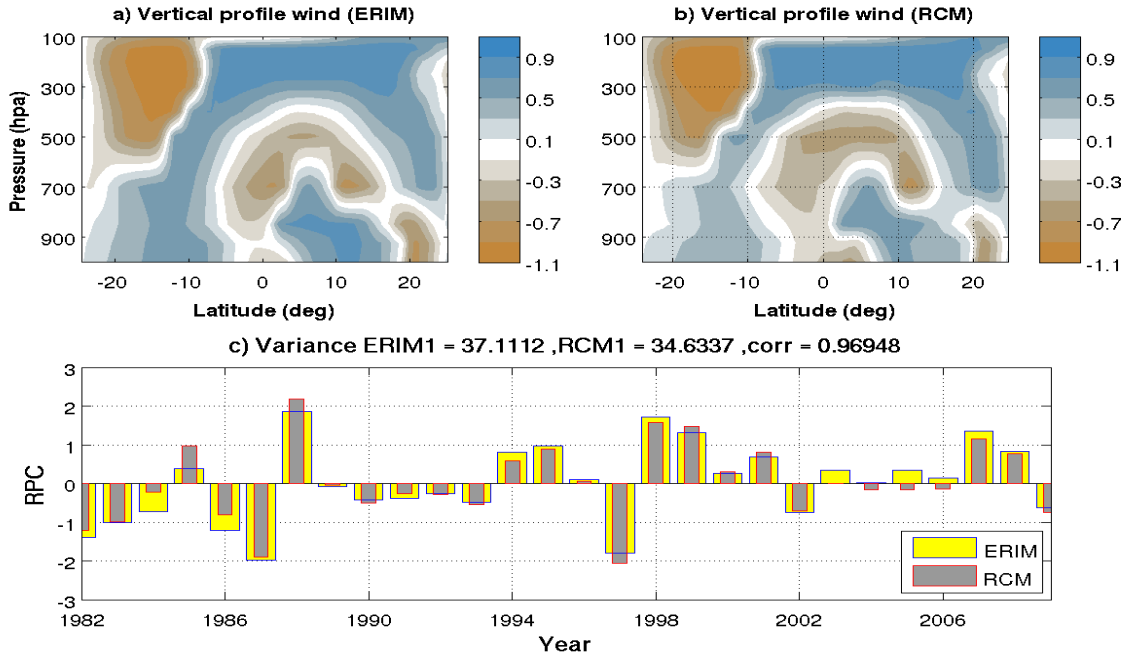

Fig. 4.13) Summer (JJAS) season; correlation patterns of mean (averaged in longitude wise from ~ 45W-85E) vertical profile horizontal wind dominant RPC1 with its raw dataset a) ERIM b) RCM c) Dominant time scores of both data sets.

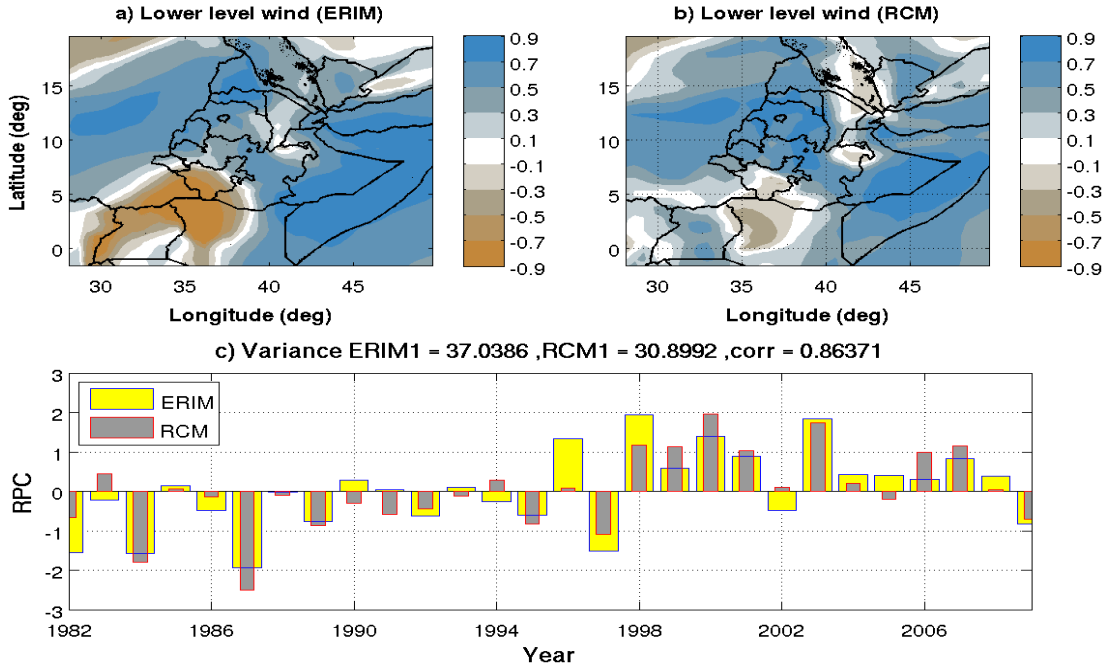

Fig. 4.14) Summer (JJAS) season; correlation patterns of low-level (averaged between 850-1000hPa) horizontal wind dominant RPC1 with raw low-level horizontal wind a) ERIM b) RCM c) Dominant time scores.

The negative correlation over the boundaries between southwest Ethiopia and Kenya could be due to the easterly anomaly associated with the Turkana Jet, which flows between the Ethiopian and East African highlands as the Somali jet diverges. The variances explained, by the first RPC of the reanalysis and model is ~37 and 38 %, respectively. The correlation between the low-level ERIM and RegCM4 wind is ~0.86; which shows the resemblance of the two time series (Fig. 4.14c).

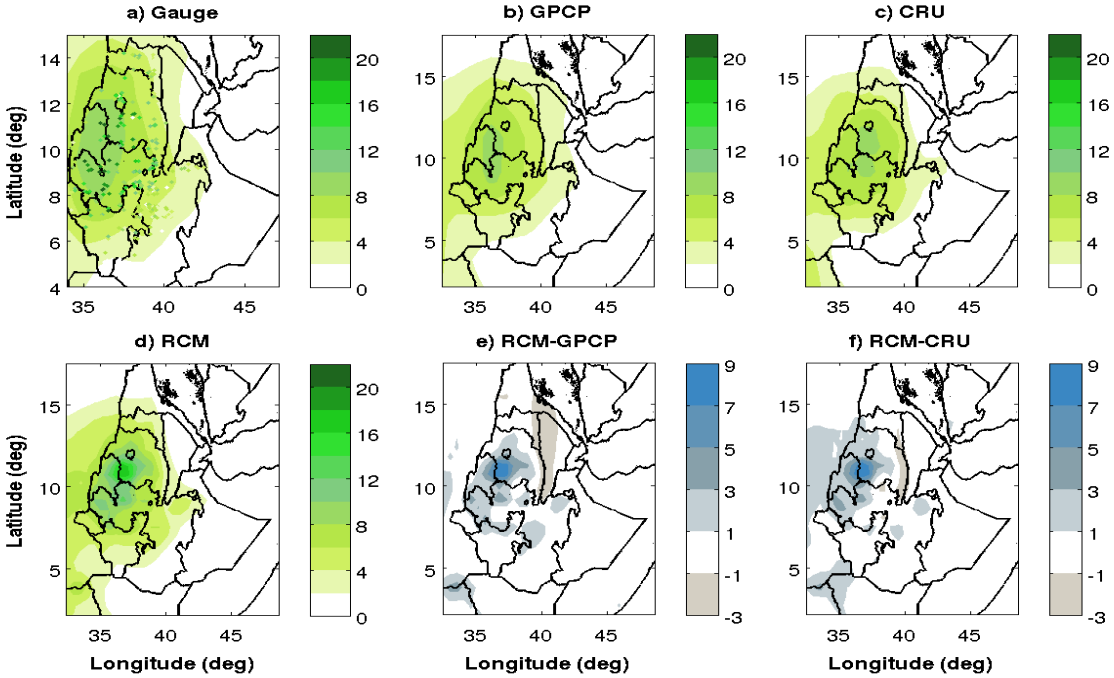

Fig. 4.15) Summer (JJAS) mean rainfall: a) Gridded and station rain (gauge). B) GPCP rain c) CRU rain d) RCM rain e) bias of RCM minus GPCP f) bias of RCM minus CRU.

4.4.2. Rainfall climatology, annual cycle, and intra-annual variability

In this section, we analyze the spatial patterns, annual cycle and intra-annual variability of summer (JJAS) rainfall over Ethiopia. Mean JJAS rainfall over Ethiopia for the period 1982–2009 shows that the northwestern, western, and central mountainous regions receive on average more than 12 mm/day of rainfall (see Fig. 4.15a, b, c, d). The northeastern, eastern, southeastern and southern regions, which are semiarid, receive comparably less precipitation during this season. The model reproduces reasonably well this climatological pattern of rainfall, although with positive and negative biases over the western mountainous regions and some isolated

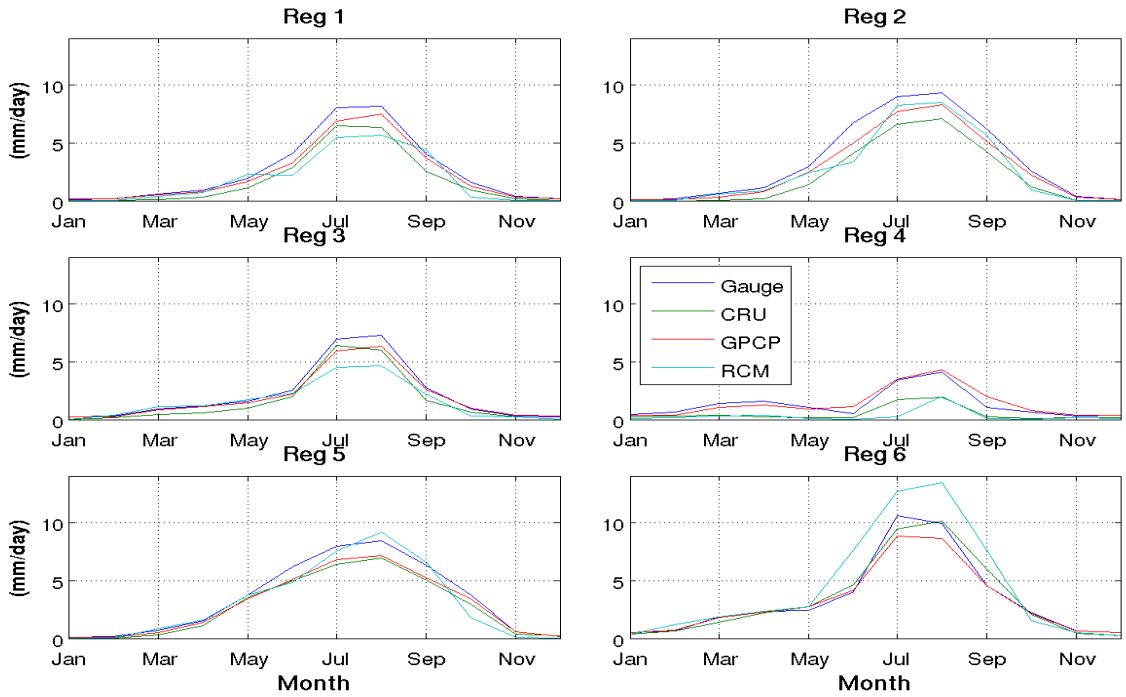

Fig. 4.16) Areal averaged of homogeneous regions seasonal rainfall or annual cycle (from Region-1 – Region-6).

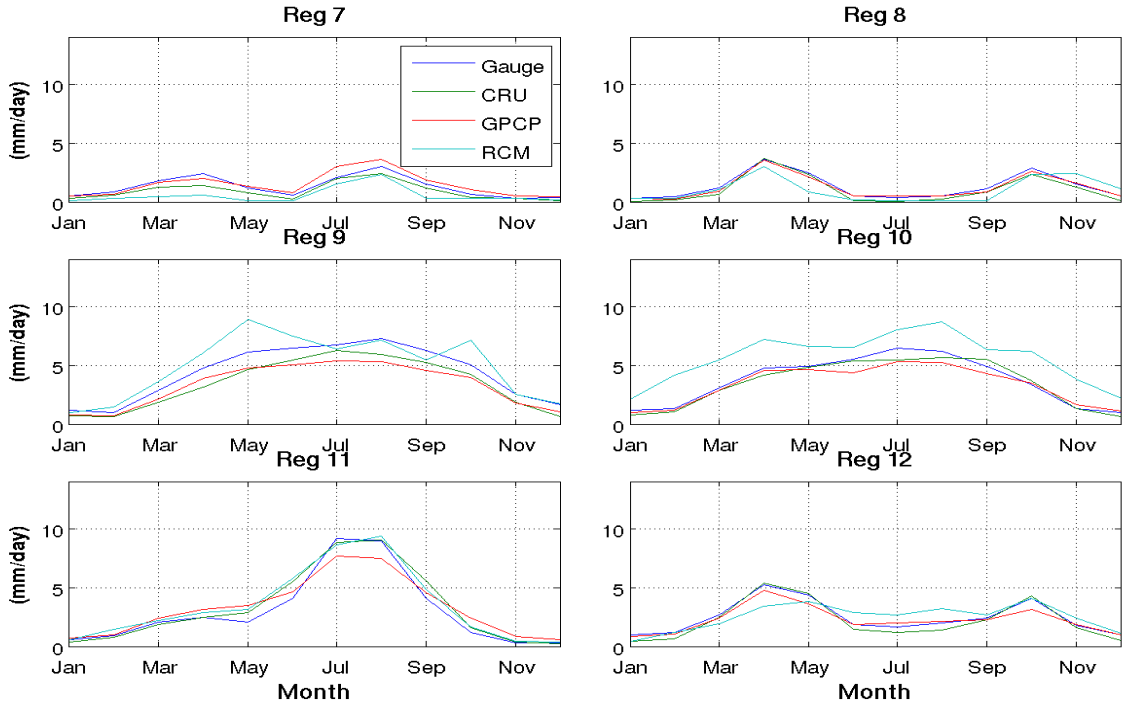

Fig. 4.17) Areal averaged of homogeneous regions seasonal rainfall or annual cycle (from Region-7 – Region-12).

lowland areas, respectively (Fig. 4.15e, f). We also note that the GPCP and CRU datasets show relatively low precipitation amounts over the northwest and west mountain regions.

Figure 4.16 and 4.17 show the mean annual cycle for the homogeneous rainfall regions of Fig. 2.1 using different sets of observations (gauge, GPCP and CRU) and RegCM4 simulation. The annual cycle values are averaged for each homogeneous region of Fig. 2.1 over the whole observation and simulation periods. Over regions 1 and 2, which are on the northwestern part of the country bordering with Eritrea and Sudan and lie west of the "Semien" mountain peak, some slight differences in the intensities among the observed and model estimates are observed. The model captures the unimodal precipitation cycle and the July-August maximum correctly and has better representation with respect to gauge for region 2 than GPCP and CRU dataset. For region five both observational and model dataset indicates uni-modal longer (March-November) rainy season in similar way. For regions 3 and 6, which lie over the "Semien Mountain," the model captures the summer monsoon rainfall and the pre- (May) and post-monsoon rain, with only a 1-month shift of peak rainfall and overestimate of peak months in region 6.

For region 4 in eastern Ethiopia, gauge, GPCP, and CRU observations exhibit a June break between the spring (FMAM) and summer (JAS) rain. The model captures this cycle except that the break between spring and summer is longer (June-July) and the rainfall amount is generally underestimated (compared to observational dataset, gauge). Over this region, gauge and GPCP are similar and RegCM4 and CRU underestimate spring and summer seasons. The eastern region 7; which shows bimodal similar to region 4 only differs by intensity of rainfall during summer season. All dataset including the simulation shows June as break between spring and summer season, with only small intensity difference among observational and RegCM4.

The double-rainy season structure is marked over region 8, with the two rainy seasons occurring in March–May and Mid-September–Mid-December. They are separated by a very dry season in June–September. This double-peaked structure is associated with a north–south migration of the ICTZ that sweeps this region (Diro 2008). All the observed and model datasets capture this structure, however with some variability in the phase and magnitude of the maxima. In particular, the RegCM4 underestimates the magnitude of the precipitation maxima during April-May and overestimates intensity of rainfall during November.

The southwestern regions of Ethiopia (i.e. region 9, 10) show unimodal, but longer rainy season almost throughout the year maximum between May-September. However, there is a wide spread in the magnitude and phase of the precipitation maxima across these datasets, with the gauge showing the largest magnitudes, GPCP the smallest and CRU some intermediate values. RegCM4 also captures well the long seasonality, unlike observational May as maxima and overestimate precipitation amounts throughout the year. The central Ethiopia (region 11) shows a precipitation peak in July/August, and the model captures the spring and summer rain whereas GPCP underestimate summer rain. Other southern (i.e. region 12) shows similar features to region 8, except amount of precipitation which differs throughout the year and with minimum precipitation during summer season. The model capture well the double peaked seasonal structure of this region but GPCP underestimates slightly the magnitude of rainfall of the second peak. Overall, RegCM4 performs well in reproducing the seasonal cycle of precipitation over all regions, except for an overestimation over the southwestern regions; where the rainfalls in almost all months is systematically underestimate over the eastern regions. We note that GPCP had better agreement in the magnitude and especially the phase of the rainy season peaks and corresponding breaks than CRU with respect to gauge dataset.

Fig. 4.18a, b, c shows the spatial patterns of correlation coefficient between the first dominant summer RPC1 of observational rainfall and the corresponding raw summer mean rainfall time series at each grid point over Ethiopian region. According to the result the northeastern regions have high coefficient of variation in rainfall during summer season. The variance explained over this region is ~28%, ~24% and ~25% of the total variance using gauges, GPCP and RegCM4 simulation respectively. The pattern of gauge (Fig. 4.18a) is wider when we compare with respect to GPCP and RegCM4 simulation (Fig. 4.18b, c). The model shows significant negative correlation over small western regions of Ethiopia, unlike gauge and GPCP. The corresponding rotated principal component (RPC1) of RegCM4 significantly correlated with RPC1 of gauge (correlation between RPC1s of gauge and RegCM4 is ~0.83). Similarly, RegCM4 RPC1 correlated significantly with GPCP of RPC1 (correlation between them is ~0.84) and the two observational RPCs (gauge and GPCP) correlated with a magnitude of ~0.89. RegCM4 also captured correctly the extreme positive years (e.g. 1988, 1998 and 2001) and extreme negative years (e.g. 1984, 1987, 1990 and 2009).

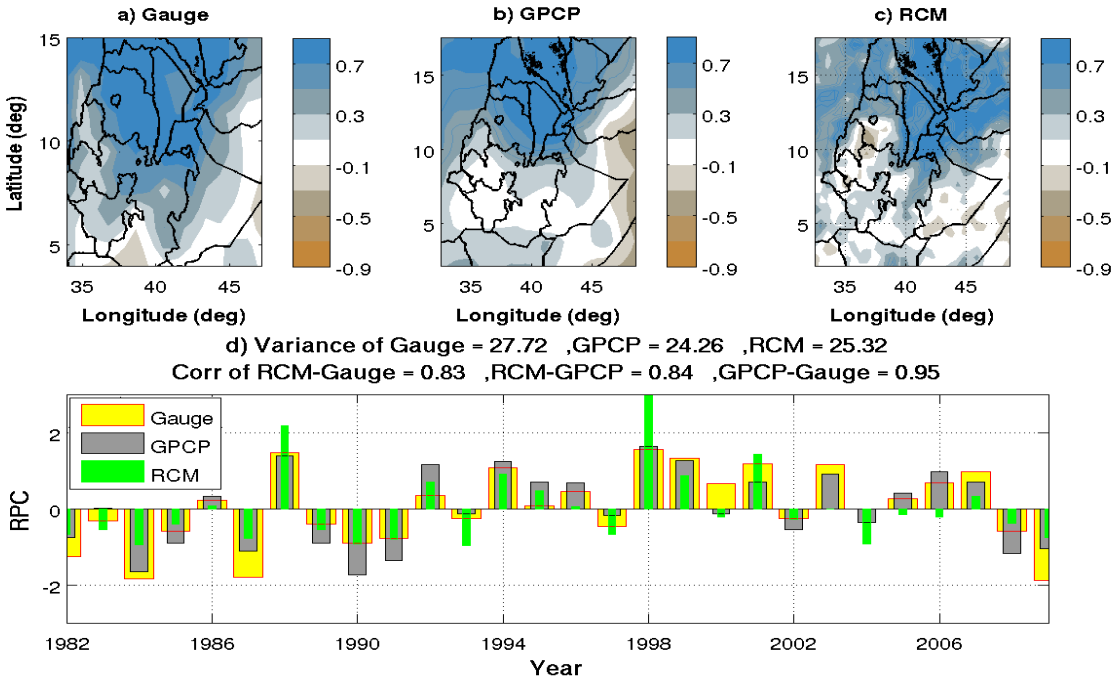

Fig. 4.18) Summer season; correlation patterns of rainfall first dominant RPC1 with raw rainfall dataset, a) Gauge b) GPCP c) RCM. (d) The time series of the RPC for the observations and the RCM.

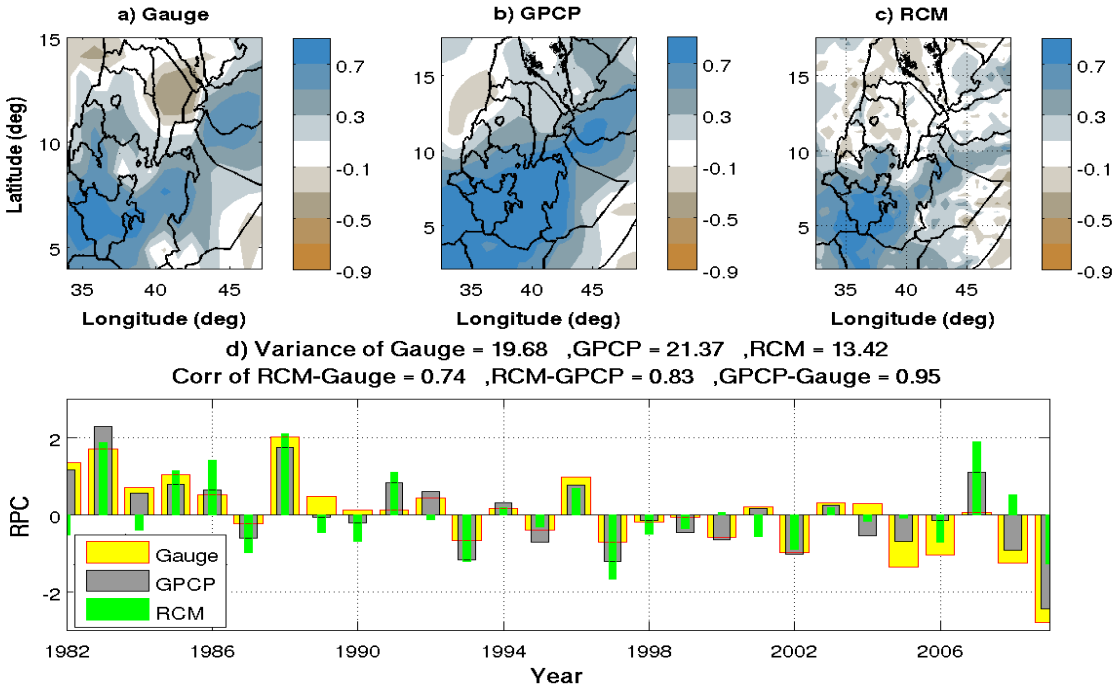

Fig. 4.19) Summer season; correlation patterns of rainfall second dominant RPC2 with raw rainfall dataset, a) Gauge b) GPCP c) RCM. (d) The time series of the RPC for the observations and the RCM.

The second patterns of correlation between second RPC2 of rainfall and summer mean rainfall by gauge, GPCP and RegCM4 are shown in Fig. 4.19a, b and c respectively. The patterns in all dataset indicate a strong correlation over southwestern Ethiopia. About 20%, ~21% and ~13% variances are explained by the patterns out of total variance over southwestern region using gauge, GPCP and RegCM4 respectively. The variance explained by RegCM4 over this region is smaller than observational dataset and gauge RPC2 negatively correlated with corresponding rainfall over northeastern region unlike GPCP and RegCM4. The second RPCs are significantly correlated with each other with correlation between RegCM4-RPC2 and gauge-RPC2 to be ~0.75, correlation between RegCM4-RPC2 and GPCP-RPC2 to be ~83 and correlation between gauge-RPC2 and GPCP-RPC2 to be ~0.89. The positive extreme years (example 1983, 1988, 1996 and 2007) and negative years (example 1997, 2002, 2008/09) are captured by RegCM4 simulation correctly.

Table 4.1 summarizes the correlation coefficients between simulated and observed rainfall anomalies over the 12 climate sub-regions of Fig. 2.1 during summer season.

Table 4.1. Spring and summer seasons; correlation of standardized anomalies of observed and simulated rainfall for each Ethiopian region. Bold figures represent values that are statistical significant at 0.05 level.

Region	RCM vs GPCP		RCM vs merged-gauge		RCM vs CRU	
	Spring	Summer	Spring	Summer	Spring	Summer
1	**0.62**	**0.62**	**0.61**	**0.67**	0.43	0.44
2	**0.66**	0.43	**0.71**	0.15	0.39	0.46
3	**0.79**	**0.57**	**0.73**	**0.64**	**0.49**	**0.48**
4	**0.61**	**0.81**	0.37	**0.49**	0.47	0.23
5	**0.79**	**0.54**	**0.79**	0.36	0.19	0.26
6	**0.91**	**0.62**	**0.87**	**0.51**	0.32	0.24
7	**0.75**	**0.84**	**0.71**	**0.78**	**0.49**	0.47
8	**0.51**	0.47	0.36	0.43	**0.63**	0.22
9	0.44	**0.66**	0.31	0.39	0.26	**0.51**
10	**0.57**	**0.62**	**0.49**	0.42	0.21	0.46
11	**0.98**	**0.81**	**0.87**	**0.68**	0.32	**0.51**
12	**0.58**	**0.71**	**0.65**	**0.58**	0.39	**0.61**

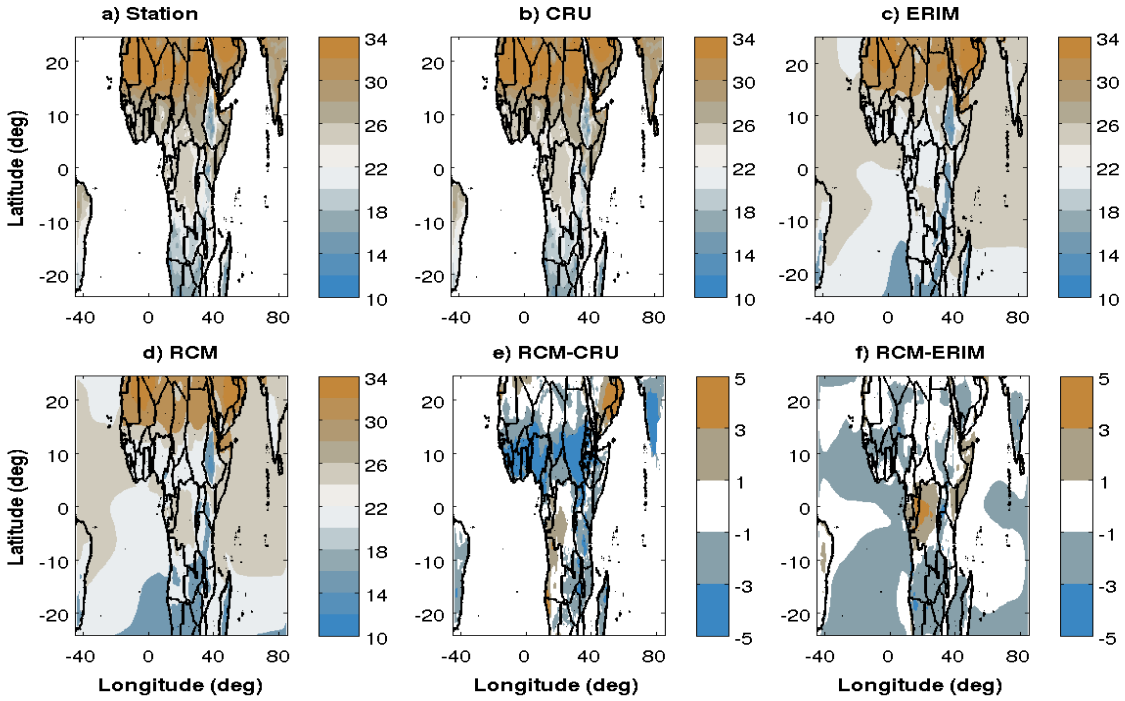

Fig. 4.20) Summer (JJAS) mean (averaged 1982–2009) two-meter air temperature (in ^{o}C), a) Station b) CRU c)ERIM d) RCM e) bias of RCM minus CRU f) bias of RCM minus ERIM.

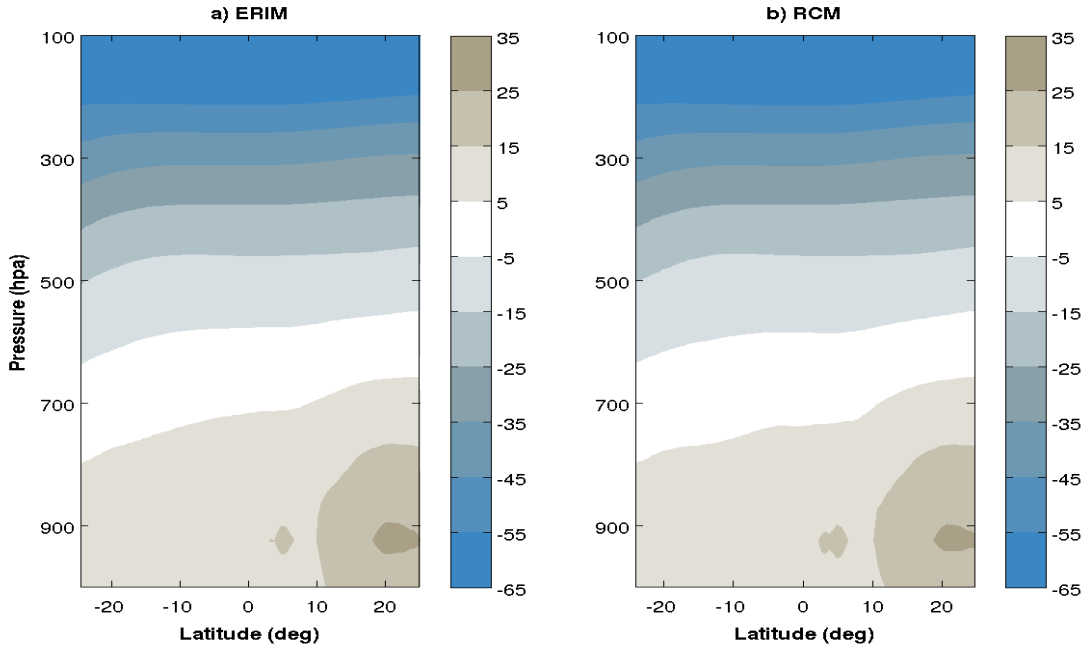

Fig. 4.21) Summer (JJAS) season; mean (averaged in longitude between ~ 32-50E) vertical profile temperature a) ERIM b) RCM.

The anomalies are calculated with respect to the precipitation mean derived from the full 28 year period 1982–2009. The area averages of precipitation anomalies are normalized by the standard deviation derived from the 1982–2009 time series. Observed summer rainfall anomalies for each region are generally well correlated with the corresponding model rainfall anomalies, as shown in the correlation analysis of Table 4.1. In particular, observed and simulated rainfall anomalies are highly correlated over the central highland areas and southwestern, southern, and northern regions, while the lowest correlation is found over the border regions of the country (zone 2). The correlations (Table 4.1) show a significance level of 95%, indicating that there is good agreement between model and observations. Over these regions the RegCM4 simulation generally captures well both the occurrence of individual anomalies (correlation coefficients of >~0.6) as well as the magnitude of intra-annual variability in all these sub-regions. However, a few exceptions are found in some regions where the correlations are relatively low (Table 4.1).

4.4.3. Temperature climatology, annual cycle, and intra-annual variability

Fig. 4.20a, b, c, d, e, f shows the summer average 2 m temperature; which is derived from the full 28 year period 1982–2009 from station, CRU, ERIM and RegCM4 as well as the bias patterns (RegCM4-CRU and RegCM4-ERIM) respectively. The result indicates lower temperature over southern Africa and increasing towards northern Africa, except Ethiopian and eastern Africa mountainous regions. During this season, maximum temperature (≥ 34) is observed over northern tip of Africa. The hot pattern regions of ERIM and RegCM4 are more confined in the northern regions of Africa with respect to observation dataset. The observed patterns are reproduced well except cold bias over Sahel and East African mountainous regions and warmer bias over Saudi Arabia (Fig. 4.20e). With respect to reanalysis (ERIM) dataset, RegCM4 simulation reproduces the pattern with only warmer bias over Democratic republic of Congo, Congo Brazzaville and Gabon (Fig. 4.20f). The cold bias observed with respect to CRU is reduced with respect to ERIM. Note that the underestimation of temperature over the complex terrain of southeast Africa may lead to an increased north-south temperature gradient between this regions and the Sahara, which may be responsible for the stronger monsoon flow and the

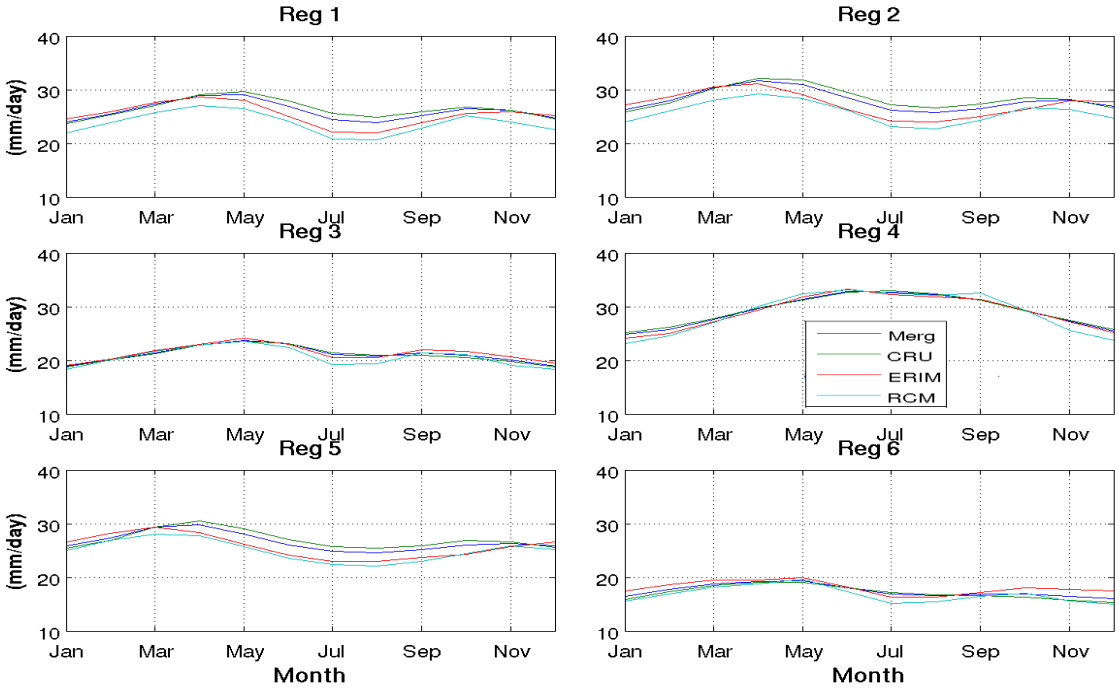

Fig. 4.22) Areal averaged of homogeneous regions seasonal temperature or annual cycle (from Region-1 – Region-6).

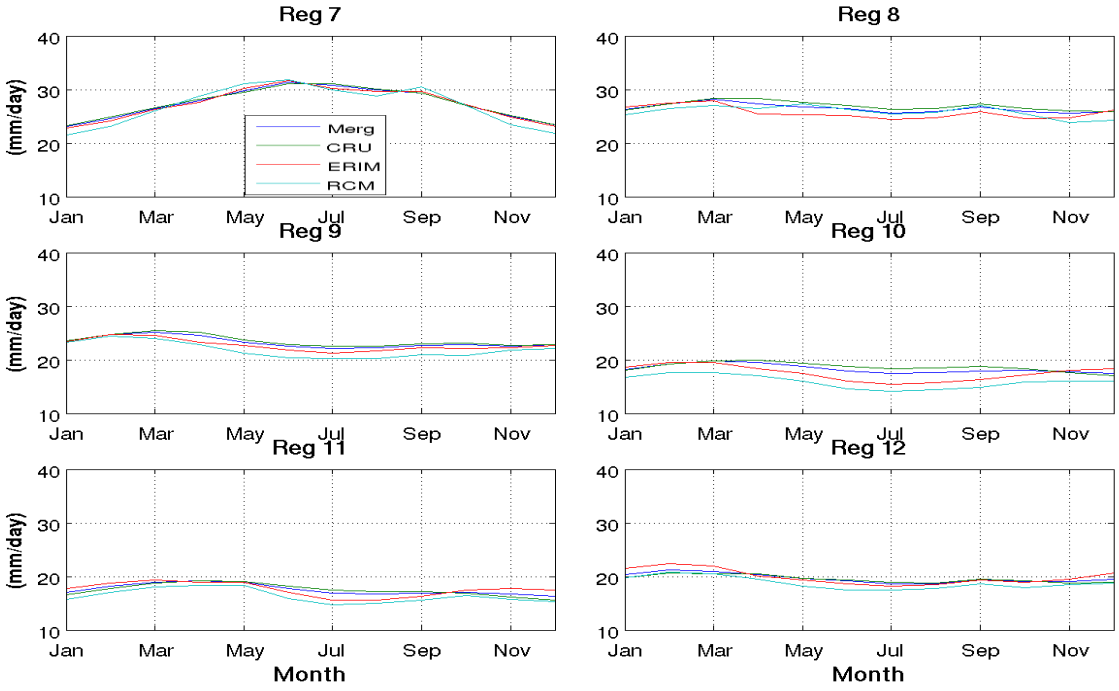

Fig. 4.23) Areal averaged of homogeneous regions seasonal temperature or annual cycle (from Region-7-Region-12).

slight shift of the TEJ core found in the regional model. Overall, the climatology of summer 2-meter temperature is reproduced well by the RegCM4 simulation. Both observational and model locate peaks of high temperatures in the Sahara desert and the lowest temperatures over orographic regions of east Africa. Fig. 4.21a, b shows the mean vertical profile of temperature averaged longitude (~ 32E-50E) from ERIM and model simulations. The result confirms that the model reproduced this pattern except little shift towards the ground below ~500hPa, even though above ~500hPa the patterns are similar. Both ERIM and model shows highest (35^{o}C) temperature around 900hPa at ~20^{o}N and lowest (negative 65^{o}C) temperature at a height of 100hPa throughout the latitude domain.

Additionally the mean areal annual cycle temperature over the whole period of station and CRU merged, pure CRU, ERIM and model simulation for each homogeneous regions (Fig. 2.1) are compared. Region 1, 2, 3, 5 and 6 in Fig. 4.22 show similar temperature cycle; which is bimodal maximum in May and October and minimum in July and December/January, which only differ in magnitude of temperature. For example, the temperature decreases from region 2, region1, region 5, region 3 and region 6 consecutively. May is the hottest and July/December is the coldest months over the regions. Region 4 shows a mono-modal temperature cycle; maximum (~36^{o}C) in July and minimum (~25^{o}C) in December for all dataset. Region 7 (Fig. 4.23) which is similar with region 4 only shifts the maximum (~32^{o}C) month to June and minimum (~22^{o}C) on December. The Central and southern regions (regions 8, 9, 10, 11 1nd 12) show similar temperature throughout the year which differs only in magnitude. For example, region 10, 11 and 12 are colder than region 9 which shows on average ~19^{o}C and 23^{o}C in all months respectively. Region 8 also shows constant temperature ~27^{o}C through-out the year. All dataset are consistent over all sub-regions of Ethiopia.

Area averaged temperature anomalies for which normalized by corresponding standard deviation are calculated for 12 homogeneous regions (Fig. 2.1). Table 4.2 summarizes the correlation coefficients between simulated and observed temperature anomalies over the homogeneous regions. The intra-annual variability of RegCM4 temperature agrees with observational than ERIM over region 2, 5, 6, 9, 10, 11 and 12 (Table 4.2).

Table 4.2. Spring and summer seasons; correlation of standardized anomalies of observed and simulated temperature for each Ethiopian region. Bold figures represent values that are statistical significant at 0.05 level.

Region	RCM vs ERIM		RCM vs station)		RCM vs CRU	
	Spring	Summer	Spring	Summer	Spring	Summer
1	**0.85**	**0.67**	**0.93**	**0.67**	**0.85**	**0.55**
2	**0.81**	**0.62**	**0.81**	**0.74**	**0.71**	**0.65**
3	**0.88**	**0.77**	**0.74**	**0.71**	**0.77**	**0.53**
4	0.41	**0.53**	**0.66**	**0.48**	**0.76**	0.45
5	**0.62**	0.41	**0.65**	**0.69**	0.44	**0.71**
6	**0.58**	**0.84**	**0.85**	**0.89**	**0.81**	**0.83**
7	0.41	**0.51**	**0.61**	**0.51**	**0.64**	0.31
8	**0.59**	**0.69**	**0.57**	**0.61**	**0.66**	**0.57**
9	0.31	0.25	0.45	**0.77**	**0.51**	**0.71**
10	**0.56**	**0.49**	**0.65**	**0.81**	**0.59**	**0.76**
11	**0.78**	**0.83**	**0.82**	**0.89**	**0.75**	**0.85**
12	**0.72**	**0.53**	**0.65**	**0.64**	**0.51**	**0.61**

The dominant variability of summer 2-meter temperature shown in Fig. 4.24 and 4.25 confirms the performance of the model to reproduce the observed variability of temperature. However, there is a slight difference for temperature between the ERIM, CRU and model simulation dataset. We realize that even if the boundary values of temperature have slight different from both merged observation and CRU; the model corrected the observed differences between observation and reanalysis dataset. We also note that the intra-annual variability of CRU is much better correlated with station-based dataset than ERIM.

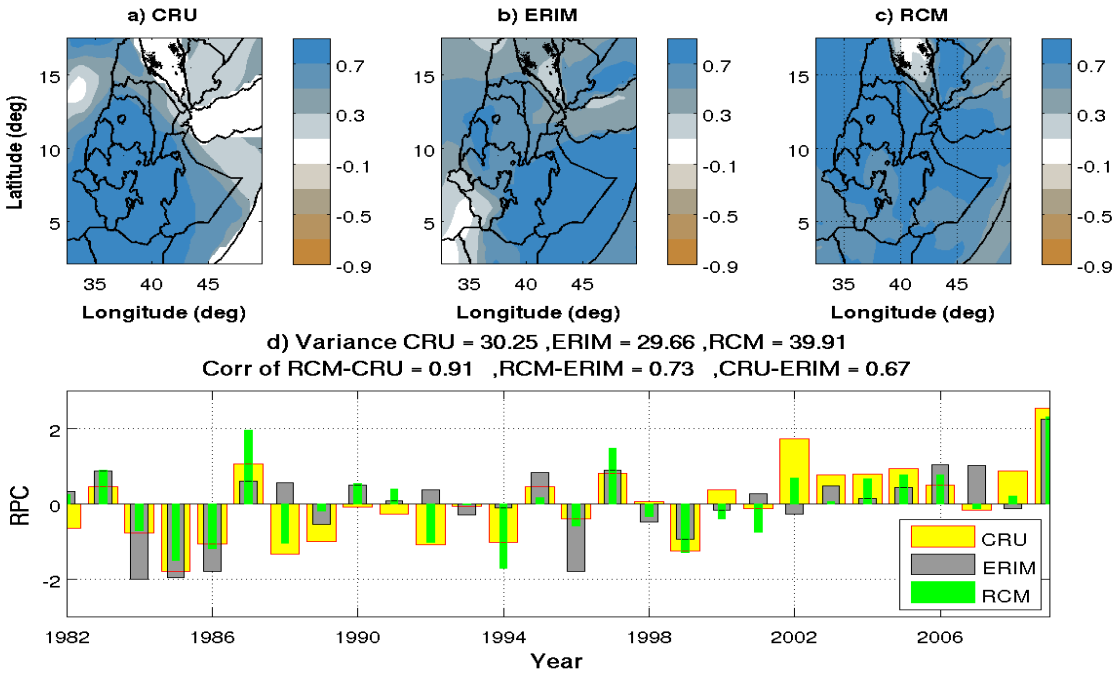

Fig. 4.24) Summer season; correlation patterns of temperature first dominant RPC1 with raw temperature dataset; a) CRU b) ERIM c) RCM. (d) The time series of the RPC for the observation, reanalysis and the RCM.

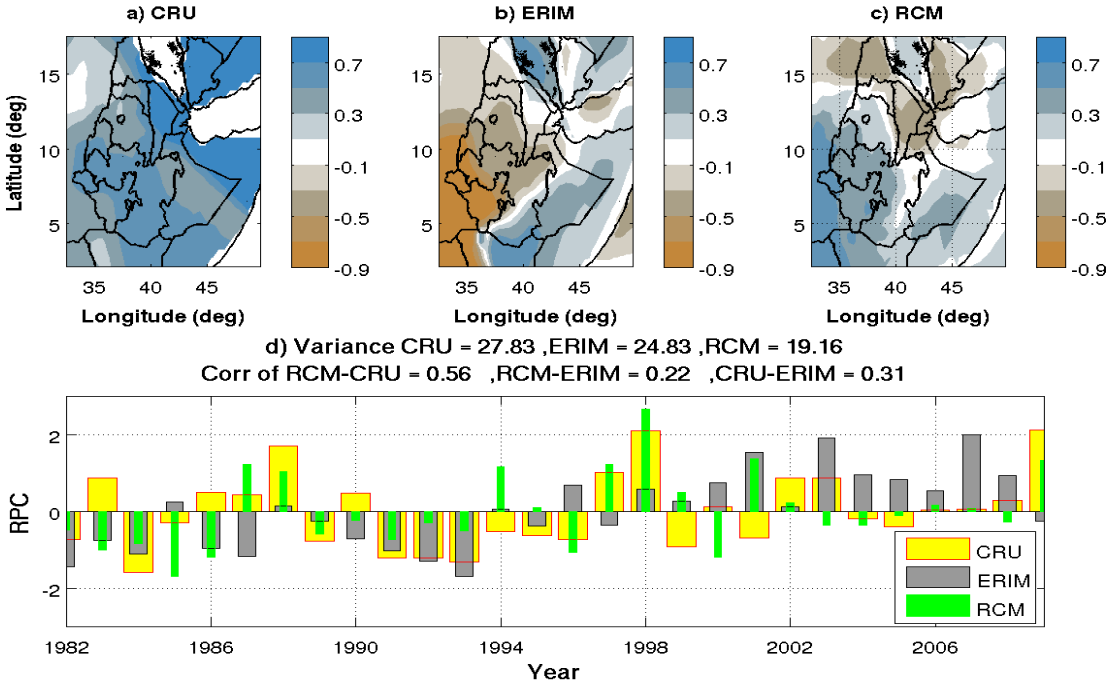

Fig. 4.25) Summer season; correlation patterns of temperature second dominant RPC2 with raw temperature ; a) CRU b) ERIM c) RCM. (d) The time series of the RPC for the observation, reanalysis and the RCM.

4.4.4. Summary

In this section, we investigated the ability of the RegCM4 to simulate the multi-scale spatial and temporal variability of large-scale circulation, rainfall and temperature for summer season. The main large-scale circulation that connected with the generation of rainfall during summer season over Ethiopia like TEJ, AEJ and EALLJ are realistically simulated. Comparison of ERIM and RegCM4 horizontal upper level winds (averaged between 100 and 300 hPa) indicates a strong similarity in representing the location and strength of the TEJ core, even though the jet stream is slightly stronger in the model over regions of south Chad, Central African republic, central and eastern Ethiopia. Model simulated low-level horizontal wind has a good agreement during summer season with reanalysis wind dataset in both the magnitude and direction over Ethiopia. The correlation of simulated and ERIM first dominant rotated principal components of upper level horizontal winds are significant and high in magnitude (~0.98) and similar patterns of REOFs show the ability of the model to capture the features of this wind, which connected highly with rainfall variability over most of Ethiopian regions during summer season. The low-level horizontal wind similarity of spatial patterns of dominant variability and high magnitude correlation (~0.86) of the corresponding RPCs confirms the performance of the model to capture the main features of rain generating mechanisms over Ethiopia.

Ethiopian summer climate variability from different observation datasets along with the performance of the regional climate model (RegCM4) in reproducing this variability is also assessed. The observed rainfall datasets indicate that the western mountainous regions of Ethiopia receive rainfall in excess of 12 mm/day during the summer season, with this amount decreasing towards the bordering regions following the slopes of the western and eastern plateaus (e.g. northeastern, southeastern and southern tip of the country). This observed climatology of summer rainfall reproduced fairly with exception of overestimate around “Semine Mountains” and underestimate over semi-arid low lands.

The mean annual cycle for the homogeneous rainfall regions using different sets of observations (gauge, GPCP and CRU) and RegCM4 simulation shows RegCM4 performs well in reproducing the seasonal cycle of precipitation over all regions, except for an overestimation over the southwestern regions; where the rainfalls in almost all months and systematically

underestimate the eastern regions. We note that GPCP had better agreement in magnitude and especially the phase of the rainy season peaks and corresponding breaks than CRU with respect to gauge dataset.

The correlation coefficients between simulated and observed rainfall anomalies normalized by the standard deviation over the 12 climate sub-regions during summer season and between the first two dominant RPCs show the ability of RegCM4 simulation to reproduce intra-annual variability of rainfall over Ethiopian regions. The first dominant pattern observational dataset which explain the northeast region is captured correctly by RegCM4 simulation with corresponding RPCs significant correlation (correlation > 0.82). Similarly, the second dominant variability regions (southwestern of Ethiopia) are simulated fairly with significant correlation of corresponding RPCs including extreme years.

Climatology of temperature during summer season reproduced realistically with slight underestimate over east Africa mountainous and Sahel regions and overestimate around Saudi Arabia. The significant and high magnitude correlation coefficients of standardized anomalies of temperature over each homogeneous region of Ethiopia and dominant RPCs of temperature confirm the ability of the model to reproduce intra-annual variability of temperature. We also note that CRU temperature is much more linked with station temperature than ERIM.

Overall RegCM4 reproduce summer spatial and temporal variability of large-scale circulation, rainfall and temperature realistically. The variability of rainfall are estimated better by GPCP than CRU with respect to gauge and CRU temperature much more correlated with station dataset to estimate the observed variability.

4.5. Conclusion

We have performed evaluation of the RegCM4 simulated rainfall over Ethiopia, temperature, wind field and pressure over Africa during spring and summer seasons. The ability of the model to capture the variability of these variables is reasonably consistent with observations in both seasons. The simulated climatologies and intra-annual variability of different homogeneous climate sub-regions of Ethiopia are consistent with the observed

variables in representing these sub-regions of the country. In particular, the model reasonably reproduces the observed rainfall, wind field and pressure climatology and intra-annual variability during both seasons. Conversely, the model has evidently weak representation of variability of temperature during both seasons with respect to station temperature and CRU temperature and better with respect to ERIM. This shows that temperature variability is depends more on local process, hence RegCM4 correct the temperature and make it to have better representation of observed variability.

CHAPTER - FIVE

Spatial and Temporal Multi-Scale Variability of Drought Over Ethiopia Using Drought Indices Derived From Observational and Regcm4

At this point, we understand multi-scale spatial and temporal variability of rainfall and temperature over Ethiopia. This is an interesting and important for the development of drought indicators and it helps to analyze the characteristics of drought in different sub-regions of Ethiopia. In this chapter, we discuss in detail the multi-scale temporal and spatial characteristics of drought over Ethiopia. Furthermore, we quantify the intensity of dryness using most popular drought indicators such as SPI3, SPI12 and PDSI driven from both observational and model simulation dataset.

5.1. Features of drought events over Ethiopia

Trend Empirical Orthogonal Function (TEOF) was applied on the SPI12 and PDSI indices which are derived from observational and model simulation atmospheric variables. Observing the results from the Trend Principal Component (TPC) and taking into account the trend patterns explained by each TPC, the first two trend patterns (TEOF-1 and TEOF-2) were identified from SPI12 and PDSI indices. These trend patterns in SPI12 and PDSI indices explain more than 60%, 36% of the total trend patterns for both observation and model simulation. The dominant patterns (TEOF-1) of SPI12 (Fig. 5.1a, b) and PDSI (Fig. 5.2a, b) indicate a positive pattern over the southern region and a negative pattern over the northwestern border area. This mode describes mainly the southern regions and explains more than 1/3 of the observed trend pattern and around 1/5 of the model-derived trend based on correlation patterns of TPC-1 and raw indices (not shown here). The corresponding TPCs are characterized by negative trend superimposed with low frequency high power signals (Fig. 5.1c, d and Fig. 5.2c, d). These

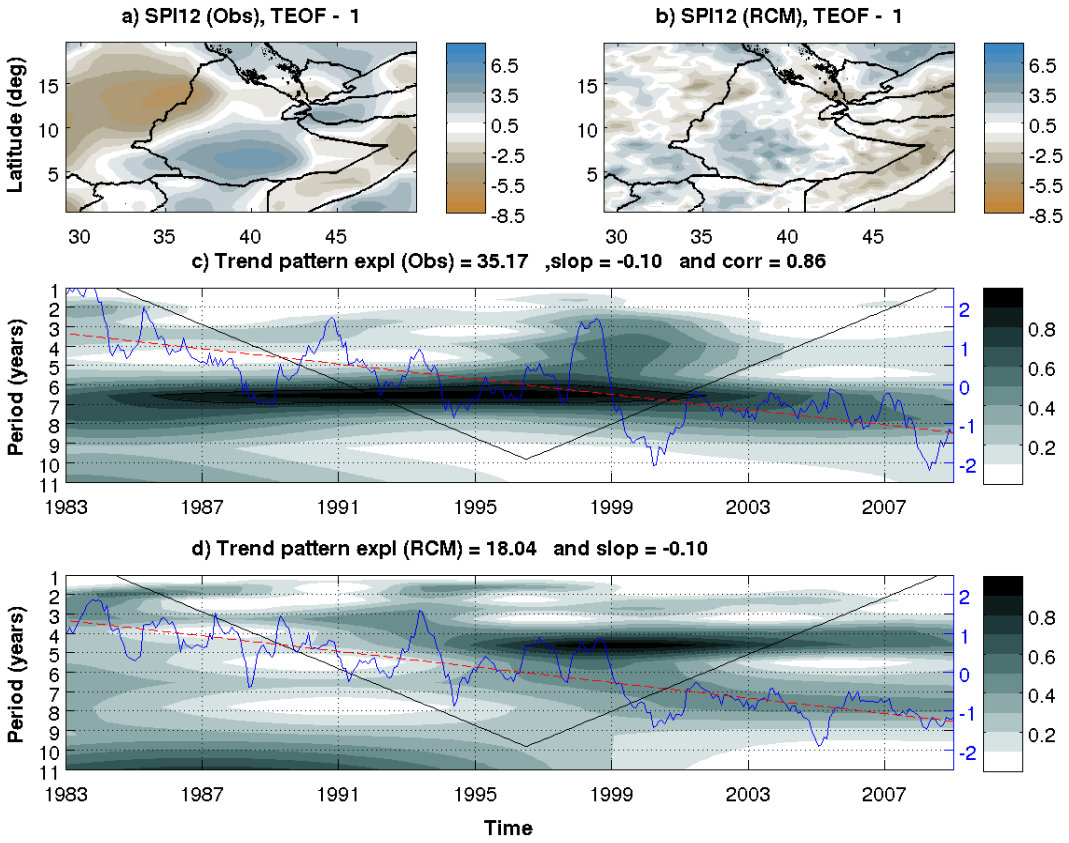

Fig. 5.1) Trend Emeperical orthogonal function (TEOF-1); a) SPI12 driven from observation b) SPI12 driven from RegCM4 c) TPC-1 of SPI12 (observation, blue solid line) with trend (red broken line which is linear fit of TPC-1) and wavelet analysis. d) TPC-1 of SPI12 (RegCM4, blue solid line) with trend (red broken line which is linear fit of TPC-1) and wavelet analysis.

TPCs indicate sudden changes especially during ~1997-2000 and more frequent and intense dry events are observed after wards. The wavelet analysis of observational SPI12 and PDSI dominant TPCs which indicates the 95% confidence region is consistently distributed in the ~6-7 year's high power periodic waves during ~1992-2000 in both observational indices and 4-5 year's high power periodic waves during 1995-2003 in the model driven SPI12. During ~1997-2000, different (2-8years) periodic high power signals are detected in TPC-1s computed from observation indices (Fig. 5.1c and Fig. 5.2c); which may explain the observed sudden change in this time series around 1990-2000. Although, periodic signals of TPC-1 of PDSI is less power when we compare with TPC-1 of SPI12. The observed trend pattern difference in some regions between SPI12 (Fig. 5.1) and PDSI (Fig. 5.2) computed from observational and RegCM4 are quite natural, given the difference in their formulation. SPI12 is calculated only from the

precipitation records whereas the PDSI is based on the supply-and-demand concept of the water balance equation taking into account precipitation, temperature and available water content of soil. Therefore, it is clear that the level of significance of trends may differ between PDSI and SPI12 drought indices. The RegCM4 driven PDSI and SPI12 dominant trend patterns and the corresponding time components are consistent with observation driven indices. For instance, the temporal correlations of the first TPC's (TPC-1) between indices derived from the model and observation are 0.86 and 0.87 for SPI12 and PDSI respectively. In addition to the trend component characteristics, the periodic signals and inter/intra-annual variability drought explained by the first dominant TEOF and corresponding time component are simulated fairly well (Fig. 5.1b, d and Fig. 5.2b, d).

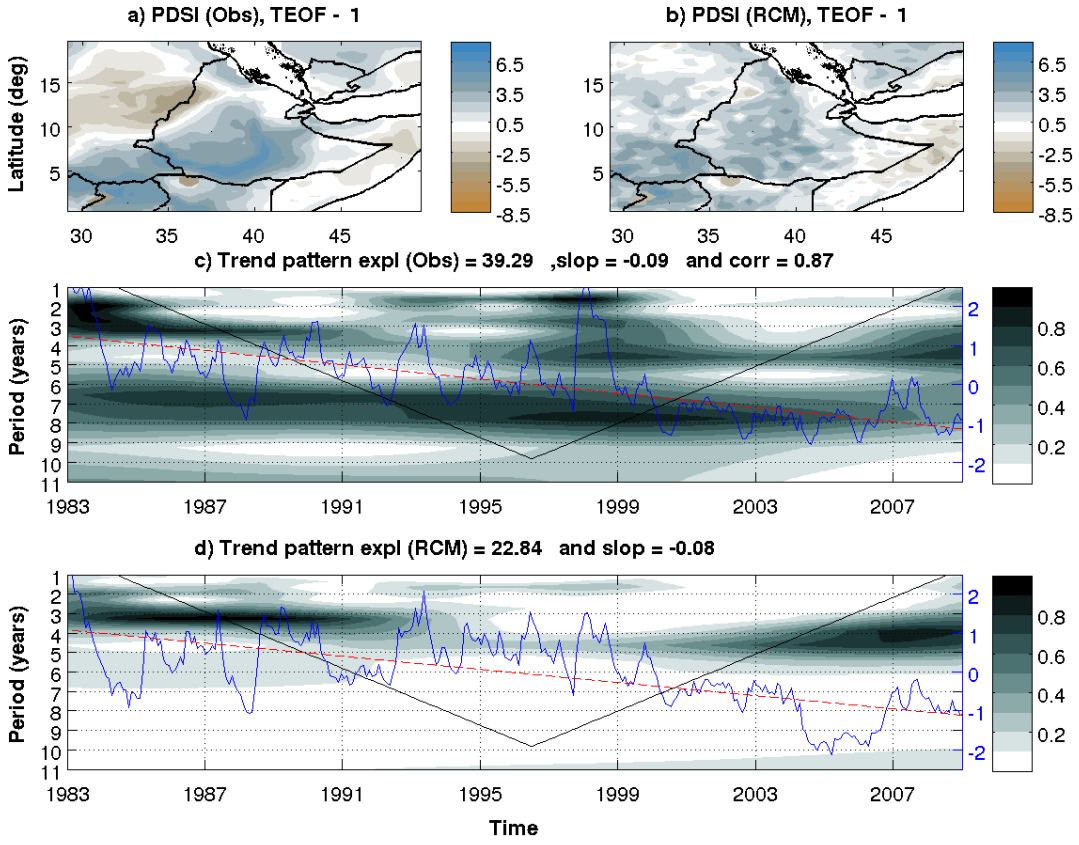

Fig. 5.2) The First dominant trend patterns of PDSI, a) TEOF-1 of PDSI driven from observation, b) TEOF-1 of PDSI driven from RegCM4, c) TPC-1 of PDSI (observation, blue solid line) with trend (red broken line which is linear fit of TPC-1) and wavelet analysis, d) TPC-1 of PDSI (driven from RegCM4, blue solid line) with trend (red broken line which is linear fit of TPC-1) and wavelet analysis.

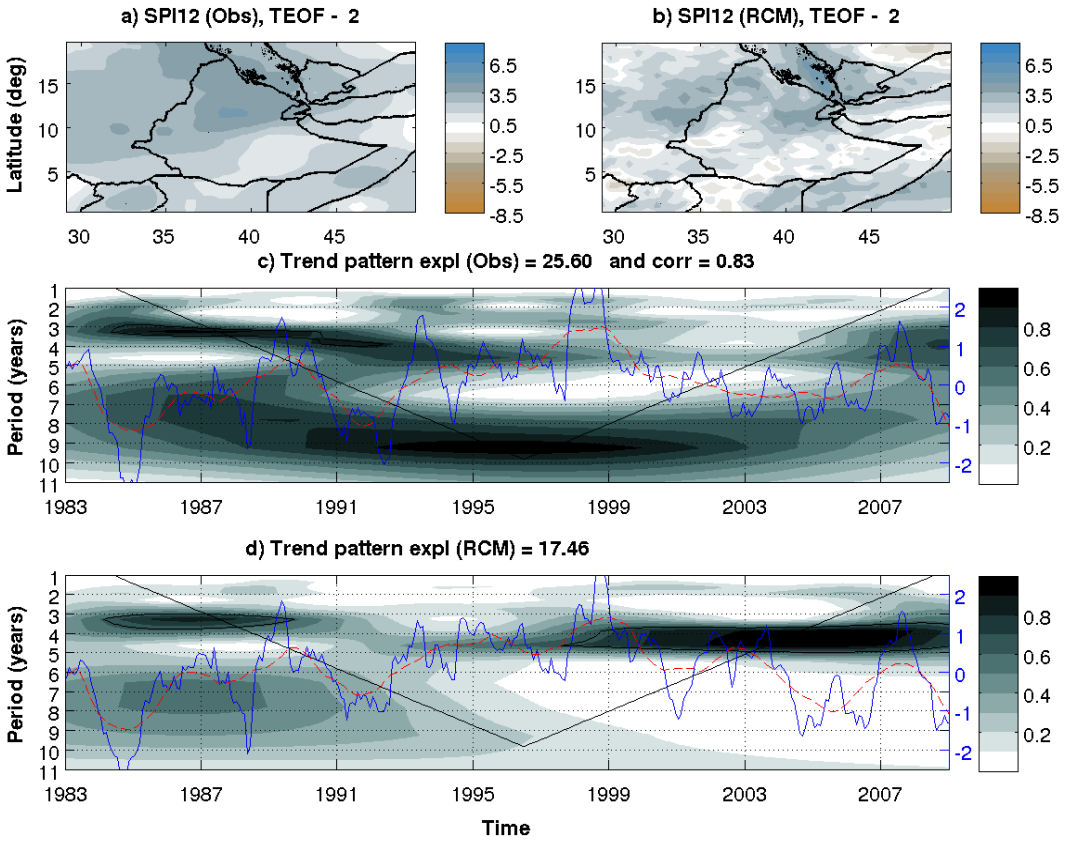

Fig. 5.3) The second dominant trend patterns of SPI12, a) TEOF-2 of SPI12 driven from observation, b) TEOF-2 of SPI12 driven from RegCM4, c) TPC-2 of SPI12 (observation, blue solid line) with 12 month moving average of TPC-2 (red broken line) and wavelet analysis, d) TPC-2 of SPI12 (driven from RegCM4, blue solid line) with 12 month moving average of TPC-2 (red broken line) and wavelet analysis.

The second dominant TEOF-2 patterns (Fig. 5.3a, b) of both observational and RegCM4 driven SPI12 describes mainly the northern regions and their TPC-2 (Fig. 5.3c, d) exhibit low frequency high power variability. The time series of these TPC-2 seem to dominated by dry events during the first decade until ~1997. Both observational and model driven TPC-2 show during ~1984/85, ~1988, ~1991/92, and ~ 2009 severe dry and during ~1989/90, ~1993/94, ~1998 and ~2007 wet events are occurred. The wavelet analysis of both observation and model driven TPC-2 indicates, during the first decade a combination of relatively high frequency (~1-4 years) and relatively low frequency (~8-9 years) high power signals. For the last decades, however, the high power signal is getting weaker in observations although the model derived

SPI12 shows a strong 3-4 years high power peak. Similar results are found in both observation and model driven PDSI second dominant TPCs (Fig. 5.4).

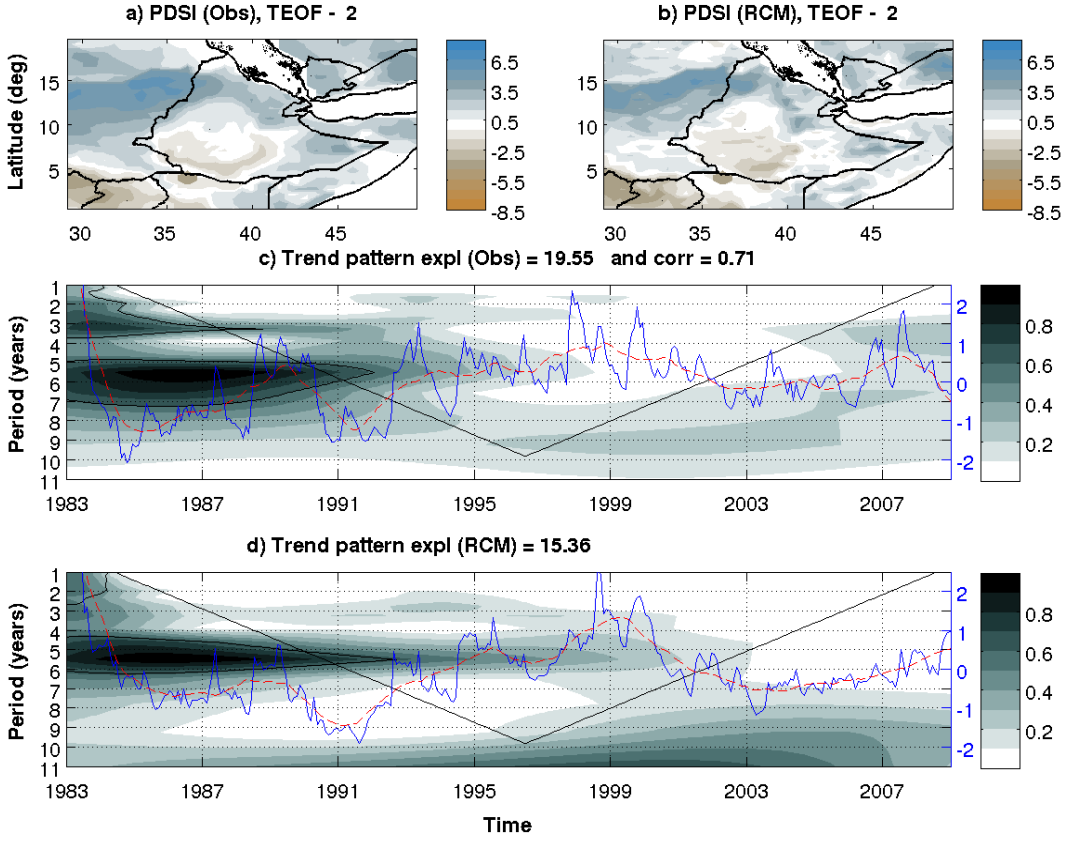

Fig. 5.4) The second dominant trend patterns of PDSI, a) TEOF-2 of PDSI driven from observation, b) TEOF-2 of PDSI driven from RegCM4, c) TPC-2 of PDSI (observation, blue solid line) with 12 month moving average of TPC-2 (red broken line) and wavelet analysis, d) TPC-2 of PDSI (driven from RegCM4, blue solid line) with 12 month moving average of TPC-2 (red broken line) and wavelet analysis.

This suggests that, unlike the southern region, the drought over this region shows just a low frequency variability with more drought in the 1980's and a recovering in the late 1990's.

The high correlations of observational and RegCM4 driven indices of PDSI and SPI12 second dominant TPCs (0.83 and 0.71 respectively) with similarity corresponding patterns (TEOFs-2) show the performance of the model to reproduce the features of drought events over Ethiopia. That is multi-scale temporal variability of drought using PDSI and SPI12 are simulated very well by RegCM4 with respect to observational driven indices.

In addition, the number of percentile severely/extremely dry months (P = number of extreme dry months/total months)*100) using observational (Fig. 5.5) and model (not shown here) driven PDSI < -2.99 and SPI12 < -1.49 confirms that the frequencies of dry years for the whole period are lower for northern regions than for the southern regions.

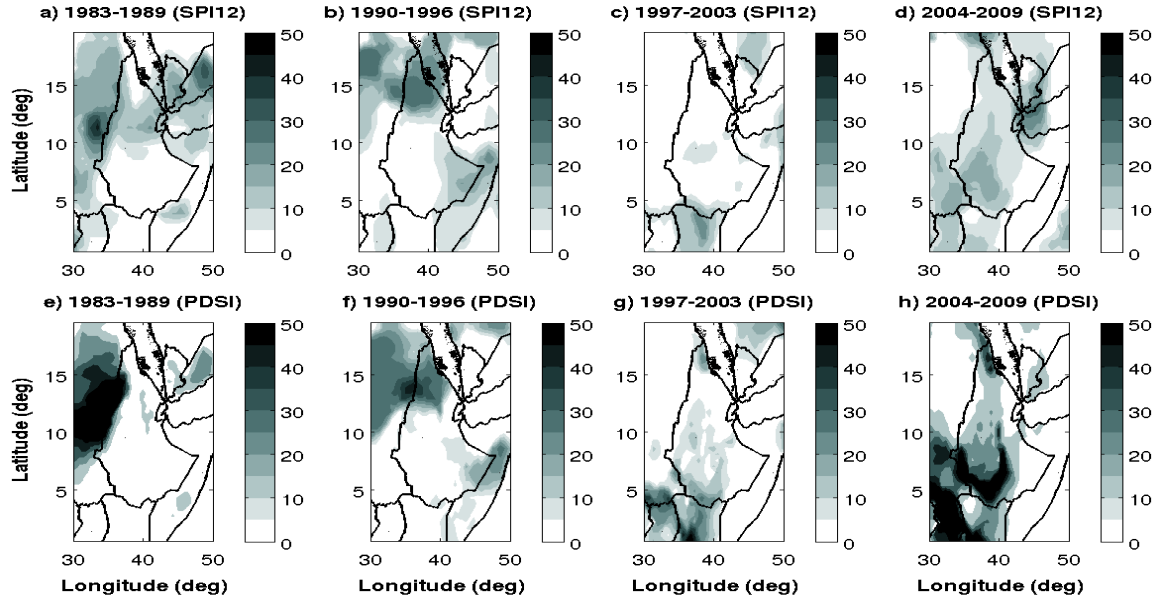

Fig. 5.5) Percentile of extreme-dry monthes; which is number of extreme-dry months of the sub-period per total number of months of the sub-period times 100; using SPI12 and PDSI monthly mean indices; driven from observational dataset.

This gives a clear picture for the frequency of severe drought occurrence in different regions of Ethiopia during four consecutive heptads; which is consistent with wavelet analysis. It indicates sever and extreme severe drought are observed more frequently over the northern and northeastern regions during the first two consecutive heptads. Then gradually the southern and southwestern regions experienced sever and extreme drought during the recent heptads as shown in Fig. 5.5a, b, c, d using SPI12 and Fig. 5.5e, f , g, h using PDSI. Overall, a good agreement is observed among all results of drought indices by both observational and model driven SPI12 and PDSI.

5.2. Inter-seasonal Variability of Drought

To understand seasonal contribution of the observed characteristics of drought we analyze TEOF of SPI3 for summer (JJAS) and spring (FMA) season; which are major rainy seasons for northern and southern regions respectively (see section 3.5). PDSI and SPI12 of any given month are strongly controlled by moisture conditions in the previous months, so as expected we found seasonal persistence in the southern regions. Therefore linking the inter-seasonal variability of PDSI and SPI12 patterns with intra-seasonal synoptic controls of climate is difficult. Short scale drought indices like Standardized Precipitation Index computed on 3-month time scale (SPI3) showed a considerable amount of inter-seasonal variability in terms of the size, shape and alignment of drought regions.

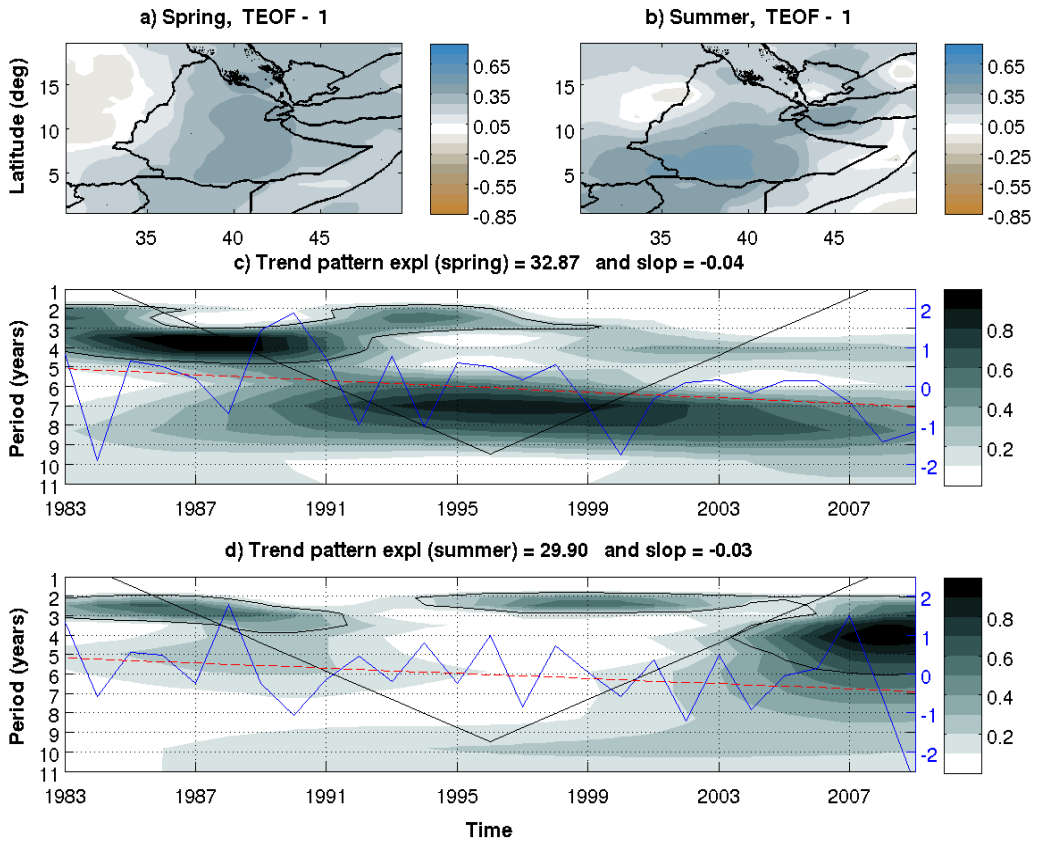

Fig. 5.6) The First dominant trend patterns of SPI3 driven from observation, a) Spring season TEOF-1 b) Summer season TEOF-1 c) spring season TPC-1 (blue solid line) with trend (red broken line which is linear fit of TPC-1) and wavelet analysis, d) summer season TPC-1 (blue solid line) with trend (red broken line which is linear fit of TPC-1) and wavelet analysis.

Moreover greatly related to the timing of extreme seasonal rainfall years over Ethiopia (for instance, the correlation between TPCs computed from SPI3 and observational rainfall the first two TPCs during spring are 0.93, 0.87 and during summer 0.91, 0.92 respectively).

The first dominant spring season TPC of SPI3; which explains the southern and eastern half of the country (Fig. 5.6a, c), indicates significant dry trend (decreasing rate = -0.038 observation and -0.033 model TPCs of SPI3 per year) and is dominated by relatively low frequency signals (6-8years) during ~1995-1999 and high frequency (3-4years) signals ~1988/89 years. The first dominant trend pattern of summer season represent the southern regions of the country, its time component (Fig. 5.6b, d) indicate the domination of high frequency signals during ~1987/88, ~1999/00 years. The southern region of Ethiopia has been experiencing below average spring rainfall for the past few decades and drought conditions since 1997.

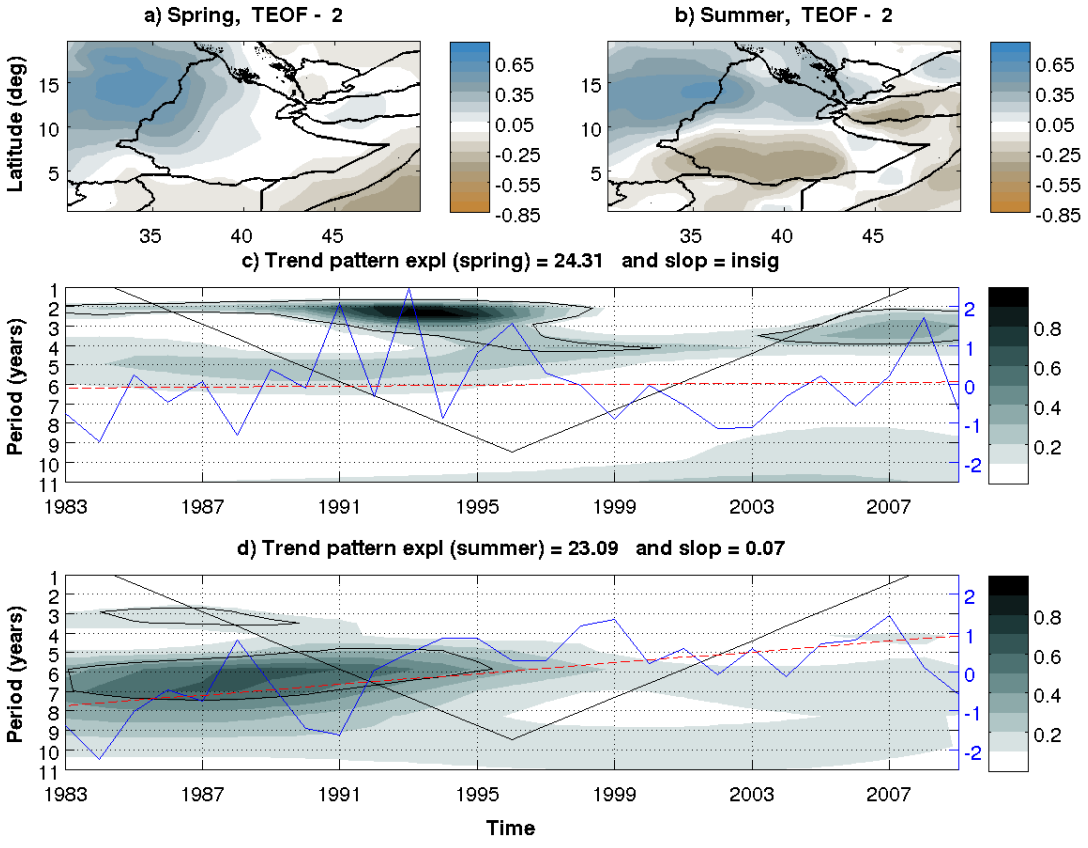

Fig. 5.7) The second dominant trend patterns of SPI3 driven from observation, a) Spring season TEOF-2 b) Summer season TEOF-2 c) spring season TPC-2 (blue solid line) with trend (red broken line which is linear fit of TPC-2) and wavelet analysis, d) summer season TPC-2 (blue solid line) with trend (red broken line which is linear fit of TPC-2) and wavelet analysis.

The second dominant TPC of SPI3 for the spring season explains the western regions (Fig. 5.7a, c, above "Gambela") and shows a high frequency (2-3years) signals before 1995. Whereas for the summer season, the second dominant TPC describes the northern regions (Fig. 5.7b, d) which indicates significant wet trend (0.069 SPI3 per year). TPC-2 of summer season shows dry anomalies in the first decade and wet anomalies in the recent decades. In addition, TPC-2 indicates low frequency high power signals domination during ~1987-1991 but not certain (out of cone of influence). Overall we understand extreme drought years are coinciding with common dry anomaly years of the two seasons (example; 1984, 2000 2008 and 2009 common extreme drought years of both season from first TPCs and 1983, 1984, 2009 from second TPCs) and consecutive dryness of these seasons (example: 2008/09 consecutive dry years during both season from first TPCs and 1984/85 from second TPCs). The common dry anomaly years of the first two dominant TPCs of spring and summer season indicate the coverage of drought occurrence (example: 1984, 1988, 1994, 2009 common dry years of both TPCs of spring and 1984, 1990 and 2009 are common dry years of summer dominant TPCs).

Spring and summer season number of percentile severely/extremely dry months of the season (P = number of extreme dry months of the season/total months the season)*100) using observational (Fig. 5.8 and Fig. 5.9) and model (not shown here) driven PDSI < -2.99 and SPI12 < -1.49 are analyzed. It indicates in the first heptanes (1983-1989, Fig. 5.8a, e and Fig. 5.9a, e) more severe droughts are occurred in the northern regions of Ethiopia during spring season than summer. During the second heptanes (1990-1996, Fig. 5.8b, f and Fig. 5.9b, f) comparative number of severe droughts are observed in the north-central regions of the country. Compare to the previous heptanes the third one (1997-2003, Fig. 5.8c, g and Fig. 5.9c, g) is little number of severe droughts appeared in both seasons. During the last years (2004-2009, Fig. 5.8d, h and Fig. 5.9d, h) more severe droughts are observed in southern regions of Ethiopia during summer than spring. This result also agrees with the above; which says southern and southwestern regions became sever and extreme drought regions in recent years.

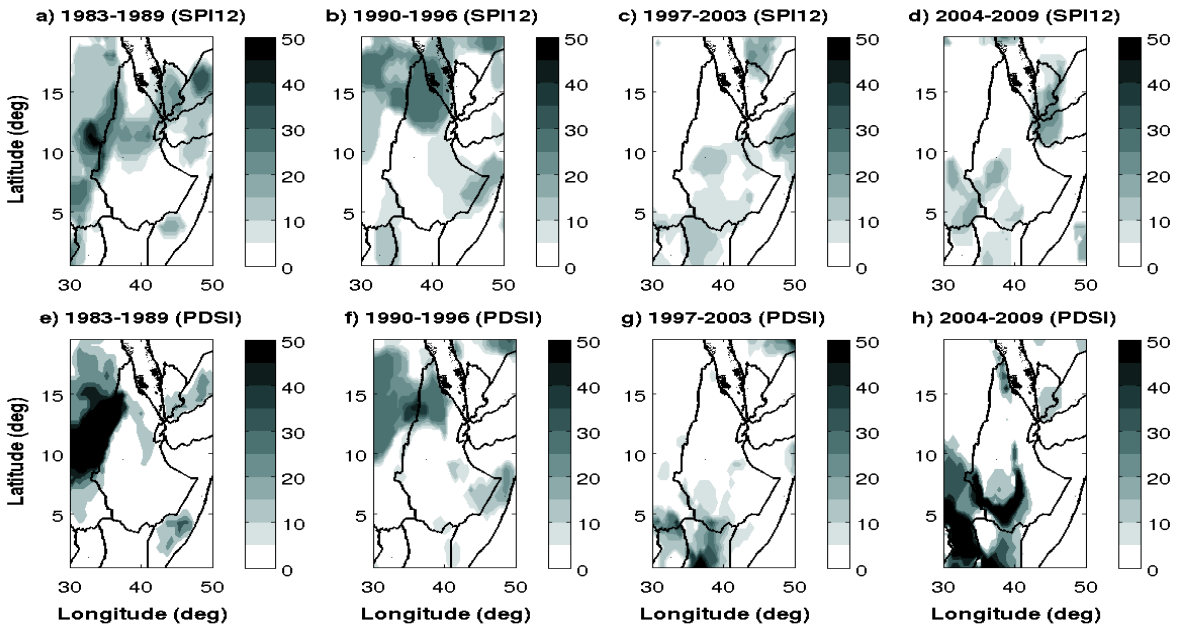

Fig. 5.8) Percentile of extreme-dry monthes; which is number of extreme-dry months of the sub-period per total number of months of the sub-period times 100; using spring months (FMA) SPI12 and PDSI monthly mean indices; driven from observational dataset.

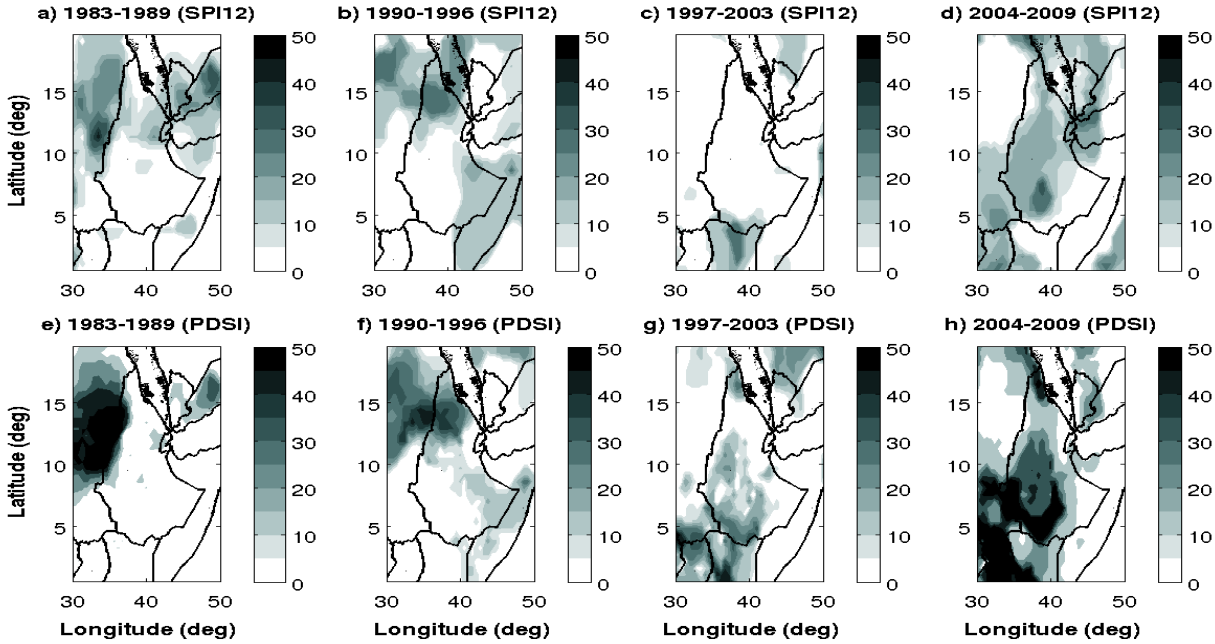

Fig. 5.9) Percentile of extreme-dry monthes; which is number of extreme-dry months of the sub-period per total number of months of the sub-period times 100; using summer season months (JJAS) SPI12 and PDSI monthly mean indices; driven from observational dataset.

5.3. Summary and Conclusion

Standardize Precipitation Index (SPI) and Palmer Drought Severity Index (PDSI) driven by observational and RegCM4 are used for expressing the severity of dry and wet conditions over Ethiopia. Using different approaches, this study investigated the spatial and temporal variations including trend of dry conditions over Ethiopian region during a period of 1982 - 2009.

The first dominant TEOF-1; which explains mainly the southern regions shows high magnitude positive pattern over southern regions and small magnitude negative pattern over northwestern regions. Its time component TPC-1 describes as more drought-prone regions of Ethiopia and statistically significant dry trend with high/low frequency high power signals in particular during the recent decade. In contrast, the second TEOF-2; which explains mainly northern regions indicates the likelihood of drought occurrence over these regions are considerably less and dominated by low frequency high power signals.

The high correlations of observational and RegCM4 driven indices of PDSI and SPI12 first dominant TPCs (0.86 and 0.87 respectively) and second dominant TPCs (0.83 and 0.71 respectively) with similarity corresponding patterns (TEOFs) shows the performance of the model to reproduce the features of drought events over Ethiopia. That is multi-scale temporal and spatial variability of drought over the southern and northern regions using PDSI and SPI12 are simulated very well by RegCM4 with respect to observational driven indices.

As alternative the number of percentile severely and extremely dry months (P = number of extreme dry months/total months)*100) using observational and RegCM4 driven PDSI < -2.99 and SPI12 < -1.49 are analyzed. It confirms that the frequencies of dry years for the whole period are lower over northern regions than the southern regions, when estimated by both observational and RegCM4 driven indices, especially during recent two heptads.

Spring season first dominant TEOF-1 explains the eastern half of the country; which its TPC-1 shows that significant dry trend and dominated by high/low frequency high power signals during ~1987/88 and ~1995 – 1999. The second TPC-2 of this season; which its pattern indicated the western regions, is dominated by high frequency signals during ~1992-1995 without

significant trend. On contrast, summer season first dominant TPC-1; which its pattern explains southern regions is dominated by high frequency signals without significant trend whereas, the TPC-2 of this season; which its pattern explains the northern regions, shows significant wet trend with relatively low frequency signals during first decade.

CHAPTER – SIX

The Physical Mechanisms of Drought Events over Ethiopia

So far, we understand the spatial and temporal multi-scale variability of rainfall, temperature and drought events in Ethiopia region. In addition, we have some idea about the intensity of drought events in different heptanes years in different regions of Ethiopia. So, at this point one of the questions may come to our mind; what are the causes of observed variability of drought events? What is the mechanism for the observed variability of drought intensity? What controls drought variability over Ethiopia on a seasonal time scale?

For this purpose, we examine variations of atmospheric variables including: - Low-level Horizontal Wind (zonal and meridional) averaged between 850-1000hpa (LHW), Upper-level Horizontal Wind; averaged between 100-300hpa (UHW), Sea Level Pressure (SLP), surface relative humidity and Sea Surface Temperature (SST) during dry/wet conditions of Ethiopia. Moreover, different ocean basins are selected (based on significant correlation between global SST and the first two dominant seasonal TPCs of drought indices; which is not shown here) for further analysis of REOF. These are East Equatorial Pacific; between longitude 180-80^{o}W and latitude 25^{o}S-30^{o}N (EEPc), Atlantic; between longitude 50^{o}W-15^{o}E and latitude 40^{o}S-60^{o}N (Atl) and Indian; between longitude 48-120^{o}E and latitude 40^{o}S-20^{o}N (Ind).

6.1. Large scale Circulation Features during Spring Season (February-April)

We correlate the first two dominant TPCs of spring SPI3 and global SSTA time series in each grid (Fig. 6.1) for a period 28 years (1982-2009). The significant correlation pattern of the first dominant TPC of SPI3 and global SSTA shows north equatorial central Pacific, west-central Indian and South Atlantic Ocean basins are associated positively, whereas sub-tropical central Pacific, equatorial west Pacific, north Atlantic and coast of Guinea are associated negatively

(Fig. 6.1a). The second dominant TPC of spring SPI3 correlated negatively with Indian, south-

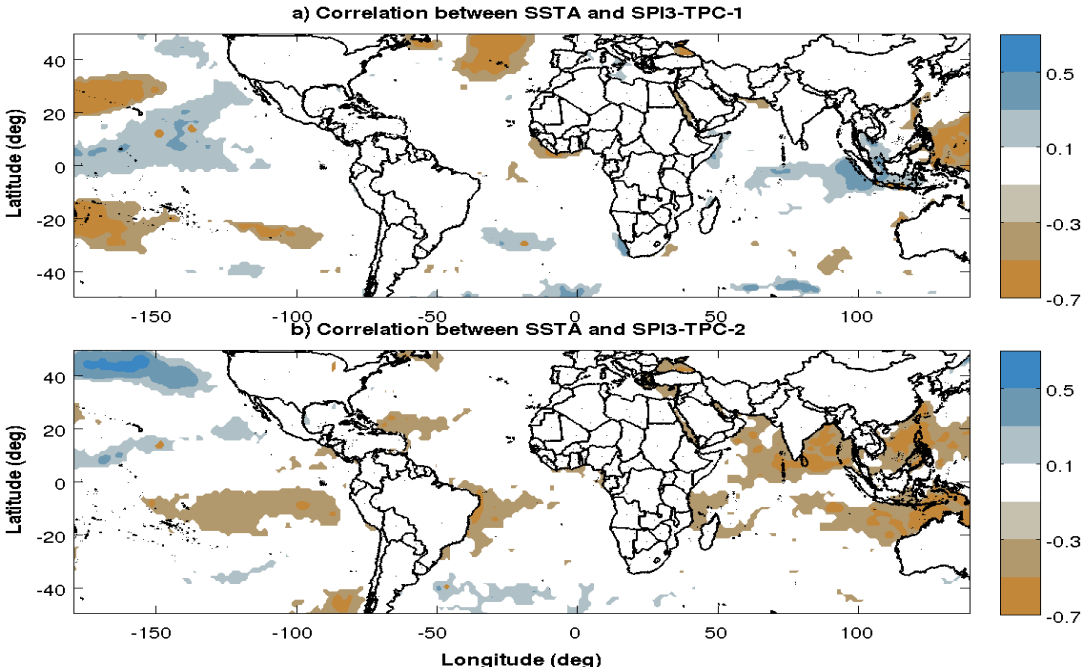

Fig. 6.1) Correlation between spring dominant TPCs of SPI3 with contemporary SSTA; a) with TPC-1 b) with TPC-2.

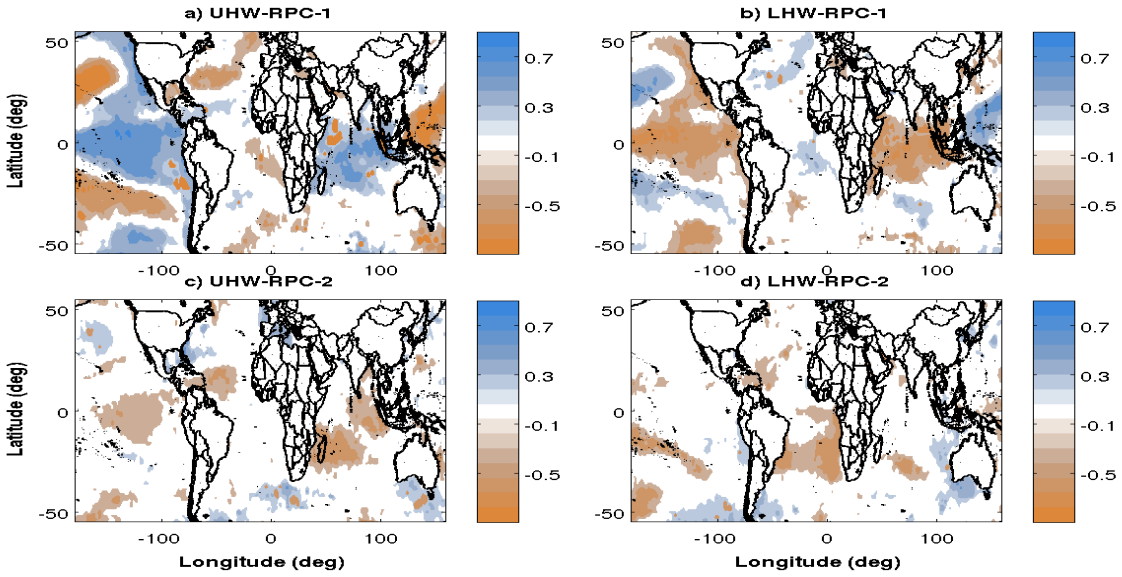

Fig. 6.2) Correlation between spring SSTA with contemporary dominant RPCs of horizontal Wind: a) upper-RPC-1; b) low-RPC-1 c) upper-RPC-2 d) low-RPC-2.

equatorial east Pacific and south-equatorial-west Atlantic Ocean basins (Fig. 6.1b). The significant linear association found in all oceanic basins with dominant TPCs during spring season agrees with the previous studies (Diro et al. 2011a). The correlation patterns between the first two dominant RPCs (Fig. 4.2 and 4.4) of low/upper-level horizontal wind with contemporary spring global SSTA consolidate the above result; which all ocean basins are significantly linked linearly with spring drought variability of Ethiopia (Fig. 6.2). Specifically both dominant RPCs of upper-level horizontal wind strongly correlated with Pacific Ocean, whereas RPC-1 and RPC-2 of low-level horizontal wind associated better with Atlantic and Indian Ocean basins than Pacific and the linear association of these variables are summarized in Table 6.1. The correlation patterns of spring oceanic indices with Ethiopian contemporary raw SPI3 confirm the significant association of these ocean basin and Ethiopian climate. For instance, areal average between 55-15W and 5-25N of Tropical North Atlantic (TNA), areal average between 30W-10E and 0-20S of Tropical South Atlantic (TSA) and the difference of West Indian areal average and East Indian areal average or Indian Ocean Dipole (IOD) are correlated negatively with raw SPI3 time series (Fig. 6.3b, c, d). On the other hand, areal average between 170-120W and 5W-5E SSTA region (Nina3pt4), the difference of sub-tropical west Indian areal average and sub-tropical east Indian areal average (SIOD) and 30hpa zonal wind at the equator, averaged from 0-60E (Quasi Biennial Oscillation, QBO) are correlated positively over Ethiopia (Fig. 6.3a, e, f).

Similar results are found from REOF analysis of the selected ocean basins (Fig. 6.4a, b, c and d). This can be demonstrated from the correlation pattern of the most significant correlated dominant modes of EEPc, Atlantic and Indian oceans with raw spring SPI3 over Ethiopia (Fig. 6.4e, f, g). The result indicates unevenly heating of east Pacific, Atlantic and Indian Ocean are significantly correlated with raw SPI3 time series in different regions of Ethiopia. For instance, the second dominant REOF of east Pacific shows positive anomaly over its equatorial part (Fig. 6.4a, d) and its time component (RPC-2) is positively correlated with spring raw SPI3 (Fig. 6.4e). The third dominant variability (RPC-3) of Atlantic; whose pattern indicates positive pattern over coast of Guinea and northwest Africa is correlated negatively with raw SPI3 over most of spring rain getting regions (Fig. 6.4f).

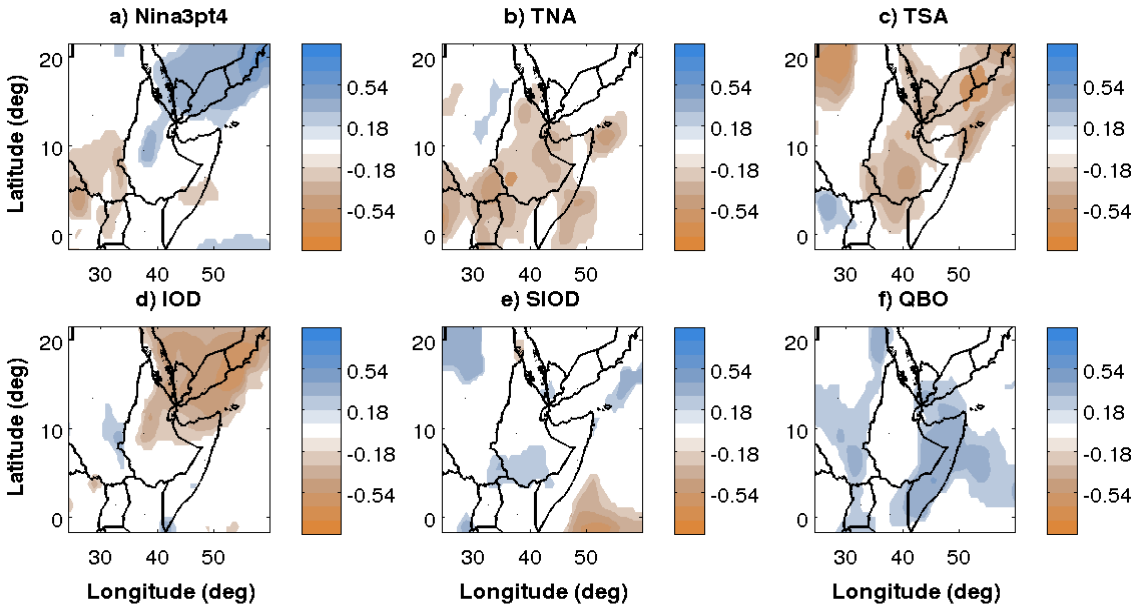

Fig. 6.3) Correlation patterns of raw spring SPI3 and contemporary indices of Oceanic basins; a) areal average of Nina1pt2, b) areal average of Nina3pt4, c) South oscillation index, d) areal average of tropical north Atlantic, e) areal average of tropical south Atlantic, f) North Atlantic Oscillation, g) the difference of west Indian areal average and east Indian areal average, h) the difference of south west Indian areal average and south east Indian areal average, i) 30hpa zonal wind at the equator, averaged from 0-60E.

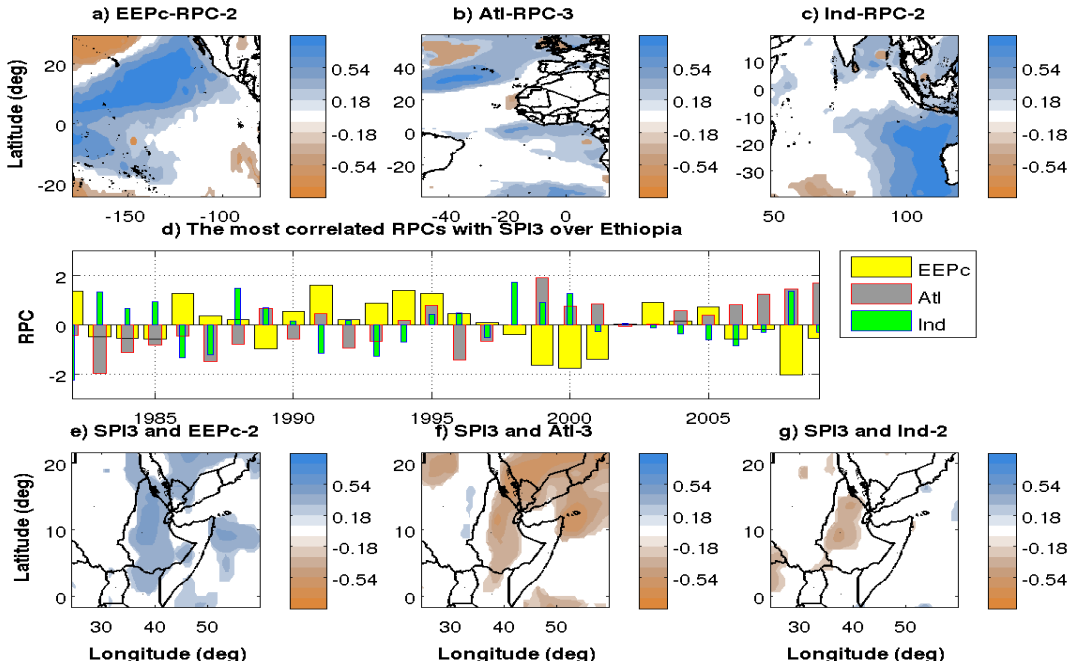

Fig. 6.4) Correlation of RPCs with SSTA and SPI3 of; a) SSTA and RPC-2 of East Pacific (longitude 180-80W, latitude 20S-20N), b) SSTA and RPC-3 of Atlantic (longitude 50W-15E, latitude 40S-60N), c) SSTA and RPC-2 of Indian ocean basin (longitude 48-120E, latitude 40S-20N), d) The corresponding RPCs, e) SPI3 with RPC-2, f) SPI3 with RPC-3 and g) SPI3 with RPC-2.

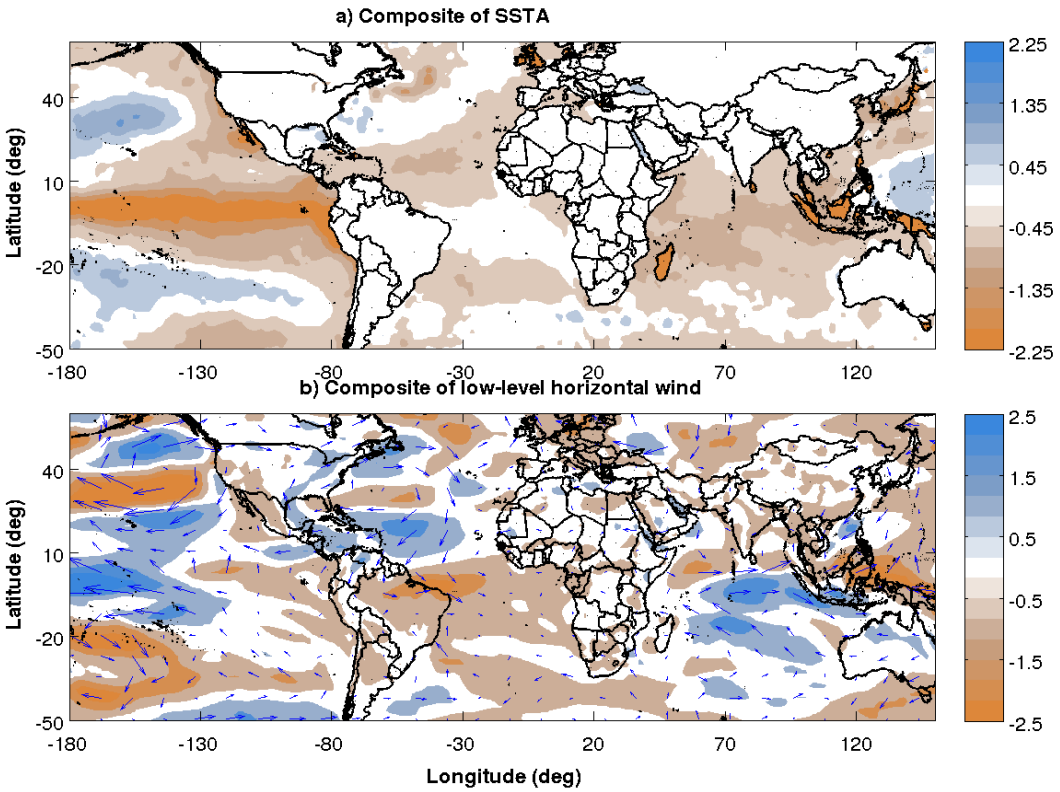

Fig. 6.5) Composite (dry minus wet anomaly years) patterns during spring season, based on spring dominant TPC-1 of SPI3; a) SST, b) Low-level horizontal wind.

Similarly, the second dominant mode of Indian Ocean (RPC-2), whose pattern shows negative IOD, is correlated negatively over north central regions of Ethiopia (Fig. 6.4g). Therefore, all ocean basins are significantly associated with climate of Ethiopia, which is in agreement with the above discussions.

Four dry (1984, 2000, and 2008 and 1994/1992) and wet (1990, 1989, 1991/1993 and 1983) years are chosen from the first dominant TPCs of spring SPI3 using student's t-test to understand the dynamics in spring season. Figure 6.5a indicates the dry minus wet composite of Sea Surface Temperature Anomaly (SSTA) based on TPC-1 of spring SPI3. It reveals highest negative anomalies over east Pacific; which affect the rain producing mechanisms in Ethiopia, the negative anomaly over the West Indian; which affects the low-level circulation, are events happened contemporary with drought over most of southern and southeastern regions of Ethiopia.

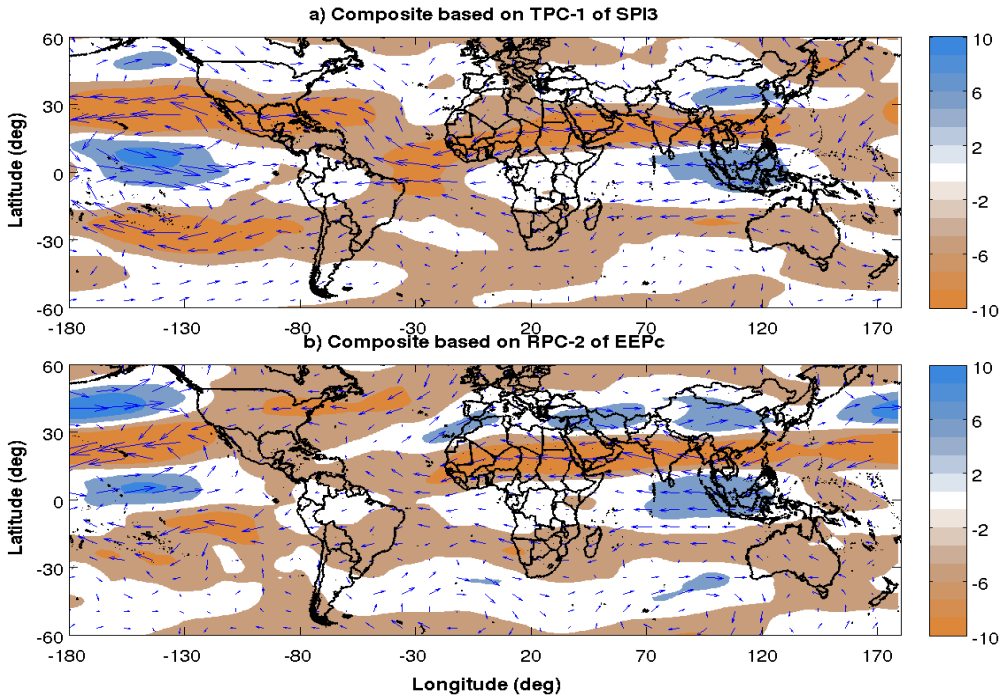

Fig. 6.6) Composite of upper-level horizontal wind during spring season: a) dry minus wet anomaly patterns, based on spring dominant TPC of SPI3; b) cool minus warm anomaly patterns, based on second dominant RPC of EEPc.

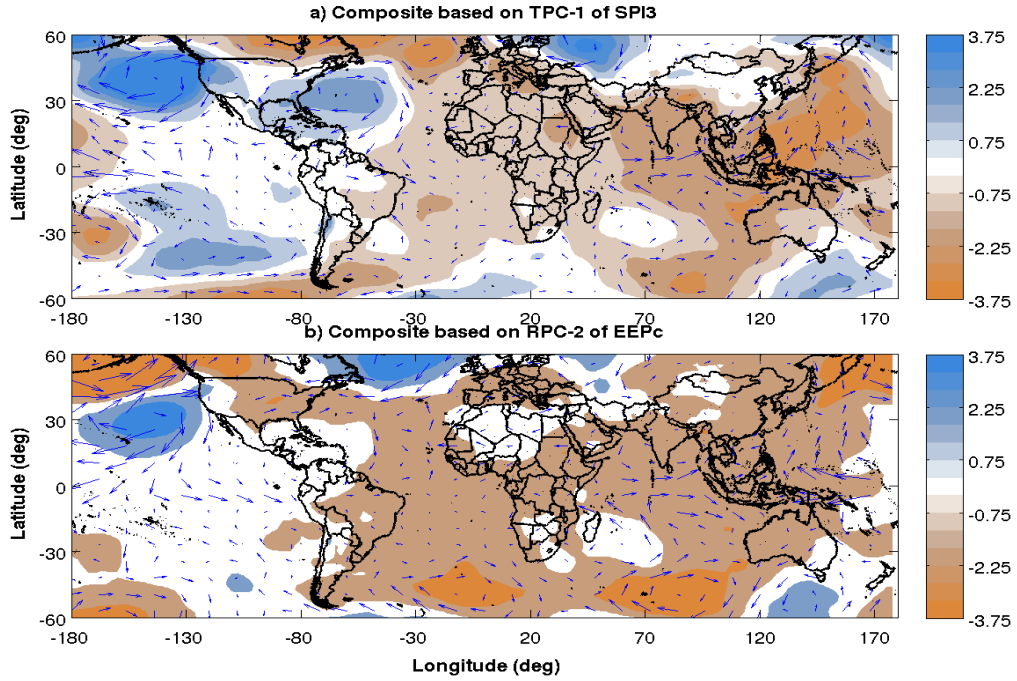

Fig. 6.7) Composite of sea level pressure during spring season: a) dry minus wet anomaly patterns, based on spring dominant TPC of SPI3; b) cool minus warm anomaly patterns, based on second dominant RPC of EEPc.

From spring climatology of low-level horizontal, wind (not shown here) we understand southwesterly and northwesterly from Atlantic, northerlies from Mediterranean and south easterlies, easterlies and north easterlies from Indian Ocean are low-level winds, which carry moisture towards Ethiopian regions. The variability of one of these systems is significantly affecting the corresponding region of the country. For instance, over Indian and Gulf of Guinea the low-level horizontal wind decreases in magnitude because of westerly anomalies over cost of Somalia and easterly anomalies over west of Ethiopia; which make the region an area of divergence (Fig. 6.5b). This condition is strongly associated with deficiency of rainfall and cause drought over most of spring rain getting regions of Ethiopia. In normal condition the low-level horizontal wind coming from northeast, southwest and southeast come together and converge; which characterized by strong upward motion and precipitation (Segele et al. 2009a and Diro et al, 2011a, 2011b). And around east Africa the Inter Tropical Convergence Zone (ITCZ) have meridional component due to the difference in heat capacity of the land surface and the Indian Ocean (Diro 2008 and references therein). Sometime this convergence zone around tropics (ITCZ) changes its position and strength depending on the strength of the low-level horizontal winds coming towards the region. These moisture carrying systems by turn depends on sub-tropical high-pressure systems (namely North Atlantic (Azores), South Atlantic (St. Helena), South India (Mascarene) and North India (Arabian) Azores) and global SSTA. From our composite result, of low-level horizontal wind (Fig. 6.5b) we noticed shift of the meridional component of ITCZ towards west; which is associated with weakening of southwesterlies; coming from south Atlantic and strength of northeasterly anomaly during negative anomaly years of SPI3 in spring season. The westward/eastward shift of meriodinal component of ITCZ associated with dry conditions of eastern/western regions of the country during spring season.

From composite patterns of upper-level horizontal wind, we noticed decreasing of STWJ in magnitude over north half of Ethiopia suggesting northward shift of STWJ from its climatological location or strength of easterly anomalies (Fig. 6.6a). The weak/strong STWJ is strongly associated with dry/wet conditions of spring rain getting regions of the country by weakening/enhancing the ascent flow and convection. Similar composite analysis of upper-level horizontal wind based on cool minus warm EEPc basin (Fig. 6.6b) shows , during negative anomaly years of EEPc the upper-level horizontal wind (STWJ) decreases because of the strengthening of mixed Rossby-Gravity wave (easterlies).

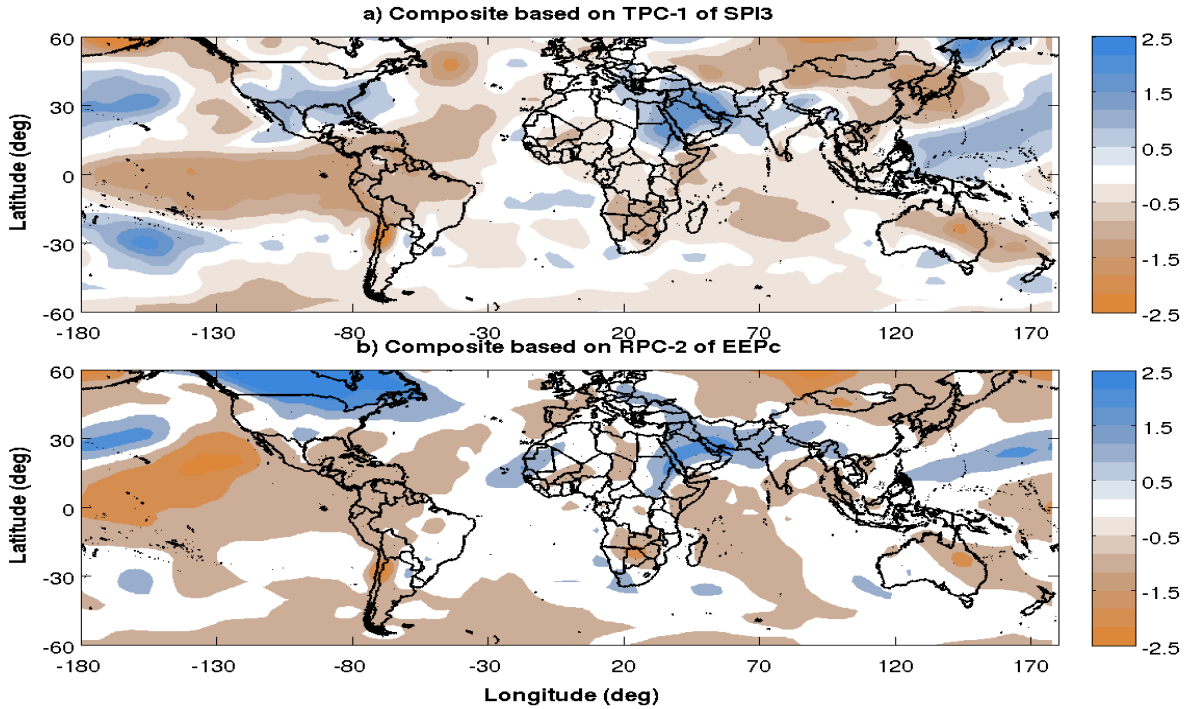

Fig. 6.8) Composite of surface air temperature during spring season: a) dry minus wet anomaly patterns, based on spring dominant TPC of SPI3; b) cool minus warm anomaly patterns, based on second dominant RPC of EEPc.

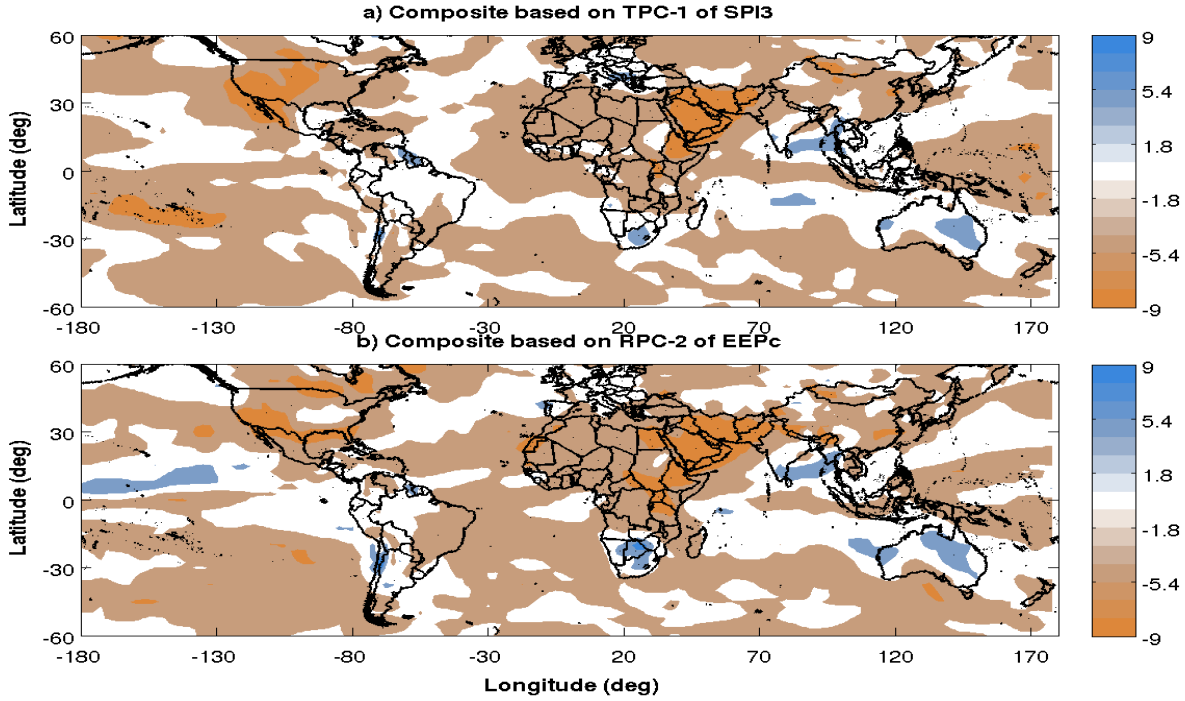

Fig. 6.9) Composite of surface relative humidity during spring season: a) dry minus wet anomaly patterns, based on spring dominant TPC of SPI3; b) cool minus warm anomaly patterns, based on second dominant RPC of EEPc.

A separate study by Maruyama and Tsuneoka (1988), Shaman and Tziperman (2011) and Plumb (1977) in connection with linkage between ENSO and QBO has shown existence of such relationship via Rossby wave. Hence, our result confirms the effect of ENSO on Ethiopian climate during spring season via altering large-scale circulation through Kelvin/mixed Rossby-Gravity waves. The negative anomaly of the Arabian High and positive anomaly over Azores; which facilitate westerly anomaly over equatorial Indian Ocean are related to drought over Ethiopia (Fig. 6.7a, b) by suppressing the moisture influx from Indian Ocean and the easterlies south of Arabian high. Diro (2008) reported similar results. In addition, the composite patterns of surface air temperature (Fig. 6.8) and surface relative humidity (Fig. 6.9) consolidate the above discussion. The decreasing temperature mostly associated with increasing pressure except some places and discussed in detailed by Copsey et al. (2006); which supplement the above discussion.

Occasionally dry events are observed during positive anomaly years of EEPc (e.g. 1992, Fig. 6.10a). Although, ENSO is dominant mode and interlinked with other ocean basins the variability of southeast/southwest Atlantic and weak negative IOD patterns play important role for the occurrence of drought by varying the low-level dynamics (Fig. 6.10b). We already noticed that from above discussion the easterly anomaly observed over equatorial Atlantic is associated with dry events over Ethiopia (Fig. 6.10b).

Table 6.1) Correlation magnitude of dominant principal components of atmospheric variables.

Dominant modes		correlation	Dominant modes		correlation
SPI3-1,2	LHW-4,2	0.56,0.65	SPI3-1	EEPc-2	0.58
SPI3-1,2	UHW-1,2	0.67,0.52	In-2	LHW-1	0.49
SPI3-1	At-3	0.66	EEPc-2	UHW-1	0.73
SPI3-1	In-2	0.51	At-3	LHW-1	0.69

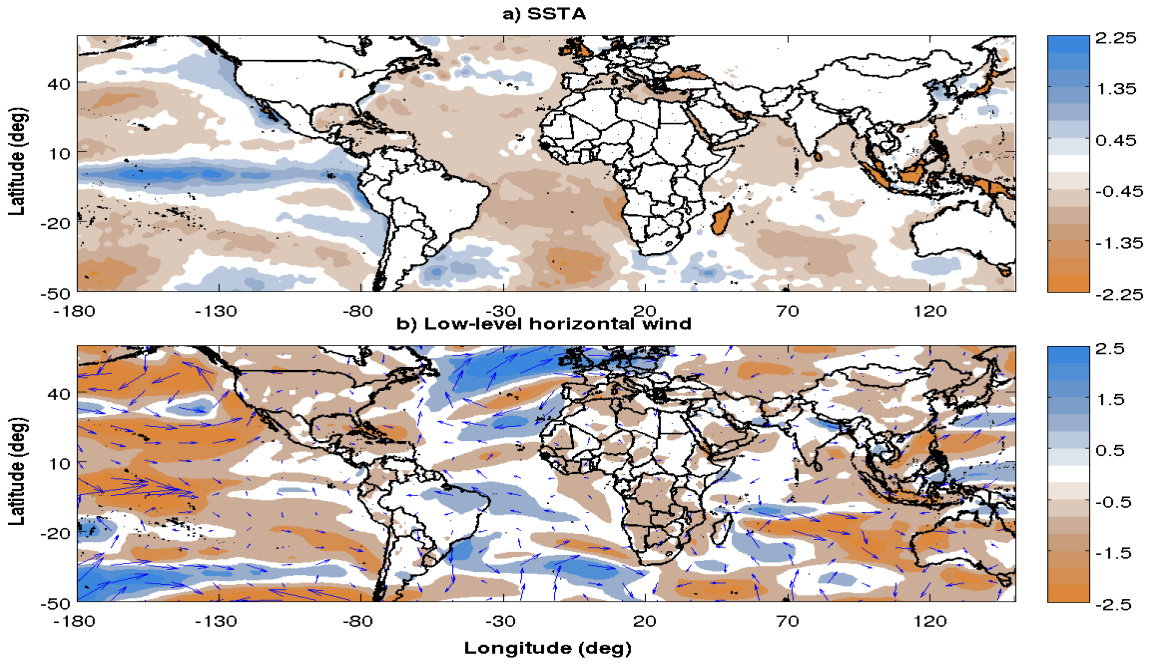

Fig. 6.10) Spring season anomaly patterns of during 1992 (example of dry year); a) SST, b) Low-level horizontal wind.

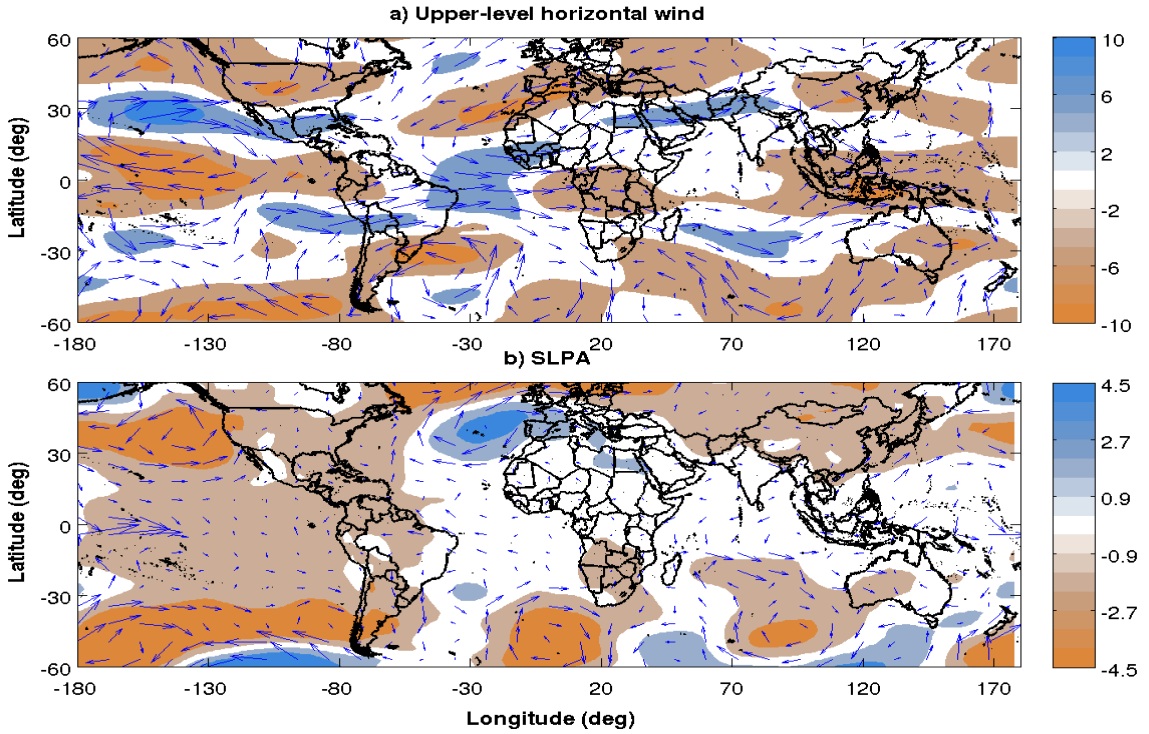

Fig. 6.11) Spring season anomaly patterns of during 1992 (example of dry year); a) Upper-level horizontal wind b) Sea level Pressure with low-level horizontal wind anomaly vector.

The weakening of moisture carrying systems from both neighboring ocean basins is highly associated with dry conditions even when the upper-horizontal wind is unchanged. But in 1992 southerly extension of STWJ slightly shifts towards west from climatological position (Fig. 6.11a); which may be because of the strength of Azores (Fig. 6.11b) and this in turn create favorable conditions for decreasing pressure over northwest Africa and Arabian high at higher altitudes.

6.1.1. Discussion in spring season large scale features

In this section, we found that spring anomaly of EEPc, Atlantic and Indian Ocean basins are significantly associated with contemporary drought indicators in Ethiopia. The correlation patterns of dominant RPCs of oceanic basins with raw SPI3 and with low/upper-level horizontal wind over Ethiopia shows significant association of these variables. Similar correlation patterns of spring oceanic indices with Ethiopian contemporary raw SPI3 confirm the significant association of these oceanic basins and Ethiopian climate. The correlation of EEPc with SPI3 and upper-level horizontal wind shows higher and significant, on the other hand the low-level horizontal wind correlated better with Atlantic and Indian Ocean basins than EEPc.

The composite analysis confirms the linkage of these variables. During extreme dry spring years of Ethiopia, negative anomaly of SSTA over EEPc, less magnitude negative anomaly of SSTA over Atlantic and Indian ocean basins, decreasing of low-level horizontal wind, decreasing of STWJ because of easterlies (Kelvin/mixed Rossby-Gravity wave), decreasing/increasing of high pressure systems and air temperature and decreasing of relative humidity are observed at the same time. We noticed some dry events in Ethiopia are observed during positive SSTA years of EEPc, high negative SSTA of southeast Atlantic, less negative SSTA of west Indian, decreasing low-level wind, shifting towards west the trough of STWJ and decreasing/increasing of high pressure systems. From this, we understand EEPc SST is the most dominant mechanism for the variability of Ethiopian climate via altering large-scale circulation. On the other hand, neighboring oceanic basins also play important role for the variation by altering mostly moisture carrying systems towards the country. For instance, increasing SST over the western/southwestern Indian Ocean warm pole results in increased evaporation and this moist

air is advected to high-land/southwest-border regions, which is strengthened by the low-pressure anomaly generated over these warm poles. In similar manner SSTA and the pressure, systems over Atlantic (e.g. the Azores High, the Icelandic Low) control the direction and strength of winds coming from this ocean basin into Ethiopia.

6.2. Large Scale Circulation Features during Summer Season (June-September)

Fig. 6.12a indicates the correlation pattern of summer SPI3 dominant TPC-1 and time series of global SST. It indicates the EEPc region is significantly correlated negatively; which is unlike to spring season and northeast Atlantic (coastal area of northwest Africa) correlated negatively. The correlation pattern (Fig. 6.12b) of summer second dominant TPC-2 of SPI3 with contemporary SSTA shows weak association with EEPc and positively correlated with northwestern Atlantic and central Indian Ocean. From this, we understand the northwestern and south tip regions of Ethiopia (region explained by corresponding TEOF-2) are associated more with Atlantic and Indian Ocean than east Pacific. Fig. 6.13 indicates the correlation patterns of summer upper/low-level horizontal wind dominant RPCs with contemporary global SSTA. Similar to spring season upper-level horizontal wind is strongly associated with ENSO region and low-level horizontal wind with neighboring ocean basins. The correlation results are summarized in Table 6.2. The correlation patterns of summer raw SPI3 with time series Nina3pt4, SIOD and QBO indicates negative association (Fig. 6.14a, e, f); which is opposite to spring season. On the other hand, the correlation of TNA, TSA and IOD with raw summer SPI3 shows positive/negative correlation over northwest/south regions (Fig. 6.14b, c, d). Similar results are reported (Segele et al. 2009a and Diro et al, 2011a, 2011b).

REOF analysis of oceanic basins confirms the above results. It indicate the warming of EEPc ocean basin, which its time component is negatively, correlated over north half of the country (Fig. 6.15a, d, e). The third pattern (REOF-3) of Atlantic; which explain the dipole pattern (negative south eastern and positive southwestern) of south equatorial Atlantic basin (Fig. 6.15b, d, f) and its time component shows mostly positive before 1997 and negative afterwards.

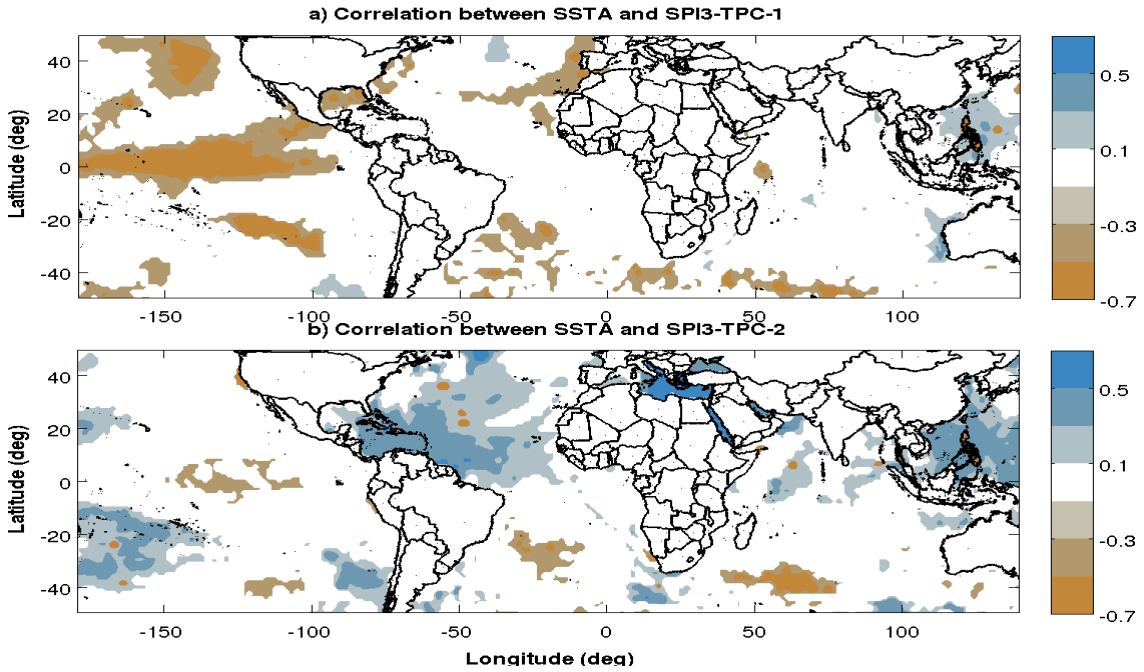

Fig. 6.12) Correlation summer SSTA with contemporary dominant TPCs of SPI3; a) with TPC-1 b) with TPC-2.

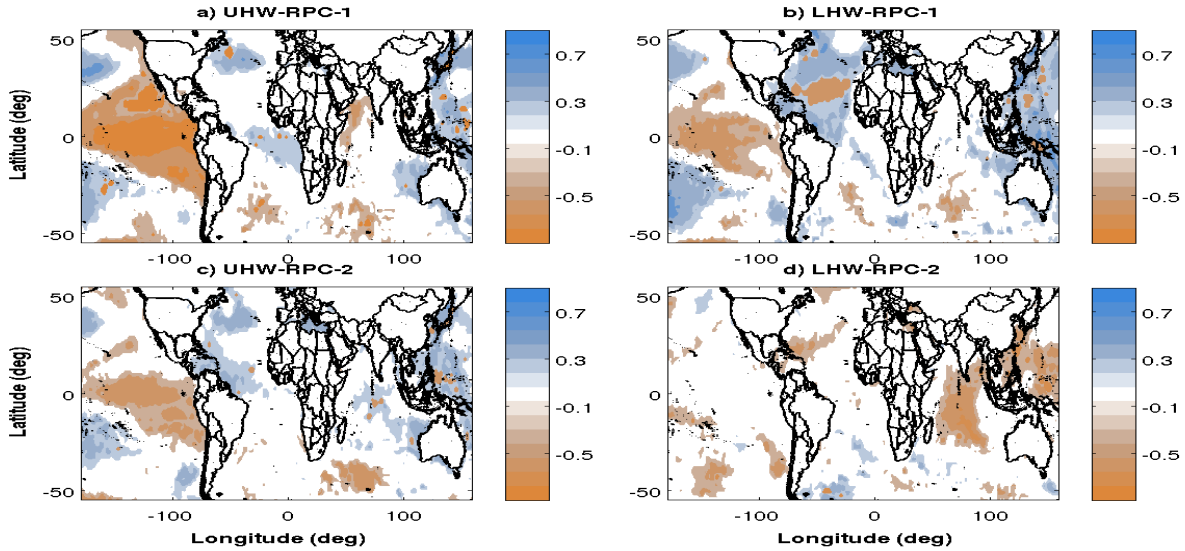

Fig. 6.13) Summer SSTA correlation with contemporary dominant RPCs of horizontal wind; a) upper-RPC-1 b) low-RPC-1 c) upper-RPC-2 d) low-RPC-2.

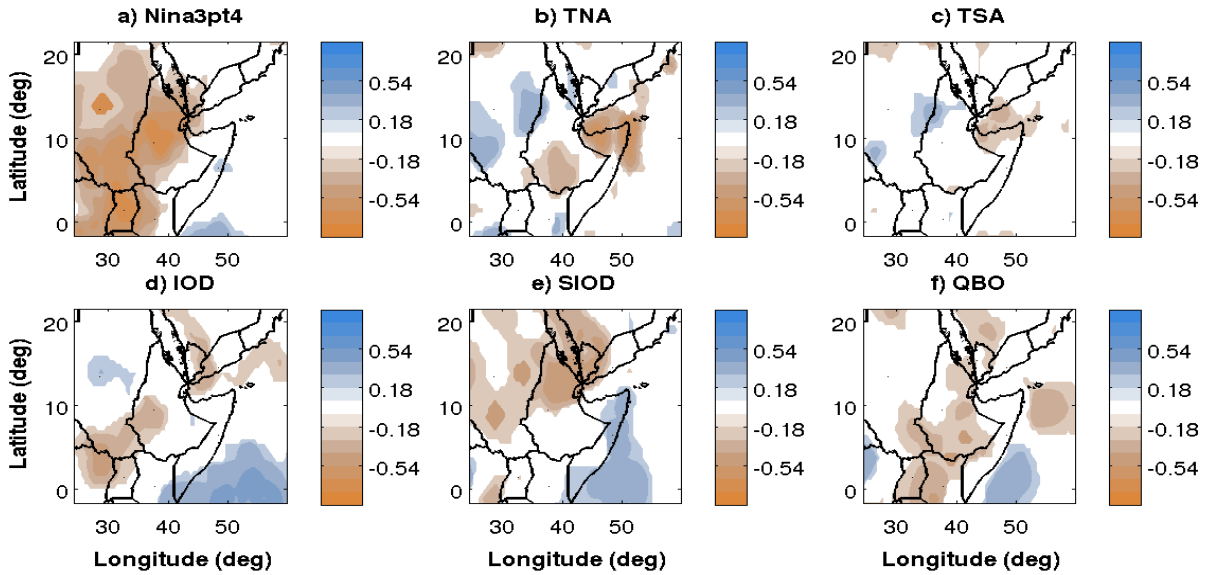

Fig. 6.14) Correlation patterns of raw summer SPI3 and contemporary indices of Oceanic basins; a) areal average of Nina1pt2, b) areal average of Nina3pt4, c) South oscillation index, d) areal average of tropical north Atlantic, e) areal average of tropical south Atlantic, f) North Atlantic Oscillation, g) the difference of west Indian areal average and east Indian areal average, h) the difference of south west Indian areal average and south east Indian areal average, i) 30hpa zonal wind at the equator, averaged from 0-60E.

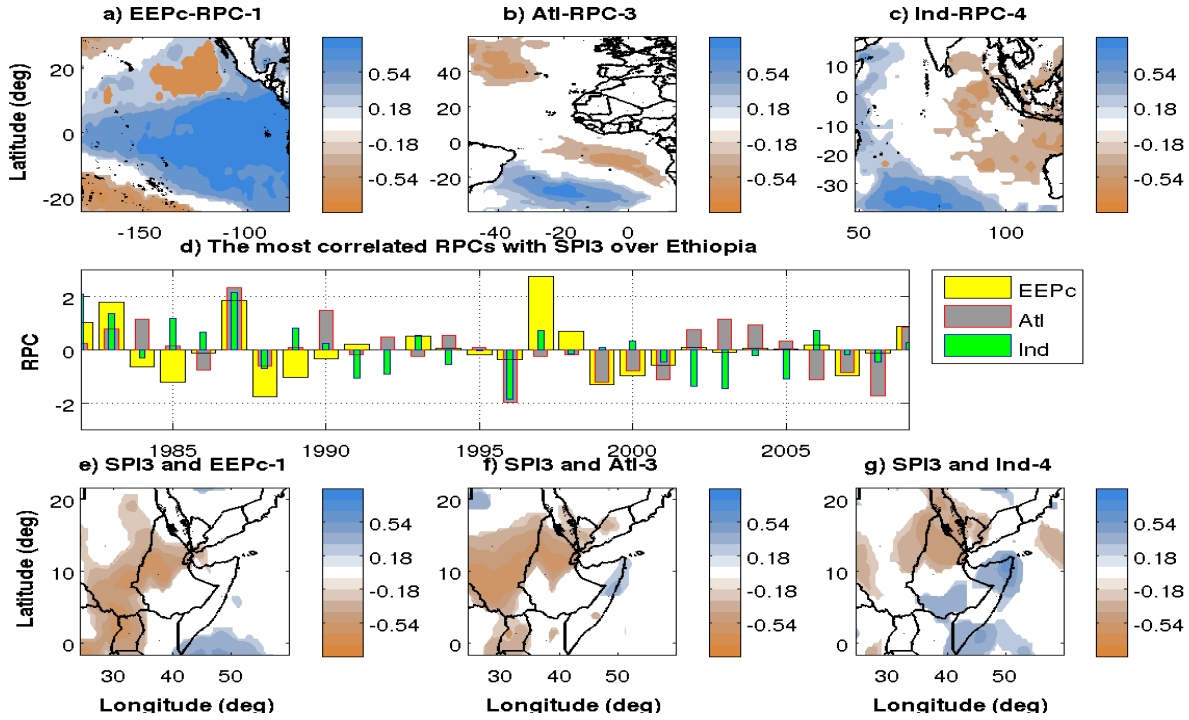

Fig. 6.15) The dominant variability patterns of Atlantic and Indian Oceans, corresponding RPCs and the correlation patterns of SPI3 and RPCs during summer season.

This RPC-3 of Atlantic is correlated negatively over northern half of the country like EEPc. The fourth dominant pattern of Indian Ocean basin shows weak positive IOD and its time component correlated positively and negatively over southern tip and northern regions of Ethiopia (Fig. 6.15c, d, g) respectively. The results confirm all three oceanic basins are highly associated with Ethiopian summer rain.

In order to understand dynamical relation of oceanic basins, large-scale circulation and Ethiopian climate we choose four wettest (1983, 1988, 1996/98, 2007) and four driest (1990/91, 1997, 2002, 2009) years using similar approach to spring season for composite analysis of atmospheric variables. Fig. 6.16a shows the composite of SSTA and low-level wind based on summer dominant TPC-1 of SPI3 and it indicates that drier conditions in southern Ethiopia are connected with warm SSTA over equatorial pacific and colder SSTA over Indian and Atlantic oceans. The result supplements the above discussion and agree with previous studies (Korecha and Barnston 2007; Segele and Lamb 2005; Segele et al. 2009a and Diro et al, 2011a, 2011b).

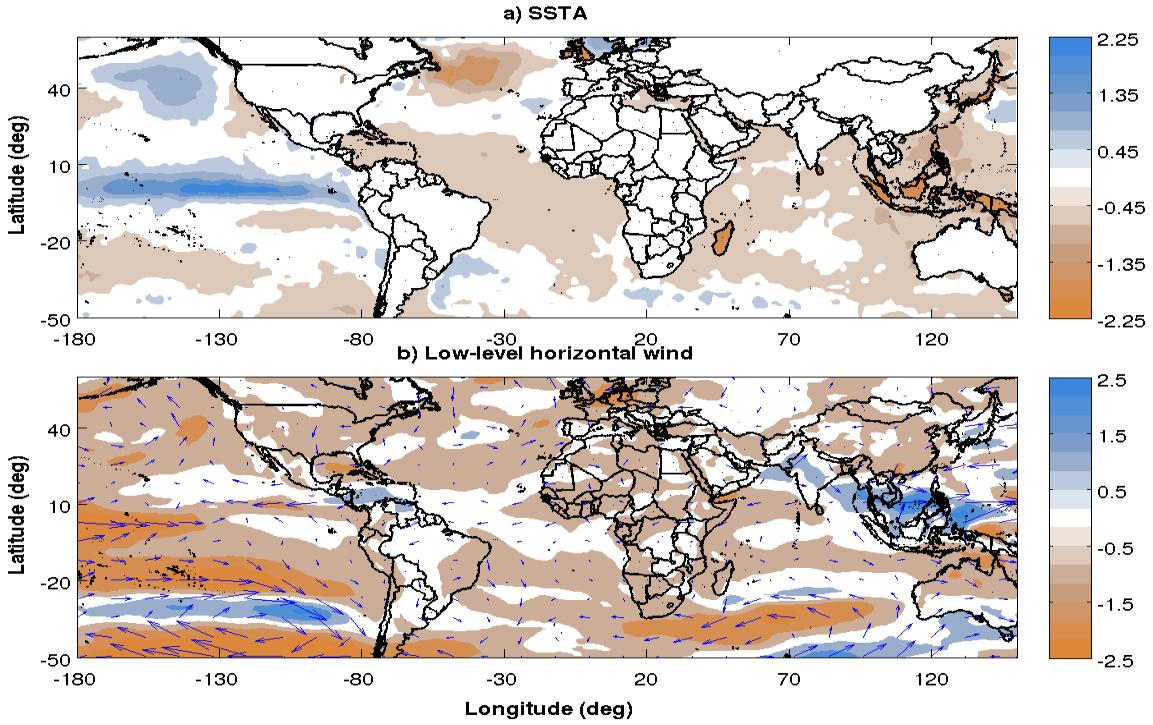

Fig. 6.16) Composite (dry minus wet anomaly years) patterns during summer season, based on summer dominant TPC of SPI3; a) SST, b) Low-level horizontal wind.

The composite of low-level horizontal wind (Fig. 6.16b) shows, weaker East African Low Level Jet (EALLJ) and easterly anomaly from Atlantic suggesting unfavorable condition for the generating of rainfall by reducing the moisture influx coming from the Atlantic and Indian ocean. The colder SST anomalies over the northwestern India ocean which results in a weakening of monsoon trough over the Arabian Sea together with the colder Atlantic SST and weakening of St. Helena high result in the weakening of the southwest and northeast pressure gradient and hence weakening the moisture carrying systems towards Ethiopia.

The climatological pattern of upper-level horizontal wind, specifically Tropical Easterly Jet (TEJ) is discussed in section 4.5.1. The development of this jet; which is related to the thermal wind pattern during the north hemisphere summer. The TEJ is similar to STWJ associated with rainfall by enhancing/suppressing of the vertical motion (Diro 2008). The composite of upper-level horizontal wind (Fig. 6.17a) suggests that a weak TEJ is strongly associated with drought events over the northern and central regions of Ethiopia, in agreement with Grist and Nicholson (2001). This by turn associated with increasing SST over EEPc and decreasing of pressure at high altitude over northern and South Africa; which is a conducive event for the decrement of TEJ. Similar composite patterns of upper-level horizontal wind based on first dominant RPC of EEPc consolidate the above discussion (Fig. 6.17b). The result shows like spring season the positive phase of ENSO enhances westerly anomaly (Rossby wave); which emanates from the eastern equatorial Pacific and propagates eastward, and the easterly upper-level horizontal wind (TEJ) decreases. During negative phase of ENSO TEJ become strengthen because, this phase enhances the easterly Rossby wave; which is a favorable condition for upward motion over EEPc and strongly associated with wet condition over the country.

As spring season the variability of high-pressure systems affects significantly the moisture carrying low-level horizontal winds from neighboring ocean basins for example the weakening and shift of Azores high are highly associated with dry events of northern regions of Ethiopia (Fig. 6.18a, b). The sea level pressure composite (Fig. 6.18a) indicates positive anomaly of southeast of South Africa and around Arabian high are contemporary events with dry conditions of Ethiopia. At the same time, air temperature decreases over western Indian and equatorial Atlantic Ocean and increases over EEPc (Fig. 6.19); this may be a favorable condition for the strength of Rossby wave.

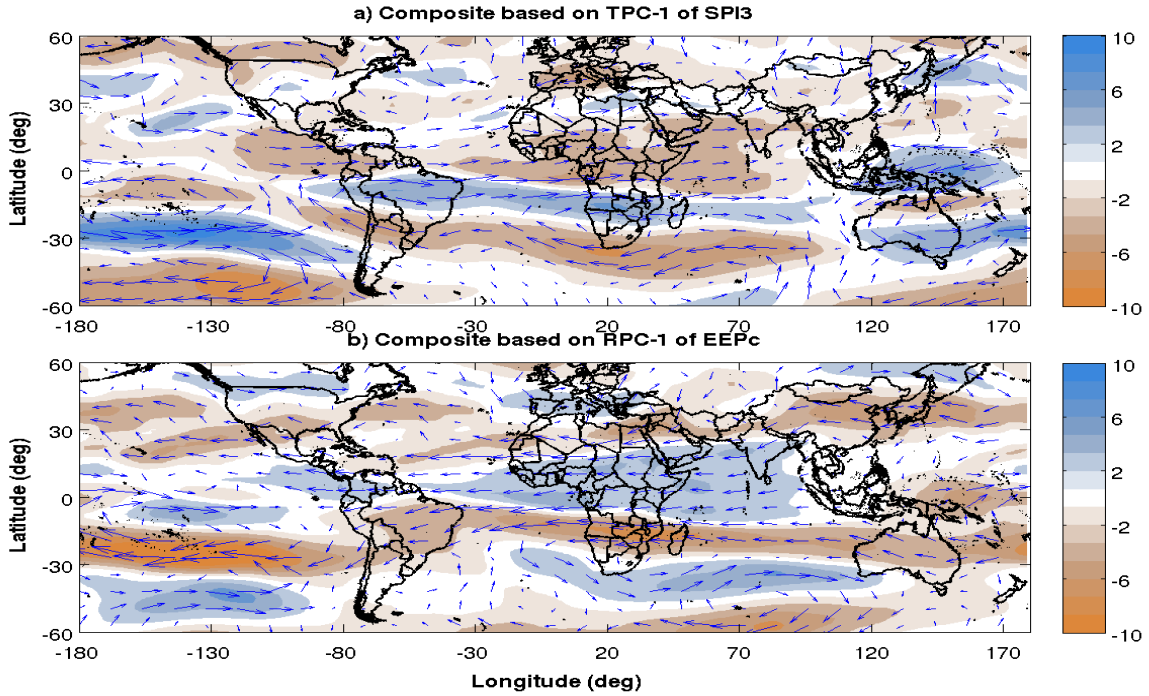

Fig. 6.17) Composite of upper-level horizontal wind during summer season: a) dry minus wet anomaly patterns, based on summer dominant TPC of SPI3; b) cool minus warm anomaly patterns, based on dominant RPC of EEPc.

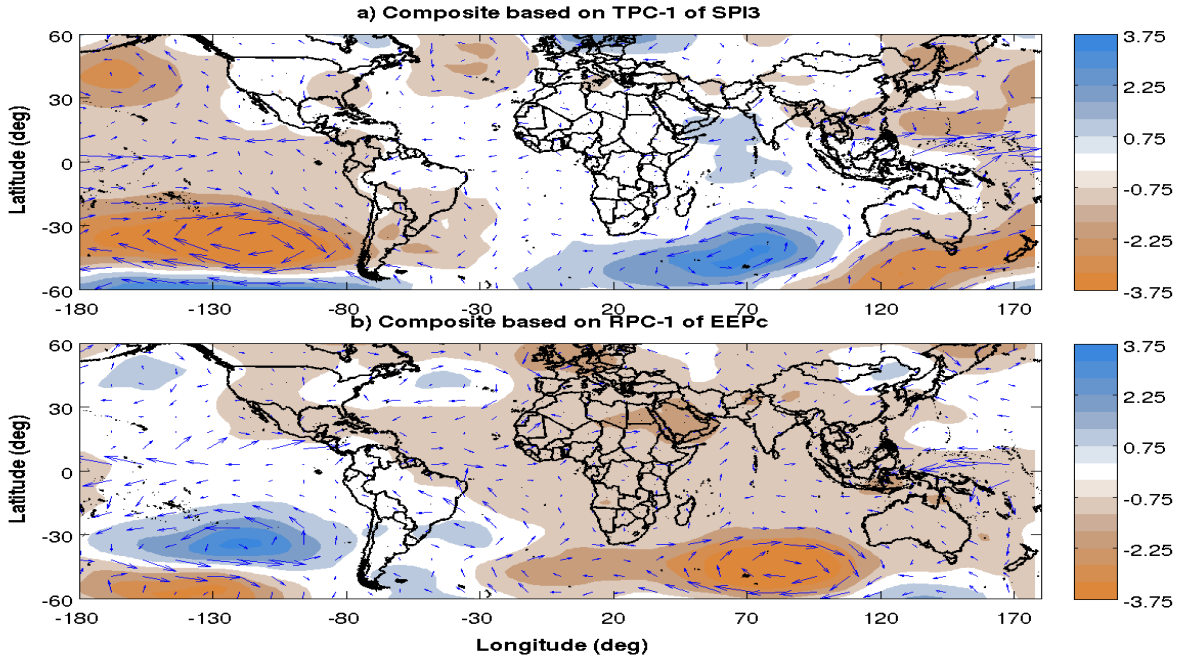

Fig. 6.18) Composite of sea-level pressure during summer season: a) dry minus wet anomaly patterns, based on summer dominant TPC of SPI3; b) cool minus warm anomaly patterns, based on dominant RPC of EEPc.

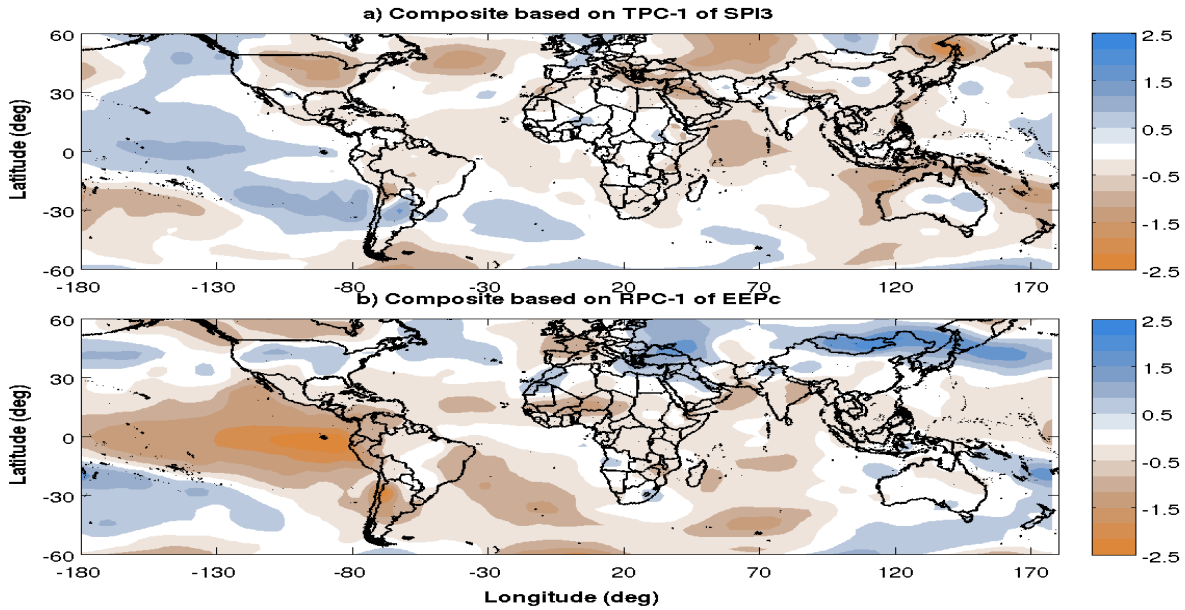

Fig. 6.19) Composite of surface air temperature during summer season: a) dry minus wet anomaly patterns, based on summer dominant TPC of SPI3; b) cool minus warm anomaly patterns, based on dominant RPC of EEPc.

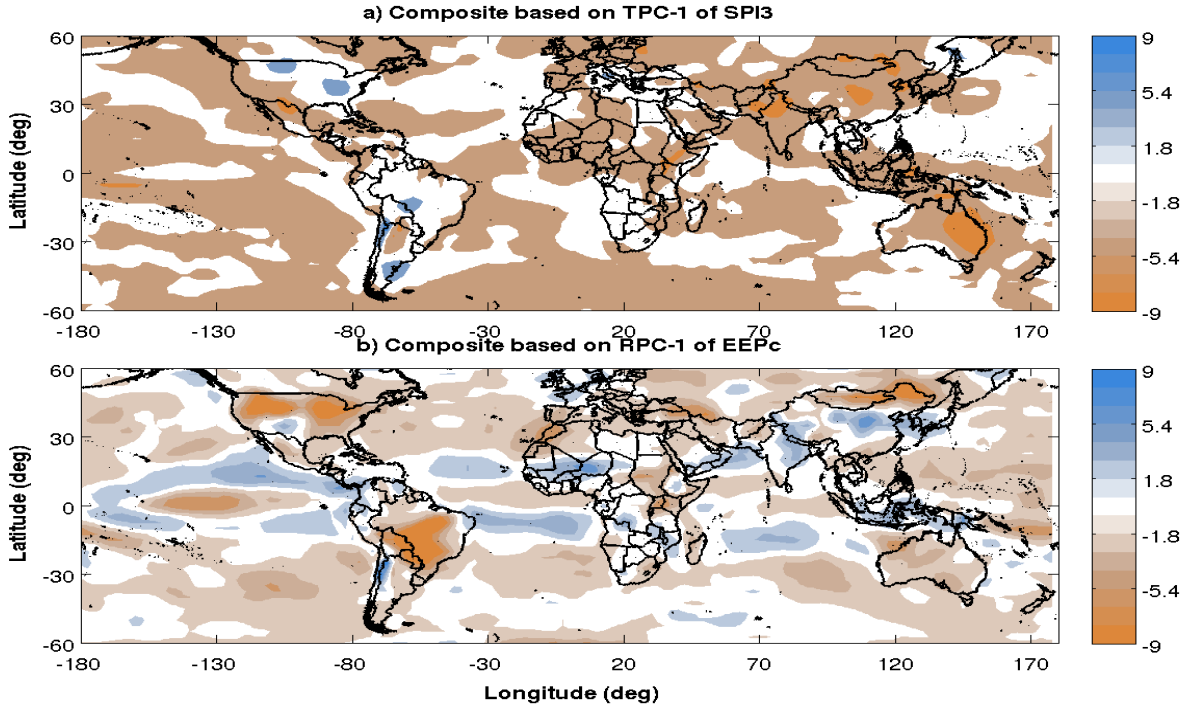

Fig. 6.20) Composite of surface relative humidity during summer season: a) dry minus wet anomaly patterns, based on summer dominant TPC of SPI3; b) cool minus warm anomaly patterns, based on dominant RPC of EEPc.

The composite of relative humidity (Fig. 6.20) confirms the above discussion; which is decreasing over the country because of decrement of rain-generating mechanisms. All the above evidences confirm the physical link of EEPc with Ethiopian climate via altering the large-scale circulation; which responsible for rainfall mechanism over the country.

Table 6.2) Correlation magnitude of dominant modes.

Dominant modes		correlation	Dominant modes		correlation
SPI3-1,2	LHW-1,4	0.48,0.71	SPI3-1	EEPc-1	0.67
SPI3-1,2	UHW-1,5	0.78,0.63	In-4	LHW-1	0.44
SPI3-1	At-3	0.45	EEPc-1	UHW-1	0.76
SPI3-1	In-4	0.68	At-3	LHW-1	0.52

Some dry events are observed during negative anomaly years of east pacific (eg. 1984/85, Fig. 6.21a). At the same time the negative phase of IOD and warming of Gulf of Guinea are observed; which change the low-level dynamics (Fig. 6.21b). The anomaly of upper-level horizontal wind indicates insignificant change in the strength of TEJ (Fig. 6.22a). This gives sense, both moisture-carrying systems and TEJ should be favorable for generation of rainfall during summer season.

The composite pattern of sea level pressure suggests that the weakening St. Helena and Mascarene are causes shift of ITCZ from its usual pattern; which highly connected with variability of rainfall (Fig. 6.22b). Indian and Atlantic Ocean control dry events observed in negative anomaly years of EEPc by change the low-level moisture carrying horizontal wind.

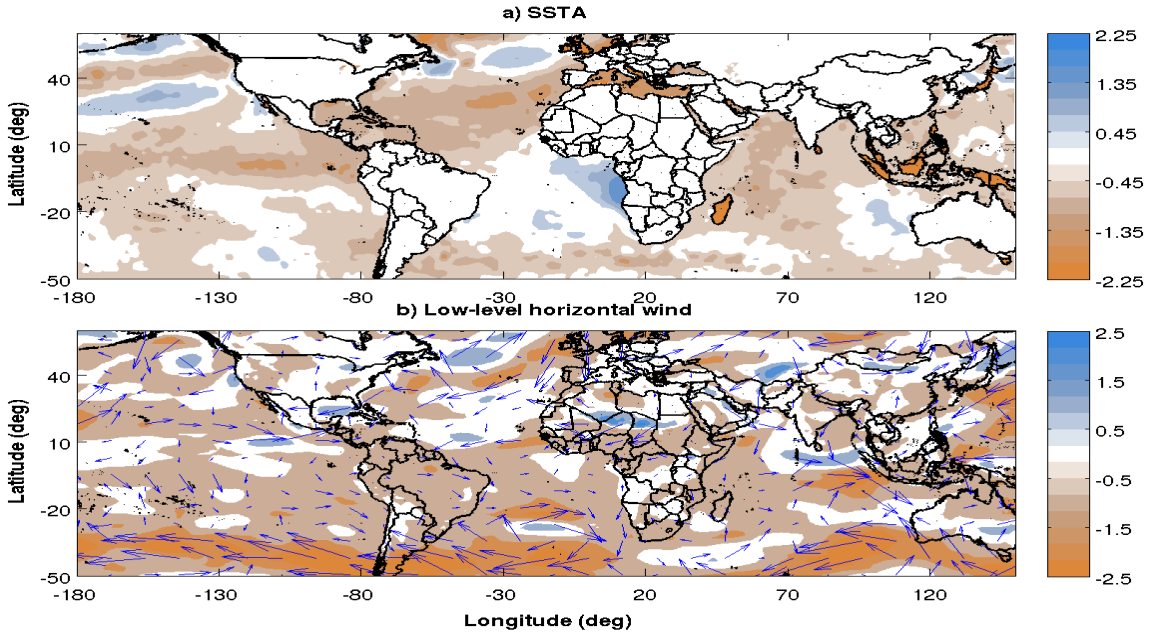

Fig. 6.21) Summer season anomaly patterns of during 1984 (example of dry year); a) SST, b) Low-level horizontal wind.

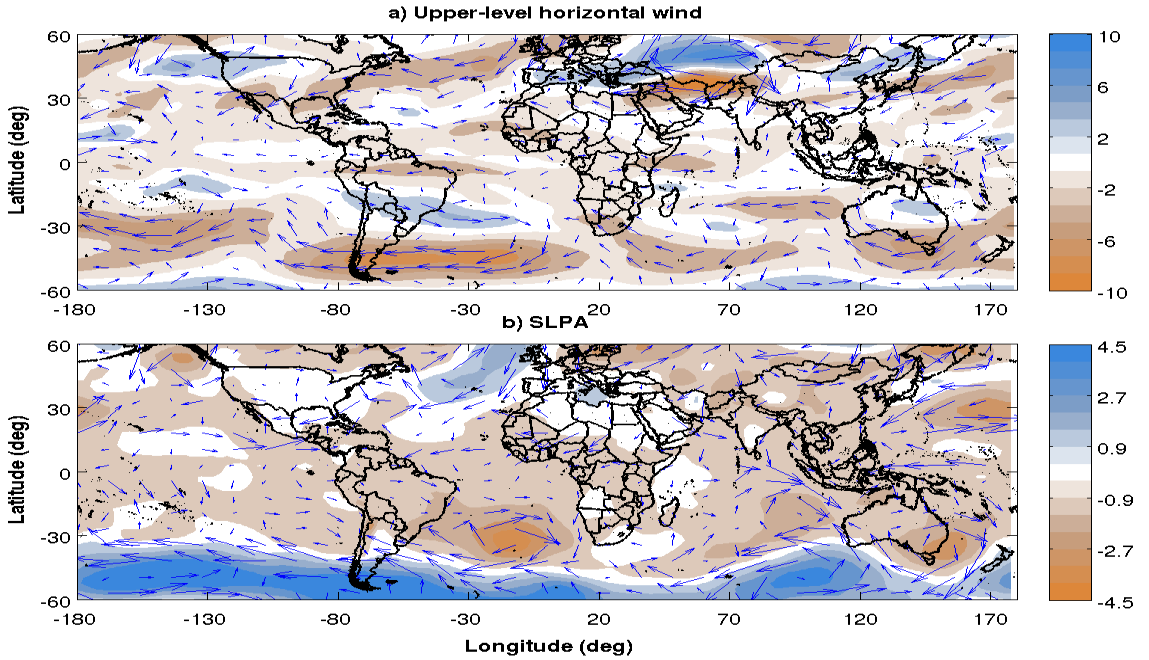

Fig. 6.22) Summer season anomaly patterns of during 1984 (example of dry year); a) Upper-level horizontal wind, b) Sea level Pressure with low-level horizontal wind anomaly vector.

6.2.1. Discussions on Summer large scale features

The mechanisms contributing to the teleconnection between ENSO and summer drought events are examined based on atmospheric variables including upper/low-level horizontal wind, SSTA, surface pressure and relative humidity. The negative correlation pattern unlike to spring over EEPc and negative correlation pattern in other ocean basins indicates the linear association of these ocean basins and SPI3 over the country. The composite analysis suggests that most of extreme dry events of summer season are associated with positive anomaly of EEPc, decreasing of upper and low level wind, increasing Mascarene, decreasing Azores and decreasing of relative humidity. Some dry events (e.g. 1984/85) are observed during weak negative anomaly EEPc. At the same time weak negative IOD and warming coast of Guinea are observed; which play important role to alter the low-level horizontal wind that carry moisture from neighboring ocean basins towards the country. Warming of cost of Guinea may cause decrement of St. Helena; which is highly connected with climate of Ethiopia during summer season.

We found ENSO modulates summer precipitation in Ethiopia by increased convection over the EEPc associated with warm phase of basin and produces anomalous divergence in the upper troposphere that initiates an eastward propagating Kelvin wave; which is against TEJ. Following this condition, the upward motion enhancing mechanism (TEJ) decreases, this is strongly associated with dry conditions of Ethiopia. Thus, intra-annual variability of summer rainfall over Ethiopia is linked to ENSO variability in the EEPc via an eastward/westward propagating atmospheric Kelvin/mixed Rossby-Gravity wave; which alters the strength of TEJ.

6.3. Conclusions

The evidence presented in this study indicates that the seasonal anomalies of all ocean basins are strongly linked with Ethiopian climate in spring and summer seasons via large-scale circulation. A negative/positive SSTA over equatorial east Pacific; which may alter the rain producing large scale circulation over Ethiopia, is significantly correlated with dry/wet events in spring and wet/dry events in summer. During negative anomaly years of EEPc

weakening/strengthen the upper-level horizontal wind (STWJ/TEJ), this may be because of the enhancement of mixed Rossby-gravity (easterlies) and decrement of Kelvin wave (which provides westerly momentum) in spring/summer seasons (Fig. 6.23). Because of the opposite climatological directions of these systems, these waves affects oppositely, hence negative anomaly of EEPc associated oppositely that of summer season. Occasionally dry events are observed during positive/negative anomaly years of east pacific (e.g. 1992/1984) in spring/summer season. In this case, neighboring ocean basins play important role by altering moisture-carrying systems towards the country. This condition supported by unfavorable conditions of high-pressure systems. Of course, severe drought events are strongly associated with unfavorable conditions of both upper and low-level horizontal wind. Hence low-level horizontal winds mostly affected by neighboring ocean basins, whereas upper-level horizontal wind more by EEPc ocean. So, these oceanic basins parameters can be used as indicators of drought occurrence over the country.

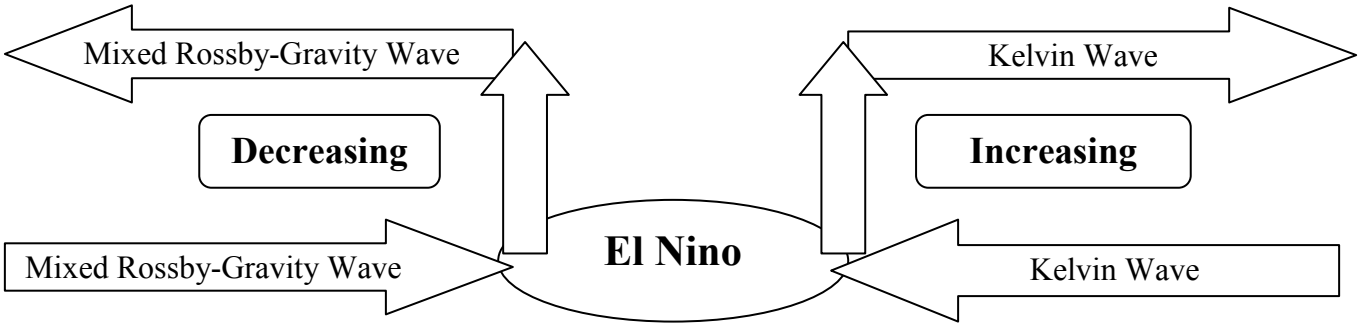

Fig. 6.23) The features of Kelvin and mixed Rossby-Gravity waves during positive anomaly years of EEPc SST in both seasons.

CHAPTER - SEVEN

Conclusion

The drought detection, trend, frequency of occurrences and severity as well as the governing physical mechanisms have been investigated in this dissertation. Extensive datasets from observations and model simulations are employed for this purpose. A number of analysis tools such as trend-eof, composite and wavelet analyses as well as various measures of bias and dispersion for comparison of datasets as well as results of analysis from different methods are utilized. The descriptions of datasets and methods employed in this work are described.

Evaluations of performance of regional climate model (RegCM4) in reproducing observations and known climatology of major circulation patterns are made against reanalysis and observational datasets. The evaluations were performed with respect to spatial and temporal varabilities of rainfall, temperature and wind fields. Analyses of climatological patterns of large scale circulation (i.e., low-level horizontal wind averaged over 850-1000 hPa, upper-level horizontal wind averaged over 100-300 hPa and latitudinal cross-section of vertical profile of horizontal wind averaged over longitude range of 40W-80E), temperature climatology over the whole domain of simulation i.e., African domain, and rainfall over Ethiopia have been performed. The results of the analysis have shown that the model performance is accurate enough and it has reproduced the various observations with sufficient accuracy. For instance, RegCM4 have reproduced summer (more detail can be found in Zeleke et al, 2012) and spring rainfall climatology over complex Ethiopian topography with minor wet bias over highlands and dry bias over lowlands. This bias is common features of most climate models as the convection scheme are still far from perfect. To this effect, Grell convection with Frisch closure assumption over land and Emanuel scheme over oceans are used to reduce the bias.

The mean annual cycle of rainfall over the homogeneous rainfall regimes is well reproduced in the model. The correlation coefficients between simulated and observed rainfall anomalies normalized by the standard deviation over the 12 climate sub-regions during spring

and summer season and between the first two dominant RPCs show the ability of RegCM4 simulation to reproduce intra-annual variability of rainfall over Ethiopia. Moreover, time series of all observational and reanalysis atmospheric variables during both seasons in each homogeneous rainfall zones as well as dominant TPCs or RPCs are associated nicely with the corresponding model simulations (i.e., correlation > 0.80).

As a result, the model outputs are subsequently used to derive drought indices in parallel with observations. Standardized Precipitation Index (SPI) and Palmer Drought Severity Index (PDSI) are two of several such indices chosen for this work. SPI and PDSI, derived from observation and RegCM4 simulations, are used for expressing the severity of dry and wet conditions in Ethiopia. The spatial and temporal variations including trend of dry conditions in Ethiopia are investigated based on time series SPI and PDSI indices for the 1982 – 2009 period. The indices are derived for both observation and models. Though there is good agreement between observational climate variables such as rainfall and corresponding model simulation, the association of indices derived from the two datasets is evaluated as a precaution. As a result, high correlations between trend-principal component (TPC) of observational and RegCM4 driven indices (i.e., PDSI and SPI12) are found. For instance, the correlations between the first dominant TPCs are 0.86 (PDSI) and 0.87 (SPI12) while those between second dominant TPCs are 0.83 (PDSI) and 0.71 (SPI12). Similarly, there is very good associations between corresponding TEOFs. Therefore, in subsequent discussion, we refer to the general outcomes of both data sets than to the model or observation individually.

The first dominant TEOF-1 of the two indices are localized mainly over the southern regions. This TEOF shows high magnitude positive pattern over southern regions and small magnitude negative pattern over northwestern regions. Its time component, TPC-1, shows significant dry trend. Moreover, TPC-1 exhibits low frequency high power signals during the recent decade. In contrast, the second TEOF-2, localized mainly over northern regions, does not exhibit well defined linear trend. As a result, its wavelet spectra shows moderate to high frequency high power signals.

The number of percentile severely and extremely dry months (PDSI < -2.99 and SPI12 < -1.49) are analyzed. It confirms that the frequencies of dry years for the whole period are lower over northern regions than the southern regions especially during recent two heptads. Furthermore, seasonal contributions for the specific drought year are also assessed. The first dominant TEOF-1 of the spring season is localized over eastern half of the country. The associated trend principal component, TPC-1, shows significant dry trend whose wavelet spectra shows low frequency high power signals during ~1987/88 and ~1995 – 999 periods. The second TPC-2 of this season represents the western regions, whose wavelet spectrum is dominated by high frequency signals during ~1992- ~1995 without significant trend. In contrast, summer season first dominant TPC-1 represents southern regions and its wavelet spectra is dominated by high frequency signals without significant trend. The TPC-2 of this season describes the northern regions and characterized by wet trend. The TPC-2 wavelet power spectra shows relatively low frequency signals during first decade.

The underlying dynamics that govern drought occurrence, trend, and severity is the SST over the different ocean basins and their interactions. Drought conditions during spring are significantly associated with the negative phase of ENSO, the weakening of the Arabian High and the subtropical westerly jet streams. On the other hand, drought conditions during summer are linked to the positive ENSO phase, a weakening of the upper level jet streams and a lower level moisture influx from the Atlantic and Indian oceans.

In summary, this work is the first compressive investigation of recurrent drought over Ethiopia. Efforts were also made to understand the drought governing dynamics from both observation and high-resolution regional climate models. Further investigation on data with longer period is still required in order to fully understand the drought dynamics and its potential predictability for development of drought early warning system.

Appendix-A Statistical methods

I. Calculation of Empirical Orthogonal Function (EOF)

We suppose that we have a gridded data set composed of a space-time field x(t,s) representing the value of the field x. The value of the field at discrete time t_i and grid point $s_{j\,((x,y)/(x,y,z))}$ is denoted x_{ij} for i = 1,2,…,n and j = 1,2,…,p. The observed field is:

$$x = (x_1, x_2, x_3, \dots, x_N)^T = \begin{pmatrix} x_{11} & x_{12} & \vdots & \vdots & \vdots & x_{1p} \\ x_{21} & x_{22} & \vdots & \vdots & \vdots & x_{2p} \\ \cdot & \cdot & \cdot & \cdot & \cdot & \cdot \\ \vdots & \vdots & \vdots & \vdots & \vdots & \vdots \\ x_{n1} & x_{n2} & \cdot & \cdot & \cdot & x_{np} \end{pmatrix} or$$

The time average of the field at the i^{th} spatial grid point is given by:

$$\bar{x}_i = \frac{1}{n}\sum_{k=1}^{n} x_{ki}$$

The climatology of the field is defined by

$$\bar{x} = \left(\bar{x}_1, \dots, \bar{x}_p\right) = \frac{1}{n} 1_n^T \, x$$

The anomaly field or departure from the climatology is defined at (t, s) by:

$$x'_{ts} = (x_{ts} - \bar{x}_{ts})$$

Or in matrix form

$$X' = (X - 1\bar{X})$$

where $1=(1,\dots,1)^T$ is the column vector containing n ones. Once the anomaly data matrix is determined, the covariance matrix is then defined by:

$$S = \frac{1}{n-1} X^T X$$

which contains the covariances S_{ij}, i, j = 1, . . .p, between the time series of the field at any pair of grid points (s_i, s_j), i.e.

$$s_{ij} = [S]_{ij} = \frac{1}{n}\sum_{t=1}^{n} x_{ti}\, x_{tj}$$

The aim of EOF analysis/PCA is to find uncorrelated linear combinations of the different variables that explain maximum variance, that is to find a unit-length direction $u = (u_1, \ldots, u_p)^T$ such that X**u** has maximum variability.

This readily yields:

$$\max(u^T S u), \qquad u^T u = 1$$

The EOFs are therefore obtained as the solution to the eigenvalue problem:

$$Su = \lambda^2 u$$

The k^{th} EOF is simply the k^{th} eigenvector u_k of S. The corresponding eigenvalue λ_k^2, k= 1, . . .p is then

$$\lambda_k^2 = u_k^T S u_k = \frac{1}{n}\|X u_k\|^2$$

and hence gives a measure of the variance of the data accounted for in the direction u_k. After finding the eigen elements of the sample covariance matrix *S*, the eigenvalues are normally sorted in decreasing order as $\lambda_1^2 \geq \lambda_2^2 \ldots \geq \lambda_p^2$. It is usual to write the variance accounted for in percentage as:

$$\frac{100\lambda_k^2}{\sum_{k=1}^{p}\lambda_k^2}\%$$

The projection of the anomaly field *X* onto the k^{th} EOF $u_k = (u_{k1}, u_{k2}, \ldots, u_{kp})^T$, i.e. $a_k = Xu_k$ is the k^{th} PC whose elements a_{tk}, t = 1, . . .n, are given by:

$$a_{tk} = \sum_{j=1}^{p} x_{tj}\, u_{kj}$$

So the k^{th} eigenvalue λ_k^2 represents the variance of the k^{th} PC $a_k = (a_{1k}, a_{2k}. \ldots a_{nk})^T$.

North (North et al. 1982) has proposed the rule of thumb to select significant EOF. He estimated typical errors using the eigenvalues of the covariance matrix, λ_k, and the number of statistically independent samples in the data

$$\Delta\lambda_k \approx \left|\sqrt{\frac{2}{n}}\lambda_k\right|$$

Trend-EOF analysis considers a new matrix, $Q = (\mathbf{q}_1, \mathbf{q}_2 \ldots \mathbf{q}_p)$ of time positions of sorted data (the inverse-ranks of the data) of x; Inverse ranks in Q need to be weighted by the cosine of the corresponding latitude in order to correct for the non-uniform data distribution on the geographic grid. Then by similar procedure of EOF we can decompose in to dominant trended mode with pattern and non-trend modes.

Appendix-B Dynamical equation of the Model

Model is a mathematical or computer-coded representation of dynamical, physical, chemical and radiative processes and feedbacks in the atmosphere (Fig. A1). These processes are described by time dependent (ordinary differential), space and time dependent (partial differential), parameterized and empirical equations. Regional climate models (higher spatial resolution = a more detailed representation of information) are important which, provides the capability of more accurately represent a wider range of physical processes, Improving our ability to understand and predict changes in the Earth‟s environment and enhance society‟s ability to plan and respond. Among processes, climate model that simulates gas, aerosol, cloud,

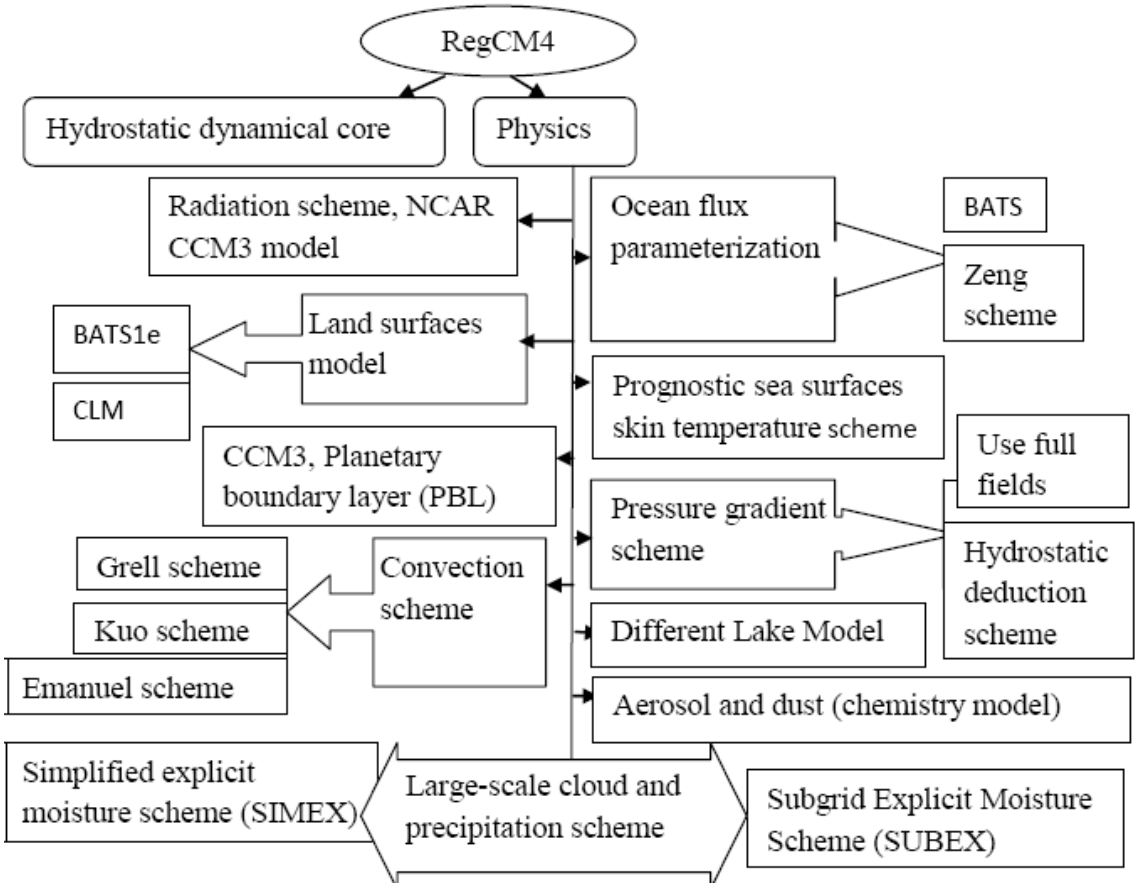

Fig. A1) Diagram of atmospheric processes considered by RegCM4.

radiative, dynamical, transport and surface processes are shown in Fig. A2. See below basic dynamical equations of the model,

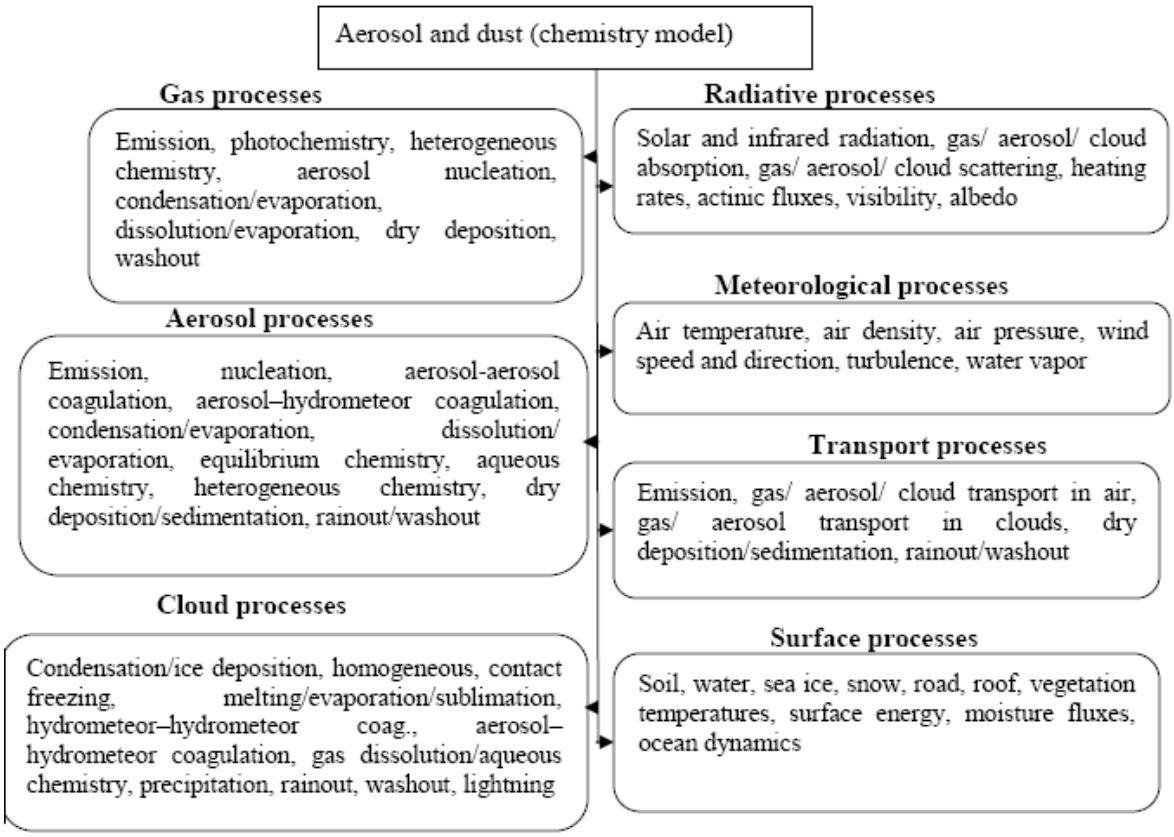

Fig. A2) Diagram of processes simulated in an air pollution–weather–climate model (Jacobson 2005).

I. The vector form of the momentum equation

$$\frac{dV}{dt} = -fK \times V - \nabla\Phi - \frac{1}{\rho_a}\nabla P_a + \frac{\eta_a}{\rho_a}\nabla^2 V + \frac{1}{\rho_a}\left(\nabla . \rho_a K_m \nabla\right)V$$

Local acceleration=Coriolis force perunit mass + Effective gravitational force per unit mass + Pressure-gradient force per unit mass + Viscous force per unit mass + Turbulent-flux divergence of momentum.

Horizontal momentum equation in RegCM4

$$\frac{\partial p^* u}{\partial t} = -m^2\left(\frac{\partial p^* uu/m}{\partial x} + \frac{\partial p^* vu/m}{\partial y}\right) - \frac{\partial p^* u\dot{\sigma}}{\partial \sigma} - mp^*\left[\frac{RT_v}{(p^* + p_t/\sigma)}\frac{\partial p^*}{\partial x} + \frac{\partial \phi}{\partial x}\right] + fp^* v + F_H u + F_V u \quad (3.1)$$

$$\frac{\partial p^* v}{\partial t} = -m^2\left(\frac{\partial p^* uv/m}{\partial x} + \frac{\partial p^* vv/m}{\partial y}\right) - \frac{\partial p^* v\dot{\sigma}}{\partial \sigma} - mp^*\left[\frac{RT_v}{(p^* + p_t/\sigma)}\frac{\partial p^*}{\partial y} + \frac{\partial \phi}{\partial y}\right] + fp^* u + F_H v + F_V v \quad (3.2)$$

where u and v are the eastward and northward components of velocity, T_v is virtual temperature, ϕ is geopotential height, *f* is the coriolis parameter, *R* is the gas constant for dry air, *m* is the map scale factor for either the Polar Stereographic, Lambert Conformal, or Mercator map projections, $\dot{\sigma} = \frac{d\sigma}{dt}$, and F_H and F_V represent the effects of horizontal and vertical diffusion, and $p^* = p_s - p_t$.

II. The continuity equation

Continuity equation for a gas *q*

$$\frac{\partial N_q}{\partial t} + \nabla.\left(VN_q\right) = (\nabla. k_h \nabla)N_q + R_{emisg} + R_{depg} + R_{washg} + R_{chemg} + R_{nucg} + R_{c/eg} + R_{dp/sg} + R_{ds/eg} + R_{hrg}$$

The continuity equation for the number concentration of particles of size *i* is

$$\frac{\partial n_i}{\partial t} + \nabla.(Vn_i) = (\nabla. k_h \nabla)n_i + R_{emisn} + R_{depn} + R_{sedn} + R_{washn} + R_{nucn} + R_{coagn}$$

The continuity equation for the volume concentration of component q in particles of size *i* is

$$\frac{\partial v_{q,i}}{\partial t} + \nabla.\left(Vv_{q,i}\right) = (\nabla. k_h \nabla)v_{q,i} + R_{emisv} + R_{depv} + R_{sedv} + R_{washv} + R_{nucv} + R_{coagv} + R_{c/ev} + R_{dp/sv} + R_{ds/ev} + R_{eqv} + R_{aqv} + R_{hrv}$$

Where; R_{emisv} = rate of surface or elevated emission, R_{depv} = rate of dry deposition to the surface, R_{sedv} = rate of sedimentation to the surface or from one altitude to another, R_{washv}= rate of washout to the surface or from one altitude to another, R_{nucv} = rate of change due to

homogeneous or heterogeneous nucleation, R_{coagv} = rate of change due to coagulation, $R_{c/ev}$ = rate of change due to condensational growth (evaporation), $R_{dp/sv}$ = rate of change due to depositional growth (sublimation), $R_{ds/ev}$ = rate of change due to dissolutional growth (evaporation), R_{eqv} = rate of change due to reversible chemical equilibrium reactions, R_{aqv} = rate of change due to irreversible aqueous chemical reactions, R_{hrv} = rate of change due to heterogeneous reactions on particle surfaces

Rates in this equation have units of cubic centimeters of component q per cubic centimeter of air per second. Some processes, such as homogeneous nucleation and coagulation, affect number and volume concentrations. Others, such as heterogeneous nucleation, condensation, deposition, dissolution, heterogeneous reaction, chemical equilibrium and aqueous chemistry affect volume concentration but not number concentration.

Water in the atmosphere appears as a gas, liquid, or solid. In a model, the total water content is estimated as

$$q_T = q_v + \sum_{i=1}^{N_B} \left(q_{L,i} + q_{I,i}\right)$$

where N_B is the number of particle size categories (bins), q_v is the specific humidity of water vapor (kilograms per kilogram of moist air), $q_{L,i}$ is the moist-air mass mixing ratio of liquid water in a size bin, and $q_{I,i}$ is the moist-air mass mixing ratio of ice in a size bin. Mass mixing ratios are determined from the continuity equations for water vapor, liquid, and ice,

$$\frac{\partial q_v}{\partial t} + (V.\nabla)q_v = \frac{1}{\rho_a}\left(\nabla \rho_a k_h \nabla\right)q_v + R_{emisv} + R_{depv} + R_{chemv} + R_{c/ev} + R_{dp/sv} + R_{ds/ev}$$

$$\frac{\partial q_{L,i}}{\partial t} + (V.\nabla)q_{L,i} = \frac{1}{\rho_a}\left(\nabla \rho_a k_h \nabla\right)q_{L,i} + R_{emisL} + R_{depL} + R_{sedL} + R_{coagL} + R_{c/eL} + R_{f/mL}$$

$$\frac{\partial q_{I,i}}{\partial t} + (V.\nabla)q_{I,i} = \frac{1}{\rho_a}\left(\nabla \rho_a k_h \nabla\right)q_{I,i} + R_{depI} + R_{sedI} + R_{coagI} + R_{f/mI} + R_{dp/sI}$$

Where; R_{emis} = rate of surface or elevated emission, R_{dep} = rate of dry deposition to the surface, R_{sed} = rate of sedimentation to the surface or from one altitude to another, R_{chem}= rate of photochemical production or loss, R_{coag}= rate of liquid or ice production or loss in a size bin due to coagulation, $R_{c/e}$ = rate of change due to condensational growth (evaporation), $R_{dp/s}$ = rate of change due to depositional growth (sublimation), $R_{f/m}$ = rate of change due to freezing (melting) and the units of R are kilograms per kilogram of moist air per second.

Continuity and Sigma dot ($\dot{\sigma}$) Equations in RegCM4

$$\frac{\partial p^*}{\partial t} = -m^2\left(\frac{\partial p^* u/m}{\partial x} + \frac{\partial p^* v/m}{\partial y}\right) - \frac{\partial p^* \dot{\sigma}}{\partial \sigma} \tag{3.3}$$

The vertical integral of Equation 3.3 is used to compute the temporal variation of the surface pressure in the model,

$$\frac{\partial p^*}{\partial t} = -m^2\int_0^1\left(\frac{\partial p^* u/m}{\partial x} + \frac{\partial p^* v/m}{\partial y}\right)d\sigma \tag{3.4}$$

After calculation of the surface-pressure tendency$\frac{\boldsymbol{\partial p^*}}{\boldsymbol{\partial t}}$, the vertical velocity in sigma coordinates ($\dot{\sigma}$) is computed at each level in the model from the vertical integral of Equation 3.3.

$$\dot{\sigma} = -\frac{1}{p^*}\int_0^\sigma\left[\frac{\partial p^*}{\partial t} + m^2\left(\frac{\partial p^* u/m}{\partial x} + \frac{\partial p^* v/m}{\partial y}\right)\right]d\sigma' \tag{3.5}$$

where σ‟ is a dummy variable of integration and $\dot{\sigma}(\sigma = 0) = 0$.

III. **Thermodynamic energy equation**

$$\frac{\partial \theta_v}{\partial t} + (V.\nabla)\theta_v = \frac{1}{\rho_a}(\nabla \rho_a k_h \nabla)\theta_v + \frac{\theta_v}{c_{p,d}T_v}\sum_{n=1}^{N_{e,h}}\frac{dQ_n}{dt}$$

$$\frac{dQ}{dt} = \sum_{n=1}^{N_{e,h}}\frac{dQ_n}{dt} = \frac{dQ_{c/e}}{dt} + \frac{dQ_{f/m}}{dt} + \frac{dQ_{dp/s}}{dt} + \frac{dQ_{solar}}{dt} + \frac{dQ_{ir}}{dt}$$

Where; $N_{e,h}$ is the number of diabetic energy sources and sinks. All Q‟s are in joules per kilogram.$dQ_{c/e}/dt$ is the rate of energy release (absorption) due to condensation (evaporation),

$dQ_{f/m}/dt$ is the rate of energy release (absorption) due to freezing (melting), $dQ_{dp/s}/dt$ is the rate of energy release (absorption) due to deposition (sublimation), dQ_{solar}/dt is the rate of solar heating, and dQ_{ir}/dt is the rate of net infrared heating (cooling).

Thermodynamic Equation and Equation for Omega (ω) in RegCM4

$$\frac{\partial p^* T}{\partial t} = -m^2\left(\frac{\partial p^* uT/m}{\partial x} + \frac{\partial p^* vT/m}{\partial y}\right) - \frac{\partial p^* T\dot{\sigma}}{\partial \sigma} + \frac{RT_v\omega}{c_{pm}(\sigma + p_t/p_{ast})} + \frac{p^* Q}{c_{pm}} + F_H T + F_V T \quad (3.6)$$

where c_{pm} is the specific heat for moist air at constant pressure, Q is the diabatic heating, $F_H T$ represents the effect of horizontal diffusion, $F_V T$ T represents the effect of vertical mixing and dry convective adjustment, and ω is

$$\omega = p^*\dot{\sigma} + \sigma\frac{dp^*}{dt}, where \quad (3.7)$$

$$\frac{dp^*}{dt} = \frac{\partial p^*}{\partial t} + m\left(u\frac{\partial p^*}{\partial x} + v\frac{\partial p^*}{\partial y}\right) \quad (3.8)$$

The expression for $c_{pm} = c_p(1+0.8q_v)$, where c_p is the specific heat at constant pressure for dry air and q_v is the mixing ratio of water vapor.

Hydrostatic Equation in RegCM4

The hydrostatic equation is used to compute the geopotential heights from the virtual temperature T_v,

$$\frac{\partial \phi}{\partial ln(\sigma + p_t/p^*)} = -RT_v\left[1 + \frac{q_c + q_r}{1 + q_v}\right]^{-1} \quad (3.9)$$

where $T_v = T(1+0.608q_v)$, q_v, q_c, and q_r are the water vapor, cloud water or ice, and rain water or snow, mixing ratios. The model dynamic equations and numerical discretization are described by *Grell et al.* [1994].

Bibliography

Adler RF, Huffman GJ, Chang A, Ferraro R, Xie P, Janowiak J, Rudolf B, Schneider U, Curtis S, Bolvin D, Gruber A, Susskind J, Arkin P (2003) The Version 2 Global Precipitation Climatology Project (GPCP) monthly precipitation analysis (1979–present). J Hydrometeorol 4:1147-1167

Alley WM (1984) The Palmer Drought Severity Index: limitations and assumptions. Journal of Climate and Applied Meteorology 23:1100-1109

American Meteorological Society (AMS) (1997) Meteorological drought-Policy statement. Bull. Amer. Meteor. Soc.,78:847-849

American Meteorological Society (AMS) (2004) Statement on meteorological drought. Bull. Am. Meteorol. Soc. 85, 771–773

Anthes RA (1977) A cumulus parameterization scheme utilizing a one dimensional cloud model. Mon Weather Rev 105:270-286

Anyah RO, Semazzi F (2007) Variability of East African rainfall based on multiyear RegCM3 simulations. Inter J Climatol 27:357-371

Barbosa SM and Andersen OB (2009) Trend patterns in global sea surface temperature. Int J Climatol. 29: 2049–2055. doi: 10.1002/joc.1855

Bekele F (1997) Ethiopian use of ENSO information in its seasonal forecasts. Internet J Afr Stud 2. Issue No. 2, March 1997

Beran M and Rodier J (1985) Hydrological aspects of drought-A contribution to the International Hydrological Program. UNESCO/WMO, Geneva

Bhatt U (1989) Circulation regimes of rainfall anomalies in the African-South Asian monsoon belt. Journal of Climate, 2, 1133–1144

Bordi I, Sutera A (2001) Fifty years of precipitation: some spatially remote teleconnections. Water Resour. Manage. 15, 247-280

Bordi I and Sutera A (2007) Drought Monitoring and Forecasting and Large Scale, In G. Rossi, et al., eds. Methods and Tools for drought Analysis and Management. Springer, Dordrecht

Byun HR and Wilhite DA (1999) Objective quantification of drought severity and duration. J. Clim. 12, 2747–2756

Camberlin P (1995) June-September rainfall in northeastern Africa and atmospheric signals over the tropics: a zonal perspective. International Journal of Climatology 15:773-783

Camberlin P (1997) Rainfall anomalies in the source region of the Nile and their connection with the Indian summer monsoon. Journal of Climate 10:1380-1392

Camberlin P and Philippon N (2002) The East African March-May Rainy season: Associated Atmospheric dynamics and predictability over the 1968-97 period. Journal of Climate 15:1002-1019

Chisholm Hugh ed. (1911) Encyclopædia Britannica (11th ed.). Cambridge University Press.

Conway D (2000) Some aspects of climate variability in the northeast Ethiopian highlands-Wollo and Tigray. SINET: Ethiopian Journal of Science 23: 139–161

Cook K (1999) Generation of the African easterly jet and its role in determining West African precipitation. Journal of Climate 12:1165-1184

Copsey D, Sutton R, and Knight JR (2006) Recent trends in sea level pressure in the Indian Ocean region, Geophysical Research Letters, 33, L19712, doi:10.1029/2006GL027175

Davis N, Bowden J, Semazzi F, Xie L, and Onol B (2009) Customization of RegCM3 Regional Climate Model for eastern Africa and a trop ical Indian Ocean domain, J. Clim., 22, 3595–3616, doi:10.1175/2009JCLI2388.1

Dee DP, Uppala SM, Simmons AJ, Berrisford P, Poli P, Kobayashi S, Andrae U, Balmaseda MA, Balsamo G, Bauer P, Bechtold P, Beljaars A, van de Berg L, Bidlot J, Bormann N, Delsol C, Dragani R, Fuentes M, Geer AJ, Haimberger L, Healy SB, Hersbach H, Hólm EV, Isaksen L, Kållberg P, Köhler M, Matricardi M, McNally AP, Monge-Sanz BM, Morcrette JJ, Park BK, Peubey C, de Rosnay P, Tavolato C, Thépaut JN, Vitart F (2011) The ERA-Interim reanalysis: configuration and performance of the data assimilation system. Q J R Meteorol Soc 137:553-597. doi:10.1002/qj.828

Degefu W (1987) Some aspects of meteorological drought in Ethiopia. In: Glantz MH (ed) Drought and Hunger in Africa: denying famine a future. Cambridge University Press, Cambridge, pp 23–36

Denis B, Laprise R, Cˆotˆe J (2002) Donwscaling ability of one-way nested regional climate models: the big-brother experiment. Climate Dynamics 18: 627–646

Dickinson RE, Errico RM, Giorgi F and Bates GT (1989) A regional climate model for the western United States, Climatic Change, 15, 383–422, 1989

Dickinson RE, Henderson SA, Kennedy PJ (1993) Biosphere-Atmosphere Transfer Scheme (BATS) version 1E as coupled to the NCAR Community Climate Model. Technical Note NCAR/TN-387 + STR, p 72

Diro GT (2008) Seasonal forecasting of Ethiopian rainfall. Dissertation, Department of Meteorology, Reading University, Reading

Diro GT, Black E, Grimes DIF (2008) Seasonal forecasting of Ethiopian spring rains. Meteorol Appl 15:73-83

Diro GT, Grimes DIF, Black E (2011a) Teleconnections between Ethiopian summer rainfall and sea surface temperature: part I observation and modeling. Clim Dyn 37:103–119. doi:10.1007/s00382-010-0837-8

Diro GT, Grimes DIF, Black E (2011b) Large scale features affecting Ethiopian rainfall. In: Williams CJR, Kniveton DR (ed). Springer,Dordrecht, pp 13-50

Edwards DC and McKee TB (1997) Characteristics of 20th Century drought in the United States at multiple time scales. Climatology Report Number 97-2, Colorado State University, Fort Collins, Colorado

Emanuel KA, Rothman MZ (1999) Development and evaluation of a convection scheme for use in climate models. J Atmos Sci 56:1756–1782

CIA (2009) Ethiopia: Economy, CIA World Fact book

FAO/WFP 2004 Crop and food supply assessment mission to Ethiopia Food and Agriculture Organization, Rome

FDRE (Federal Democratic Republic of Ethiopia) (1997) Environmental Policy Environmental Protection Authority in collaboration with the Ministry of Economic Development and Cooperation: Addis Ababa

Fritsch JM, Chappell CF (1980) Numerical prediction of convectively driven mesoscale pressure systems. Part I: convective parameterization. J Atmos Sci 37:1722–1733

Funk C, Asfaw A, Steffen P, Senay G, Rowland J, Verdin J (2003) Estimating Meher Crop Production Using Rainfall in the „Long Cycle" Region of Ethiopia. FEWS NET Special Report

Funk C, Rowland J, Eilerts G, Kebebe E, Biru N, White L and Galu G (2012) A Climate Trend Analysis of Ethiopia, U.S. Geological Survey Fact Sheet 2012–3053, 6 p

Gebremariam T (2012) Improved Convective Parametrization for Precipitation Modeling over the GHA, MSc thesis, Addis Ababa University

Giannini A Saravanan R Chang P (2003) Oceanic Forcing of Sahel Rainfall on Interannual to Interdecadal Time Scales, Science Vol. 302 no. 5647 pp. 1027-1030 DOI: 10.1126 1089357

Gibbs WJ and Maher JV (1967) Rainfall deciles as drought indicators. Bureau of Meteorology Bulletin, No. 48, Commonwealth of Australia, Melbourne

Giorgi F and Bates GT (1989) The climatological skill of a regional model over complex terrain, Mon. Wea. Rev., 117, 2325–2347, 1989.

Giorgi F (1990) Simulation of regional climate using a limited area model nested in a general circulation model, J. Climate, 3, 941–963, 1990

Giorgi F, Bates GT, Nieman SJ (1993a) The multi-year surface climatology of a regional atmospheric model over the western United States. J Climate 6:75–95

Giorgi F, Marinucci MR, Bates GT (1993b) Development of a second generation regional climatemodel (RegCM2). I: boundary layer and radiative transfer processes. Mon Weather Rev 121:2794–2813

Giorgi F Mearns L (1999) Introduction to special section. Regional climate modeling revisited. Journal of Geophysical Research 104: 6335–6352

Giorgi F Shields C (1999) Tests of precipitation parameterizations available in latest version of NCAR regional climate model (RegCM) over continental United States. Journal of Geophysical Research 104(D6): 6353–6375

Giorgi F, Bi X (2000) A study of internal variability of a regional, climate model. Journal of Geophysical Research 105(D24): 29503–29521

Giorgi F, Coppola E, Solmon F, Mariotti L, Sylla MB, Bi X, Elguindi N, Diro GT, Nair V, Giuliani G, Turuncoglu UU, Cozzini S, Guettler I, O'Brien TA, Tawfik AB, Shalaby A, Zakey AS, Steiner AL, Stordal F, Sloan LC, Brankovic C (2012) RegCM4: model description and preliminary tests over multiple CORDEX domains. Clim Res 52:7–29

Gissila T, Black E, Grimes DIF, Slingo JM (2004) Seasonal forecasting of the Ethiopian summer rains. International Journal of Climatology 24: 1345–1358

Gommes R and Petrassi F (1994) Rainfall variability and drought in Sub-Saharan Africa since 1960 Agro meteorology Series Working Paper No. 9, Food and Agriculture Organization, Rome, Italy

Grell GA, Dudhia J, Stauffer DR (1994) Description of the fifth generation Penn State/NCAR mesoscale model (MM5). Technical note NCAR/TN-398-STR, p 121

Grist J and Nicholson S (2001) A study of the dynamic factors influencing the rainfall variability in the West African Sahel. Journal of Climate, 14:1337-1359

Guttman NB (1991) A sensitivity analysis of the Palmer Hydrologic Drought Index. Water Resour. Bull, 27:797-807

Guttman NB, Wallis JR and Hosking JRM (1992) Spatial comparability of the Palmer Drought Severity Index. Water Resour. Bull, 28:1111-1119

Guttman NB (1998) Comparing the Palmer Drought Index and the Standardized Precipitation Index. J. Amer. Water Resour. Assoc. 34:113-121

Guttman NB (1999) Accepting the standardized precipitation index: a calculation algorithm. J. Am. Water Resour. Assoc. 35 (2):311–322

Haile T (1987) A case study of seasonal forecasting in Ethiopia. WMO regional association I, Geneva, Switzerland, 53-76

Hannachi A (2007) Pattern hunting in climate: a new method for finding trends in gridded climate data. International Journal of Climatology 27:1-15

Hastenrath S (1990) Climate dynamics of the tropics. Kluwer Academic Publisher

Hastenrath S Polzin D and Camberlin P (2004) Exploring the predictability of the "short rains" at the coast of East Africa. International Journal of Climatology, 24, 1333-1343

Hayes, M., 1996. Drought Indexes National Drought Mitigation Center, University of Nebraska–Lincoln, p. 7 (available from University of Nebraska–Lincoln, 239LW Chase Hall, Lincoln, NE 68583)

Hayes MJ, Svoboda MD, Wilhite DA, Vanyarkho OV (1999) Monitoring the 1996 drought using the standardized precipitation index. Bull. Am. Meteorol. Soc. 80 (3):429-438

Heddinghaus TR and Sabol P (1991) A review of the Palmer Drought Severity Index and where do we go from here? Proceedings, 7th Conf. on Appl. Climatol., 10-13 September 1991, Boston: American Meteorological Society, 242-246

Heim R (2002) A review of twentieth-century drought indices used in the United States. Bull. Am. Meteorol. Soc. 83:1149-1165

Hollinger SE, Isard SA, Welford MR (1993) A New Soil Moisture Drought Index for Predicting Crop Yields. In: Preprints, Eighth Conf. on Applied Climatology, Anaheim, CA, Amer. Meteor. Soc., pp. 187-190

Holton JR and Lindzen RS (1972) An updated theory for the Quasi-Biennial cycle of the tropical stratosphere Journal of the Atmospheric Sciences Vol. 29, pp. 1076-1080

Holton JR and Tan HC (1980) The influence of the equatorial Quasi-Biennial Oscillation on the global atmospheric circulation at 50mb Journal of Atmospheric Science Vol. 37, pp. 2200-2208

Holtslag AAM, DeBruin EIF, Pan HL (1990) A high resolution air mass transformation model for short-range weather forecasting. Mon Weather Rev 118:1561-1575

Hoskins BJ and Karoly D (1981) The steady linear response of a spherical atmosphere to thermal and orographic forcing. J.Atmos. Sci., 38, 1179–1196

Johnson WK, Kohne RW (1993) Susceptibility of reservoirs to drought using Palmer index. J. Water Resour. Plann. Manage. 119 (3):367-387

Jolliffe IT (1987) Rotation of principal components: Some comments. Journal of Climatology, 7: 507–510. doi: 10.1002/joc.3370070506

Jury MR (2010) Ethiopian decadal climate variability Theor Appl Climatol DOI 10.1007/s00704-009-0200-3

Kalnay E Kanamitsu M Kistler R Collins W Deaven D Gandin L Iredell M Saha S White G Woollen J Zhu Y Chelliah M Ebisuzaki W Higgins W Janowiak J Mo KC Ropelewski C Wang J Leetmaa A Reynolds R Jenne R and Joseph D (1996) The NMC/NCAR 40-Year Reanalysis Project. Bull. Amer. Meteor. Soc., 77, 437-471

Karl TR, Quayle RG (1981) The 1980 summer heat wave and drought in historical perspective. Mon. Weather Rev. 109 (10):2055-2073

Karl TR, Koscielny AJ (1982) Drought in the United States: 1895–1981. J. Qimatol. 2:313-329

Karl TR (1983) Some spatial characteristics of drought duration in the United States. J. Climate Appl. Meteor. 22:1356-1366

Karl TR (1986) The sensitivity of the Palmer Drought Severity Index and Palmer's Z-Index to their calibration coefficients including potential evapotranspiration. J. Climate Appl. Meteor. 25:77-86

Kassahun B (1987) Weather systems over Ethiopia. In Proceedings of First Tech. Conf. on Meteorological Research in Eastern and Southern Africa, pages 53–57, Nairobi, Kenya. Kenya Meteorological Department

Kiehl JT, Hack JJ, Bonan GB, Boville BA, Briegleb BP, Williamson DL, Rasch PJ (1996) Description of the NCAR Community Climate Model (CCM3). Technical Report TN-420-STR. NCAR, Boulder, p 152

Kim T, Valdes JB (2003) Nonlinear model for drought forecasting based on a conjunction of wavelet transforms and neural networks. J. Hydrol. Eng. ASCE 8 (6):319-328

Kistler R Kalnay E Collins W Saha S White G Woollen J Chelliah M Ebisuzaki W Kanamitsu M Kousky V Dool H Jenne R Fiorino M (2001) The NCEP-NCAR 50-Year Reanalysis: Monthly Means CD-ROM and Documentation. Bull. Amer. Meteor. Soc., 82:247-268

Korecha D and Barnston A (2007) predictability of June-September Rainfall in Ethiopia. Monthly Weather Review, 135:628-650

Kucharski F Bracco A Yoo JH Molteni F (2007) Low-frequency variability of the Indian monsoon-ENSO relationship and the tropical Atlantic: The "weakening" of the 1980s and 1990s. J. Climate 20:4255-4266

Kucharski F Bracco A Yoo JH Molteni F (2008a) Atlantic forced component of the Indian monsoon interannual variability. Geophys. Res. Lett. 33:L04706, DOI:10.1029/2007GL033037

Kucharski F Sscaife AA Yoo JH Folland CK Kinter J Knight J Fereday D Fischer AM Jin EK Kroger J Lau NC Nakaegawan T Nath MJ Pegion P Rozanov E Schubert S Sporyshev PV Syktus J Voldoire A Yoon JH Zeng N Zhou T (2008b) The CLIVAR C20C project: skill of simulating Indian monsoon rainfall on interannual to decadal timescales. Does GHG forcing play a role? Climate Dynam., published online, DOI: 10.1007/s00382-008-0462-y

Kucharski F Bracco a Yoo JH Tompkins a Feudale L Ruti P Dell"aquila A (2009) A Gill-Matsuno-type mechanism explains the tropical Atlantic influence on African and Indian monsoon rainfall. Quart. J.Roy. Meteor. Soc. 135:569-579, DOI: 10.1002/qj.406

Leung LR, Ghan SJ (1999) Pacific Northwest climate sensitivity simulated by a regional climate model driven by a GCM. Part I: control simulation. Journal of Climate 12:2010–2030

Lindzen RS and Holton JR (1968) A theory of the quasi-biennial oscillation. Journal of the Atmospheric Sciences, 25:1095-1107

Lloyd-Hughes B, Saunders MA (2002) A drought climatology for Europe. Int. J. Climatol. 22:1571-1592

Maruyama T and Tsuneoka Y (1988) Anomalously short duration of the easterly wind phase of the QBO at 50hPa in 1987 and its relationship to an El Nino event J.Meteor. Soc. Japan,66:629-634

Mengistu Tsidu (2012) High-Resolution Monthly Rainfall Database for Ethiopia: Homogenization, Reconstruction, and Gridding J. of climate 25:8422-8443

Mengistu Tsidu and Bayable E (2011) Evidences of climate change signal at local scales in Ethiopia proceedings of the global conference on global warming, 11-14 july, Lisbon, Portugal

Meyer SJ and Hubbard KG (1995) Extending the Crop-specific Drought Index to Soybean. In: Preprints, Ninth Conf. on Applied Climatology, Dallas, TX, Amer. Meteor. Soc., pp. 258-259

McHugh M (2006) Impact of South Pacific Circulation Variability on East African Rainfall International Journal of Climatology, 26, 505–521

Mcilveen R (1998) Fundamentals of Weather and Climate. Stanley thornes Publisher Ltd

McKee TB, Doesken NJ, Kleist J (1993) The Relationship of Drought Frequency and Duration to Time Scales, Paper Presented at 8th Conference on Applied Climatology. American Meteorological

Society, Anaheim, CA
McKee TB, Doesken NJ, Kleist J (1995) Drought Monitoring with Multiple Time Scales, Paper Presented at 9th Conference on Applied Climatology. American Meteorological Society, Dallas, Texas
Mishra AK and Singh VP (2010) A review of drought concepts. J. Hydrology 391, 2002-2016
Mitchell TD, Carter TR, Jones PD, Hulme M, New M (2005) A comprehensive set of high-resolution grids of monthly climate for Europe and the globe: the observed record (1901–2000) and 16 scenarios (2001–2100). Tyndall Centre for Climate Change Research, Norwich, Working Paper55
Morlet J, Arehs G, Fourgeau and Giard D (1982) Wave propagation and sampling theory. Geophys. 47: 203
Navarra A and Simoncini V (2010) A Guide to Empirical Orthogonal Functions for Climate Data Analysis, DOI 10.1007/978-90-481-3702-2 1
Nicholson SE (1996) A review of climate dynamics and climate variability in eastern Africa. The Limnology, Climatology and Paleoclimatology of the East African Lakes, T. C. Johnson and E. O. Odada, Eds., Gordon and Breach, 25–26
Nicholson SE (1997) An analysis of the ENSO signal in the tropical Atlantic and western Indian Oceans. Int. J. Climatol. 17: 345–375
NMSA (1996) Climatic and agroclimatic resources of Ethiopia. National Meteorological Services Agency of Ethiopia, Meteorological Research Report Series, Vol. 1, No. 1:1-137
North GR, Bell TL, Cahalan RF (1982) Sampling errors in the estimation of empirical orthogonal functions. Mon Wea Rev 110:699-706
Ntale HK and Gan TY (2003) Drought Indices and their application to East Africa. Int J climatol. 23:1335-1357
Ogallo LJ (1988) Relationships between seasonal rainfall in East Africa and the Southern Oscillation. Int. J. Climatol., 8:31-43
Ogallo LJ (1989) The spatial and temporal patterns of the East African seasonal rainfall derived from principal component analysis. Int. J. Climatol., 9:145–167
Osman M Sauerborn P (2002) A preliminary assessment of characteristics and long-term variability of rainfall in Ethiopiabasis for sustainable land use and resource management. In Paper Presented At Conference On International Agricultural Research forDevelopment, Witzenhausen, Germany, October 9-11
Pal JS, Small EE, Eltahir EAB (2000) Simulation of regional-scale water and energy budgets: representation of subgrid cloud and precipitation processes within RegCM. J Geophys Res 105:29579–29594
Pal JS, Giorgi F, Bi X, Elguindi N, Solomon F, Gao X, Francisco R, Zakey A, Winter J, Ashfaq ,M Syed F, Bell JL, Diffanbaugh NS,Kamacharya J, Konare A, Martinez D, da Rocha RP, Sloan LC,Steiner A, The ICTP RegCM3 and RegCNET (2007) regional climate modeling for the developing world. Bull Am Meteorol Soc 88:1395-1409
Palmer WC (1965) Meteorological drought. Research Paper No. 45. U.S. Weather Bureau. [NOAA Library and Information Services Division, Washington, D.C. 20852]
Palmer WC (1967) The abnormally dry weather of 1961–1966 in the Northeastern United States. In: Jerome, S. (Ed.), Proceedings of the Conference on the Drought
Palmer WC (1968) Keeping track of crop moisture conditions, nationwide: The new crop moisture index. Weatherwise, 21:156-161

Pankhurst (1968) Economic History of Ethiopia (Addis Ababa: Haile Selassie I University Press), pp. 216–222
Pankhurst (1961) An Introduction to the Economic History of Ethiopia (London: Lalibela House), pp. 236
Paul B. Henze (2000) Layers of Time (New York: Palgrave), p. 2

Plumb R (1977) The interaction of two internal waves with the mean flow: Implications for the theory of the quasi-biennial oscillation. Journal of the Atmospheric Sciences, 34, 1847-1858
Rao AR, Padmanabhan G (1984) Analysis and modeling of Palmer"s drought index series. J. Hydrol. 68: 211-229
Rencher AC (1998) Multivariate Statistical Inference and Applications, Wiley, New York
Rayner N, parker D, Horton E, Folland C, Alexander L, Rowell D, Kent E and Kaplan A (2003) Global analysis of Sea surface temperature, sea ice and night marine air temperature since the late nineteenth century. Journal of Geophysical Research, 108(d14)
Rayner NA, Brohan P, Parker DE, Folland CK, Kennedy JJ, Vanicek M, Ansell TJ, Tett SFB (2006) Improved Analyses of Changes and Uncertainties in Sea Surface Temperature Measured In Situ since the Mid-Nineteenth Century The HadSST2 Dataset. J. Climate 19 446-469. doi: http://dx.doi.org/10.1175/JCLI3637.1
Reynolds RW, Rayner NA, Smith TM, Stokes DC,Wang W (2002) An improved in situ and satellite SST analysis for climate. J Clim 15:1609-1625
Richman MB (1986) Rotation of principal components. Journal of climatology 6, 293-335
RRC (1985) The Challenge of Drought. Addis Ababa: Ethiopia: Relief and Rehabilitation Commission or Review of Drought Relief and Rehabilitation Activities
Saji NH and Yamagata T (2003) Possible impacts of Indian Ocean dipole mode events on global climate; Clim. Res. 25:151-169
Saji NH, Goswami BN, Vinayachandran PN and Yamagata T (1999) A dipole mode in the tropical Indian Ocean. Nature, 401:360-363
Schott FA, Xie SP and McCreary J (2009) Indian Ocean circulation and climate variability; Rev. Geophys. 47:RG1002 doi:10.1029/2007RG000245
Schott FA and McCreary JP (2001) The monsoon circulation of the Indian Ocean; Prog. Oceanogr. 51:1-123
Segele ZT, Lamb PJ (2005) Characterization and variability of Kiremt rainy season over Ethiopia. Meteorol Atmos Phys 89:153–180
Segele ZT, Leslie LM, Lamb PJ (2008) Evaluation and adaptation of a regional climate model for the Horn of Africa: rainfall climatology and interannual variability. Inter J Climatol. doi:10.1002/joc.1681
Segele ZT, Lamb PJ, Leslie L (2009a) Large-scale atmospheric circulation and global sea surface temperature associations with Horn of Africa June–September rainfall. Int J Climatol 29:1075-1100
Segele ZT, Lamb PJ, Leslie LM (2009b) Seasonal-to-interannual variability of Ethiopia/Horn of Africa monsoon. Part I: associations of wavelet-filtered large-scale atmospheric circulation and global sea surface temperature. J Clim 22:3396–3421
Seleshi Y and Demaree GR (1994) Sun spot numbers as a possible indicator of annual rainfall at Addiss Ababa, Ethiopia. I. J. climatology, vol. 14:911-923
Seleshi Y and Demaree G (1995) Rainfall variability in the Ethiopian and Eritrean highlands and its links with the southern Oscillation. Journal of Biogeography, 22:945-952

Seleshi Y and Zanke U (2004) Recent changes in rainfall and rainy days in Ethiopia. Int J Climatol 24:973–983

Seleshi Y and Camberlin P (2006) Recent changes in dry spell and extreme rainfall events in Ethiopia. Theoretical and Applied Climatology 83:181-191

Sen Z (2009) Spacial Modeling principles in Earth Sciences, Springer Dordrecht Heidelberg London New York, DOI 10.1007/987-1-4020-9672-3

Shafer BA, Dezman LE (1982) Development of a Surface Water Supply Index (SWSI) to Assess the Severity of Drought Conditions in Snowpack Runoff Areas. In: Preprints, Western SnowConf., Reno, NV, Colorado State University, pp. 164-175

Shankar D, Vinayachandran PN and Unnikrishnan AS (2002) The monsoon currents in the north Indian Ocean;Prog. Oceanogr. 52(1) 63–120

Shanko D and Camberlin P (1998) The Effect of the Southwest Indian Ocean Tropical Cyclones on Ethiopian Drought. International Journal of Climatology, 18:1373–1388

Slingo J Spencer H Hoskins B Berrisford P and Black E (2005) The Meteorology of the western Indian Ocean and the influence of the East African Highlands. Philosophical Transactions of the Royal Society A, 363, 25–42

Small EE, Giorgi F, Sloan LC (1999) Regional climate model simulation of precipitation in central Asia: mean and interannual variability. Journal of Geophysical Research 104: 6563-6582

Soule PT (1993) Spatial patterns of drought frequency and duration in the contiguous USA based on multiple drought event definitions. Int. J. Climatol. 12:11-24

Sun L, Semazzi FHM, Giorgi F, Ogallo LA (1999a) Application of the NCAR regional climate model to eastern Africa. Part I: simulation of the short rains of 1988. J Geophys Res 104:6529-6548

Sun L, Semazzi FHM, Giorgi F, Ogallo LA (1999b) Application of the NCAR regional climate model to eastern Africa. Part II:simulation of interannual variability of short rains. J Geophys Res 104:6549-6562

Tadesse T (1994) The influence of the Arabian Sea storms/depressions over the Ethiopian weather. Proc Int. Conf. on monsoon variability and prediction, WCRP-84 and WMO/TD No. 619,World Meteorological Organization, Geneva, pp 228-236

Takahashi M and Holton JR (1991) The mean zonal flow response to Rossby wave and gravity wave forcing in the equatorial lower stratosphere: Relationship to the QBO Journal of the Atmospheric Sciences 48 2078-2087

Thom HCS (1966) Some methods of climatological analysis. W.M.O., 415, Nota tecnica 81, Geneve

Thornthwaite CW (1948) An approach towards a rational classification of climate. Geographical Review 38: 55–94

Tilahun K (1999) Test of homogeneity, frequency analysis of rainfall data and estimate of drought probabilities in Dire Dawa, eastern Ethiopia. Ethiopian Journal of Natural Resources 1: 125–136

Torrence C, Compo GP (1998) A practical guide to wavelet analysis. Bull Am Meteorol Soc 79:61-78

Torrence C, Webster PJ (1999) Interdecadal changes in the ENSO-monsoon system. J. Climate 12, 2679-2690

Tozuka T and Yamagata T (2003) Annual ENSO J Physical Oceanography Volume 33 pp 1564-1578

UN-Habitat (2007) Situation Analysis of Informal Settlements in Addis Ababa, UN-Habitat. United Nations, Human Settlements Programme

Vizy EK and Cook KH (2001) Mechanisms by which the Gulf of Guinea and eastern North Atlantic sea surface temperature anomalies can influence African rainfall. J. Climate 14, 795–821

Von Storch H and Zwiers FW (1999) Statistical Analysis in Climate Research. Cambridge University Press, 484 pp, ISBN 0521 450713

Wang C (2002a) Atlantic climate variability and its associated atmospheric circulation cells. J. Climate 15, 1516-1536

Wang C (2002b) Atmospheric circulation cells associated with the El Niño-Southern Oscillation. J. Climate, 15, 399-419

Wang C (2005) ENSO, Atlantic climate variability, and the Walker and Hadley circulations. In The Hadley Circulation: Present Past and Future, edited by H.F. DIAZ, and R.S. BRADLEY. Kluwer Academic Publishers, 173–202

Wang C (2006) An overlooked feature of tropical climate: Inter-Pacific-Atlantic variability. Geophys. Res. Lett. 33 L12702, DOI: 10.1029/2006GL026324

Wang Y Leung LR McGregor JL Lee DK Wang WC Ding Y Kimura F (2004) Regional climate modeling: progress, challenges and prospects. J Meteorol Soc Jpn 82:1599-1628

Webster PJ Moore AM Loschnigg JP and Leben RR (1999) Coupled ocean-atmosphere dynamics in the Indian Ocean during 1997-98. Nature, 401:356–360

Weghorst KM (1996) The Reclamation Drought Index: Guidelines and Practical Applications. Bureau of Reclamation, Denver, CO, p. 6 (Available from Bureau of Reclamation, D-8530, Box 25007, Lakewood, CO 80226)

Wells N (2002) Development of the self-calibrating Palmer drought severity index. Undergraduate Thesis, University of Nebraska–Lincoln

Wilhite DA (2000) Drought: A Global Assessment, Vols. 1 and 2. Routledge, New York, 89-104, 1 and 2, Routledge, New York, pp. 129-448

Wilhite DA (2000b) Drought as a natural hazard: concepts and definitions. In:Wilhite, D.A. (Ed.), Drought: A Global Assessment, vol. 1. Routledge, New York, pp. 1-18

Wilhite DA and Glantz MH (1985) Understanding the drought phenomenon: The role of definitions. WaterInt., 10, 111–120

Wilhite DA and Glantz MH (1987) Understanding the drought phenomenon: the role of definitions. In Planning for Drought: Towards a Reduction of Society Vulnerability, Wilhite DA, Easterling EA, Wood DA (eds). Westview Press: Colorado; 11–27

Willeke G Hosking JRM Wallis J Guttman NB (1994) The National Drought Atlas. Institute for Water Resources Report 94-NDS-4, US Army Corps of Engineers

Wood A (1977) A preliminary chronology of Ethiopian droughts. In Drought in Africa, Vol. 2, Dalby D, Church RJH, Bezzaz F (eds). International African Institute: London; 68–73

World Meteorological Organization, 1975a: Drought and agriculture. WMO Note 138, Publ. WMO-392, Geneva, Switzerland, 127 pp

Yeshanew A and Jury M (2007) North African Climate Variability. Part 2:Tropical circulation systems. Theoretical and Applied Climatology, 89:37–49

Zeleke T Giorgi F Mengistu Tidu G and Diro GT (2012) Spatial and temporal variability of summer rainfall over Ethiopia from observations and a regional climate model experiments. Theor Appl Climatol. DOI 10.1007/s00704-012-0700-4

Zhou G Minakawa N Githeko A and Yan G (2004) Association between climate variability and malaria epidemics in the East African highlands. Proceeding of the National Academy of Sciences of the USA, 101(8), 2375–2380

Declaration

This thesis is my original work, has not been presented for a degree in any other University and that all the sources of material used for the thesis have been dully acknowledged.

Name: Tadesse Terefe

Signature: ----------

This thesis has been submitted for examination with my approval as University advisor.

Name: Dr. Gizaw Mengistu

Signature: ----------

Place and time of submission:
Department of Physics
Addis Ababa University
June 2013